12-2012

Phase Transformation in Ti-Mo-O

Herbert Boeckels
Clemson University, herbb@clemson.edu

PHASE TRANSFORMATIONS IN TI-MO-O

A Dissertation
Presented to
the Graduate School of
Clemson University

In Partial Fulfillment
of the Requirements for the Degree
Doctor of Philosophy
Material Science and Engineering

---

by
Herbert Boeckels
December 2012

Submitted to:
Dr. Henry J. Rack, Committee Chair
Dr. JoAn Hudson
Dr. Jian Luo
Dr. William T. Pennington

ABSTRACT

The present dissertation has investigated the effect of oxygen on the ω and α phase stability in metastable Ti-Mo β titanium alloys using thermal analysis, hardness measurements, electron microscopy, and x-ray diffraction.

Single crystal x-ray diffraction has shown that oxygen atoms are located in the tetrahedral interstitial lattice sites in the rapidly cooled bcc Ti crystal structure, interfering directly with the reversible displacive formation of ω, with this transformation involving collapse of the bcc lattice along $<111>_{\beta}$. Subsequent thermal exposure of reversible ω, as occurring during slower cooling, heating, and aging, prompts short range diffusion and the formation of chemical altered irreversible ω.

X-ray diffraction particle size analysis based on the Warren-Averbach approach has shown that the continued irreversible ω phase evolves in four stages during isothermal aging, initial growth followed by size stabilization, coarsening, and dissolution. The latter stages of ω evolution are controlled by elastic residual stresses surrounding these particles. Ultimate stress relaxation is based on secondary formation and growth, promoting coarsening and dissolution of ω. All of the aforementioned stages can be accelerated by increasing both the oxygen content and isothermal aging temperature.

The hardness response parallels this evolution and is dependent upon the ω and α phase evolution. The initial hardness increase is due to the growth of ω. The hardness plateau is based on stabilized ω size and fine α precipitation. The overaging hardness response is due to continuous secondary α formation and growth combined with ω

coarsening and dissolution. Hardness increases with increasing interstitial content as a result of solid solution strengthening and α particle refinement.

Isochronal and isothermal thermal analysis has shown that increasing oxygen content promotes the α phase formation thereby increasing the ω instability. Grain boundary and primary α morphology growth are associated with the growth and thickening of sideway α platelets at low aging temperatures and longer aging times. The highest oxygen levels investigated, 2 weight percent (wt%), promotes earlier intragranular α nucleation.

DEDICATION

To my family.

"You miss 100% of the shots you don't take." – Wayne Gretzky

ACKNOWLEDGMENTS

I wish to express my sincere sense of gratitude to my advisor and friend, Prof. Henry J. Rack, for his support and valuable guidance not only through this investigation but also in my personal life.

I also wish to thank the other members of my advisory committee, Prof. JoAn Hudson, Prof. Jian Luo and Prof. William T. Pennington for their cooperation and help.

Thanks are also due to Dr. C. McMillen and Dr. D. VanDerveer for helping me with the single crystal work as well as Mr. Dino Sulejmanovic in the Clemson Chemistry Department. I also would like to thank Dr. R.E.A. Williams and Prof. H.L. Fraser for training and helping me use the Ohio State University Microscope facilities. Further Thanks are due to Dr. V. Guether from GfE, Erlangen, Germany, for producing selected Ti-Mo-O buttons.

Finally, I would like to thank all my friends, who visited me from the old world making my summers awesome and all my new friends I made in the new world and making my daily life in Clemson great: Evans, Andy (2x), Katrin, Chris, Cris, Frank, Stephan, Taylor, Steve, Ben, Pepe, Jean, David, Brock, Porter, Peters, Angela, James, Lee, Adam, Bryci, Chip, Bonnie, Duffy, Katie, Julie, Marice, Chuck, Rod, Brett, Liam, Ringo, Cody, Ryan, Clark, Aaron, Heather, Randy and many more (sorry limited space here), who I met on my PhD journey.

TABLE OF CONTENTS

Page

Table of Content (Continued)

Page

Table of Content (Continued)

Page

LIST OF FIGURES

Figure Page

List of Figures (Continued)

Figure Page

List of Figures (Continued)

Figure Page

List of Figures (Continued)

Figure Page

List of Figures (Continued)

Figure Page

List of Figures (Continued)

Figure Page

List of Figures (Continued)

Figure Page

List of Figures (Continued)

Figure Page

List of Figures (Continued)

Figure Page

List of Figures (Continued)

Figure Page

LIST OF TABLES

Table Page

List of Tables (Continued)

Table Page

CHAPTER ONE

1. INTRODUCTION

Metastable β titanium alloys having high strength to density ratio, low modulus of elasticity, good cold formability, and deep hardenability as well as high corrosion resistance, are of increasing interest to the biomedical [1,2], automotive [3], aerospace [4], and energy industries [5]. Indeed, this alloy class offers perhaps the widest range of microstructure and mechanical properties among titanium alloys. Their properties are primarily determined by the proportions, distributions, and morphologies of the α precipitates, for strengthening, and their β grain size, for ductility.

One particular area of interest is the influence of the metastable ω phase on the microstructural evolution occurring during non-equilibrium heat treatment, with ω precipitates having been shown to act as potent α nucleation sites [6-12] during artificial aging. Three different nucleation sites of the α precipitates have been proposed in the literature, one at the ω/β interface [13], one within the ω phase [10, 14], and one at a certain distance from the ω precipitates [15]. This variety of nucleation sites is expected to be impacted by the interstitial content, as well as cooling and heating rates during heat treatments. Indeed, it is well documented [8, 9 and 16-21] that oxygen suppresses the ω formation and, at the same time, it can also act as an interstitial strengthener in the solutionized condition while increasing the aging kinetics of the α phase. Furthermore, when certain alloy dependent oxygen levels are reached, the oxygen atoms may cluster [18] and may themselves act as α nucleation sites. Increased attention has recently

focused on understanding the heating rate dependency on the aging reactions. Flowers et al. [12] showed that the heating rate during aging effected the phase transformations and hardness response of Ti-15Mo comparing salt bath and air furnace treatments. In addition Vassel [22] quantified the heating rate effect: at a faster heating rate, 200˚Cmin^{-1}, abetted homogeneous α precipitate within the matrix, while at a slower heating rate, 1 ˚Cmin^{-1}, ω-assisted α nucleation was observed in Ti-10V-2Fe-3Al. A further decrease in heating rate has shown that phase separation becomes a leading role for α precipitation. The β phase decomposes into two separated β phases possessing similar crystal structures (bcc) but different lattice parameters [23, 24].

This present investigation has examined the role of oxygen on ω and α phase formation in the metastable β titanium alloy Ti-15Mo. Addition efforts have compared various heating rates to clarify their impact on the ω phase stability during artificial aging.

1.1. References

[1] M. Long, R. Crooks, and H.J. Rack, “High-Cycle Fatigue Performance of Solution-Treated Metastable-β Titanium Alloys”, Acta Materialia, Vol. 47 (2), (1999), 661-669

[2] V.R. Jablokov, M.J. Nutt, M.E. Richelsoph and H.L. Freese, “The Application of Ti-15Mo B Titanium Alloy in High Strength Orthopaedic Applications”, Journal of ASTM International No.8, (2005)

[3] O. Schauerte, “Titanium in Automotive Production”, in Titanium and Titanium Alloys, ed. Leyens, C. and Peters, M., Wiley-VCH, Berlin, 2003: 467-482

[4] R.R Boyer, “An Overview on the Use of Titanium in the Aerospace Industry”, Material Science & Engineering, A213, (1996): 103-114

[5] B. Craig, “MATERIALS FOR DEEP OIL AND GAS CONSTRUCTION”, Advanced Materials and Process, May, 2008, pp. 33-36

[6] T.W. Duering and J.C. Williams, “Overview: Microstructure and Properties of B Titanium Alloys”, in B Titanium Alloys of the 1980´s, ed. Boyer R.R. and Rosenberg, H.W., The Minerals, Metals & Materials Society, Warrendale, PA, (1983):pp. 19-67

[7] G. Lütjering and J.C. Williams, “Titanium”, Springer 2003: pp. 13-48

[8] J.C. Williams, B.S. Hickman and H.L. Marcuse, “The Effect of Ω Phase on the Mechanical Properties of Titanium Alloys”, Metallurgical Transactions, Vol. 2, (1971): pp. 1913-1919

[9] A.W. Bowen, “Ω Phase Formation in Metastable β-Titanium Alloys”, in B Titanium Alloys of the 1980´s, ed. Boyer, R.R. and Rosenberg, H.W., The Minerals, Metals & Materials Society, Warrendale, PA, (1983):pp. 85-106

[10] D. De Fontaine, N. Paton and J.C. Williams, “The ω phase transformation in titanium alloys as an example of displacement controlled reactions”, Acta Metallurgica, Vol. 19, (1971): pp. 1153-1162

[11] F. Prima, P. Vermaut, G. Texier, D. Ansel and T. Gloriant, “Evidence of α-nanophase heterogeneous nucleation from ω particles in a metastable β Ti-based alloy by high-resolution electron microscopy“ Scripta Materialia, Vol. 54, (2006), pp. 645-648

[12] G.M. Pennock, H.M. Flower and D.R.F. West, "THE CONTROL OF α PRECIPITATION BY TWO STEP AGING IN β TI-15%Mo", Titanium'80, Science and Technology (1980); pp. 1343–1351.

[13] S. Nag, R. Banerjee, R. Srinivasan, J.Y. Hwang, M. Harper and H.L. Fraser, "ω-Assisted nucleation and growth of α precipitates in the Ti-5Al-5Mo-5V-3Cr-0.5Fe β-titanium alloy", Acta Metallurgica, Vol. 57, (2009), pp. 2136-2147

[14] F. Langmayr, P. Fratzl and G. Vogel, "Crossover from ω-phase to α-phase precipitation in Ti-Mo", Phys. Rev. B, Vol. 49, No 17, (1994), pp. 11759-11766

[15] D. De Fontaine, "Simple models for the ω phase transformations", Met. Trans., Vol. 19A, (1988): pp. 169-175

[16] R.G. Henning, D.A. Trinkle, J.A. Bouchet, J.G. Srinivasan, R.C. Albers and J.W. Wilkins, "Impurities block the α to ω martensitic transformation in titanium", Nature Materials, Vol. 4, (2005), pp. 129-133

[17] J.I. Qazi, V. Tsakiris, B. Marquardt and H.J. Rack, "The effect of duplex aging on the tensile behavior of Ti-35Nb-7Zr-5Ta-(0.06-0.7)O alloys", Ti-2003: Science and Technology, Luertjering, G. and Albrecht, J., eds., Wiley-VCH Verlag Gmbh, Weinheim, Germany, pp.1651-1658

[18] J.I. Qazi, B. Marquardt, L. Allard and H.J. Rack, "Phase transformations in Ti-35Nb-7Zr-5Ta(0.06-0.7)O alloys", Material Science & Engineering, Vol. C25,(2005), pp. 389-397

[19] J.I. Qazi, V. Tsakris, B. Marquardt and H.J. Rack, "Effect of aging treatments on the tensile properties of Ti-35Nb-7Zr-5Ta(0.06-0.7)O alloys", Jn. ASTM(JAI),Vol. 2, No.8, (2005)

[20] J.I. Qazi and H.J. Rack, "Metastable B Titanium Alloys for biomedical Applications", Advanced Engineering Materials, Vol. 7, No. 11,(2005), pp. 993-998

[21] J.I. Qazi and H.J. Rack, "Titanium alloys for biomedical Applications", Material Science & Engineering. C, Vol. 26, (2006), pp. 1269-1277

[22] A. Vassel, "Microstructural Instabilities in B Titanium Alloys", in B Titanium Alloys of the 1990´s, ed. Eylon, D., Boyer, R. R., and Koss, D.A., The Minerals, Metals & Materials Society, Warrendale, PA, (1993):pp. 173-185

[23] O.M. Ivasishin, P.E. Markovsky, S.L. Semiatin and C.H. Ward, “Aging Response of coarse- and fine grained β titanium alloys”, Material Science & Engineering A, Vol. 405, (2005), pp. 296-305

[24] T. Gloriant, G. Texier, F. Sun, I. Thibon, F. Prima and J.L. Soubeyroux, “Characterization of nanophase precipitation in a metastable β titanium-based alloy by electrical resistivity, dilatometry and neutron diffraction”, Scripta Materialia, Vol. 58, (2008), pp. 271-274

CHAPTER TWO

2. LITERATURE REVIEW

2.1. Titanium and Titanium Alloy Classes

Pure titanium (Ti) below 882°C exhibits a hexagonal closed packed (hcp) crystal structure and is referred to as the α phase (α), having lattice parameters of a=2.9512 Å and c=4.6845Å for pure titanium. Two types of α phases have been reported: one, known as type I α, which obeys the Burgers orientation with respect to the β phase, i.e., $\{0001\}_{\alpha}$ // $\{110\}_{\beta}$ and $<11\text{-}20>_{\alpha}$ // $<111>_{\beta}$ and the other, known as type II α, which does not obey the Burgers orientation relation but is in a {10-12} <10-11> twin orientation with respect to type I α. The Burgers relations allow 12 different variants of type I α. Above 882°C the body centered cubic (bcc) β phase (β) is stable. The β phase exhibits a body-centered cubic (bcc) crystal structure, with a lattice of 3.3066 Ångstrom for pure titanium. In alloys the lattice parameter of β is composition dependent, decreasing with increasing β-stabilizing content [1-4]. Thermodynamically, the β is phase stable above the β-transus and metastable below it. Fully β phase titanium alloys exhibit good formability due to their bcc crystal structure, having a strength level typically above 850 MPa [5].

The α to β transformation temperature, the so called "β-transus" (β_T), may be modified through the addition of various alloying elements. These can be differentiated as α-stabilizing, which increase the β-transus temperature, e.g. Al, N, O, and β-stabilizing, which decrease the β-transus temperature, e.g. Mo, V, Nb, Fe. B stabilizers

may be further subdivided into β-isomorphous elements, which are fully soluble in the β phase, and β-eutectoid elements, which form intermetallic compounds with titanium.

Moreover, titanium alloys can be classified as α, α + β and metastable β alloys depending on which phase is predominant in the microstructure at room temperature, Figure 2-1. A (α) alloys normally contain Al, O and Sn with minor additions of β stabilizers, the latter additions being limited to maintain a complete α solid solution. α + β alloys contain additional β stabilizer additions, these alloys having a β volume fraction of 5-40 percent. In β solution treated and quenched α + β alloys, having a lean β stabilizer content, the hcp martensite (α') can form. Increasing the β stabilizer content further causes the orthorhombic martensite (α") to form instead [8-10]. Finally, the metastable β alloy class is reached, when the proportion of β-stabilizing elements is increased to a level that suppresses the martensitic transformation of the β phase, M_S, below room temperature, Figure 2-1 [5-8].

Variation in the martensite start temperature (M_S) is related to variation in the association of different β stabilizing atoms with titanium. In a 1:1 titanium solid solution with varying β stabilizers, vanadium atoms exhibit a random placement in the lattice. In this case, twelve atomic percent vanadium has been found to completely suppress the M_S below room temperature [9]. In the same 1:1 solid solution, molybdenum atoms order within the crystal lattice, forming a B2 structure. This ordering correlates to the lower atomic percent necessary (eight atomic percent) needed to suppress the martensite start temperature in a titanium molybdenum structure

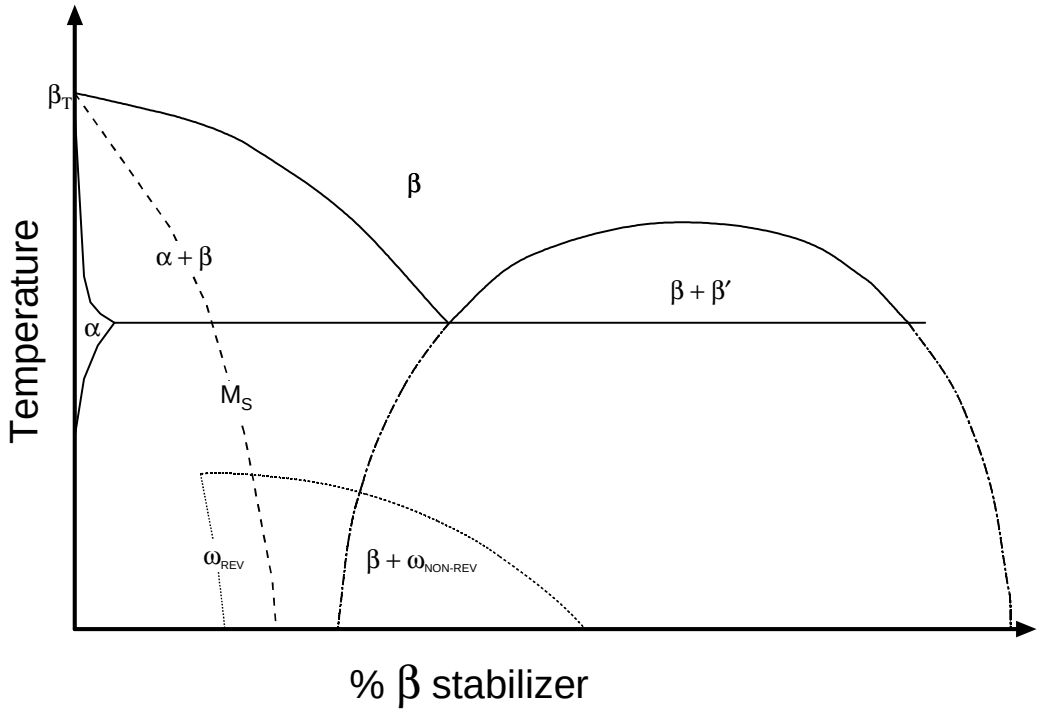

Figure 2-1: Schematic pseudo binary phase diagram of titanium and a β-stabilizer, where β_T is the β-transus temperature and βs are the critical minimum levels of β-stabilizing content for metastable and stable β titanium alloys monotectoid reaction [12].

[10, 11]. By contrast, niobium atoms in a similar ratio form niobium clusters, with seventeen atomic percent being required to lower the M_S below room temperature [10].

Finally, at the higher solute contents, a competition between the metastable ω and martensite phases is often observed [13, 14].

A common means of quantifying the degree of stability of titanium alloys based on β_T temperature is to evaluate its "molybdenum equivalent" [15] and "aluminum equivalent" [16] as given by:

$$Mo - Eq. = 1.0(wt\%Mo) + 0.67(wt\%V) + 0.44(wt\%W) + 0.28(wt\%Nb) + 0.22(wt\%Ta) + 2.9(\text{wt\%Fe}) + 1.6(\text{wt\%Cr}) - 1.0(\text{wt\%Al})$$

and

$$Al - Eq. = 1.0(wt\%Al) + 10.00(wt\%O) + 10.00(wt\%C) + 0.17(wt\%Zr) + 0.33(wt\%Sn)$$

with metastable β titanium alloys having a MoEq. greater than 10 [15], Table 2-1.

2.2. Metastable β-Titanium Alloys

Metastable β titanium alloys exhibit greater hardenability, corrosion resistance, workability, and strength to density ratios than do α + β alloys [5-8]. Two established processing routes are normally used during the production of metastable β titanium

Table 2-1: Commercial metastable β titanium alloys classified in order of increasing MoEq[5].

Nominal Composition (wt%)	Common Designatin	MoEq.	AlEq.
Ti-11.5Mo-6Zr-4.5Sn	β-III	11.5	2.5
Ti-15V-3Cr-3Sn-3Al	Ti-15-3	11.9	4.0
Ti-15Mo-2.7Nb-3Al-0.2Si	β-21S	12.8	3.0
Ti-3Al-8V-6Cr-4Zr-4Mo	Ti-38644, β-C	16.0	3.7
Ti-8V-8Mo-2Fe-3Al	Ti-8823	16.1	3.0
Ti-15Mo-0.2O	Ti-15Mo	15.0	2.0
Ti-6.8Mo-4.5Fe-1.5Al	TIMET LCB	18.4	1.5
Ti-13V-11Cr-3Al	-	23.3	3.0

alloys. One involves β deformation processing and solution treatment, either within the single phase β field or high in the α + β phase field. The other involves through-transus processing where final deformation processing is performed at continuously decreasing temperatures, typically starting just above the β-transus and continuing into the α + β phase field. Final solution treatment after processing, if desired, may also be performed for short times within the β phase field or within the α + β phase field. The latter processing route involves extensive subtransus deformation and tends to result in smaller primary α particles [5]. Similarly it offers the opportunity for controlling the size and continuity of grain boundary α [1, 17]. The important difference between these routes is their effect on the β phase stability after processing. α + β processing and/ or solution treatment, results in continued α phase precipitation and as a consequence, the β phase becomes enriched in β-stabilizers and depleted in α-stabilizers. Performing an α + β solution treatment/processing is thus a convenient way of increasing the β phase stability, whereas β solution treatment followed by quenching results in the minimum β phase stability.

Based on the solute content, metastable β titanium alloys, as first proposed by Duering and Williams [6], can be subdivided into solute lean and solute rich alloys. The difference between these is that the former types decompose on quenching into either α' or α" depending on interstitial content and/or strain level [13, 14, 18, 19][1] and/or ω

[1] Strain induced Martensite can be found in extreme lean β alloys due to residual stresses

phase, historically called athermal ω (ω_a). In contrast, solute rich alloys exhibit a phase separation into a solute rich β-phase and a solute lean β'-phase on quenching.

Advances in characterization techniques, e.g. aberration corrected high resolution transmission electron microscopy (HRTEM) and 3D atom probe tomography (3DATP), have shown that the ω phase forms through an initiated collapse of the $\{111\}_\beta$ planes within solute depleted pockets resulting in the formation of ω-like embryos in solute rich metastable β alloys, Figure 2-2 [20-23]. It has also been shown that during aging the displacive and diffusional components are closely coupled due to continuous changing in composition and further collapsing along the $<111>_\beta$ allowing the ω particles to grow initially displacively and deplete in solute content during further aging diffusionally. A free energy diagram was proposed for a Ti-18wt% Mo alloy, Figure 2-3a, corresponding to the phase diagram proposed by Furuhara [24], Figure 2-3b, the authors later proposing that a miscibility gap in the β phase based on a pseudo-spinodal decomposition of the β phase exists. This leads to solute lean pockets in which the ω-like embryos can form.

The aging behavior of metastable β titanium alloys may be further characterized by two distinct temperature regimes: a high temperature regime, in which β transforms directly into the α phase; and a low temperature regime, in which the β phase first transforms into a "transition" phase which later transforms into equilibrium α phase. The boundary between both regimes typically lies between 400 and 500˚C, depending on the alloy system and details of the thermal processing, the latter being a focal point

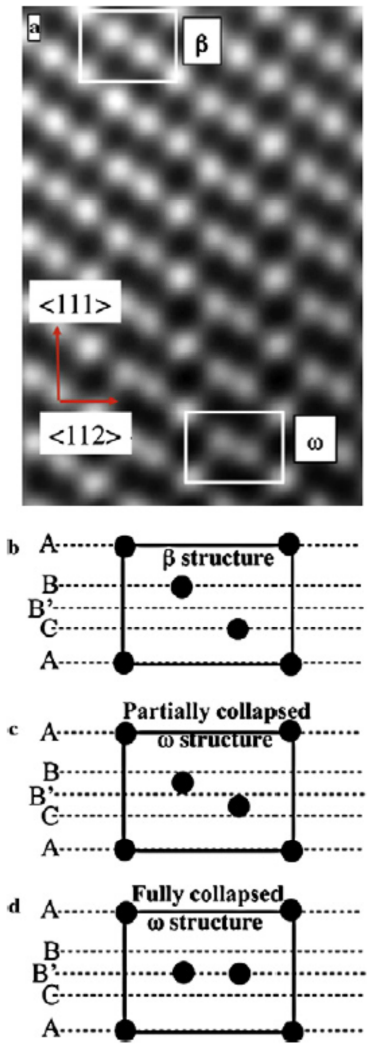

Figure 2-2: (a) Enlarged HAADF-HRTEM image showing the transition from collapsed β structure on top to the collapsed ω-like structure in the bottom side of the image. The motif of β and ω are highlighted with white rectangles. (b-d) The schematic figures for the ideal motifs of β, partially collapsed ω and fully collapsed ω structures. The ABCABC stacking of 222 planes in the β and AB'AB' stacking in the collapsed ω structures are highlighted [23].

of this dissertation [25, 26]. This behavior can be schematically represented on a time-temperature-transformation (TTT) diagram, Figure 2-4. The transition phase involved in the low temperature aging precipitation sequence can either involve β' or the metastable ω phase, depending on the alloy composition and temperature. The ω phase forms directly in weakly β-stabilized systems which are designated solute-lean β alloys, while β' occurs in more heavily alloyed systems known as solute-rich β alloys [6].

Finally, cooling rates, from the solution treatment temperature, also have an impact on the β matrix stability. For example, rates greater than $8Ks^{-1}$ for a solute lean

and 1 Ks-1 for a solute rich alloy are needed to suppress heterogeneous α nucleation and growth during cooling [27, 28].

1.1. ω Phase

The ω phase is metastable with respect to the equilibrium α and β phase, forming either as very small particles upon quenching or as larger particles, both of which coarsen upon low temperature aging [5-8, 29-34]. The ω phase transformation was first observed by Frost et al. in quenched Ti alloys in 1954 [35], its structure being later clarified by Silcock [36], Blackburn and Williams [37] as hexagonal obeying the following relationship: $<11\text{-}20>_\omega$ // $<110>_\beta$ and $(0001)_\omega$ // $(111)_\beta$. As a consequence, there are four possible variants of ω particles, parallel to the four $<111>_\beta$ directions, equally populated in undeformed alloys [26]. It is further well established [26, 38, 39]

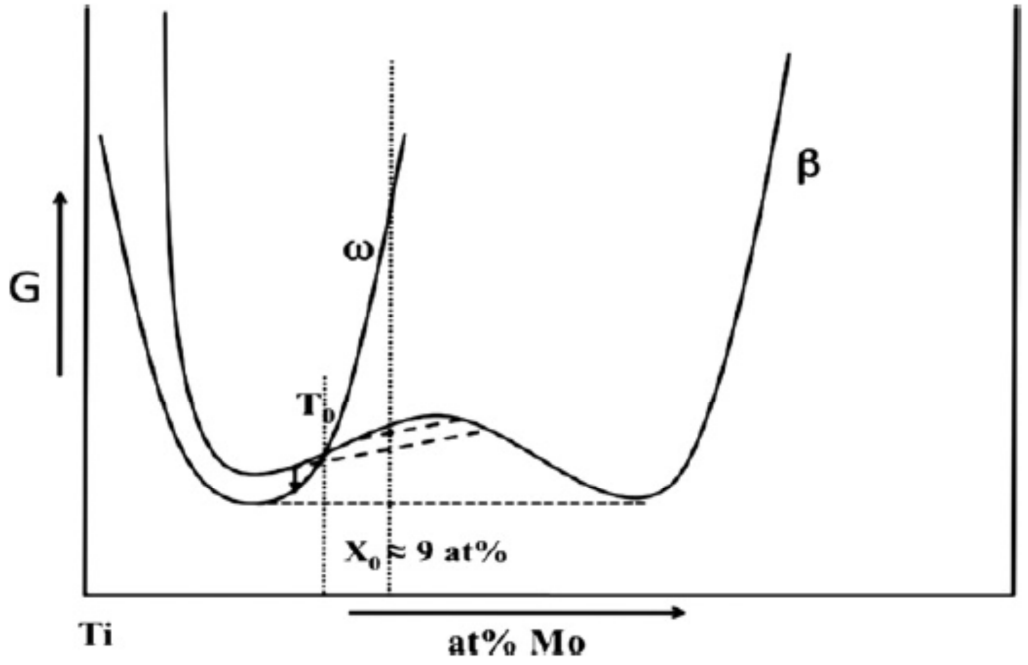

(a)

Figure 2-3: (a) Schematic free energy vs. composition plots for the β and ω phases in Ti-9at% Mo alloy under lower temperature under lower temperatures that illustrates the transformation mechanism. A miscibility gap is shown in β free energy curve and the average alloy composition is marked by th vertical dotted line. The T_0 point where the β and ω free energy curves intersect is also marked in the figure. The sequential phase separation in β and subsequent structural transformation of Mo-depleted β regions to ω are shown in the figure using dashed lines and arrow [20]. (b) A Ti-Mo schematic phase diagram, publiished by Furuhara et al. [38], which exhibits that the Ti-18wt.%Mo alloy lies within the calculated coherent spinodal regime.

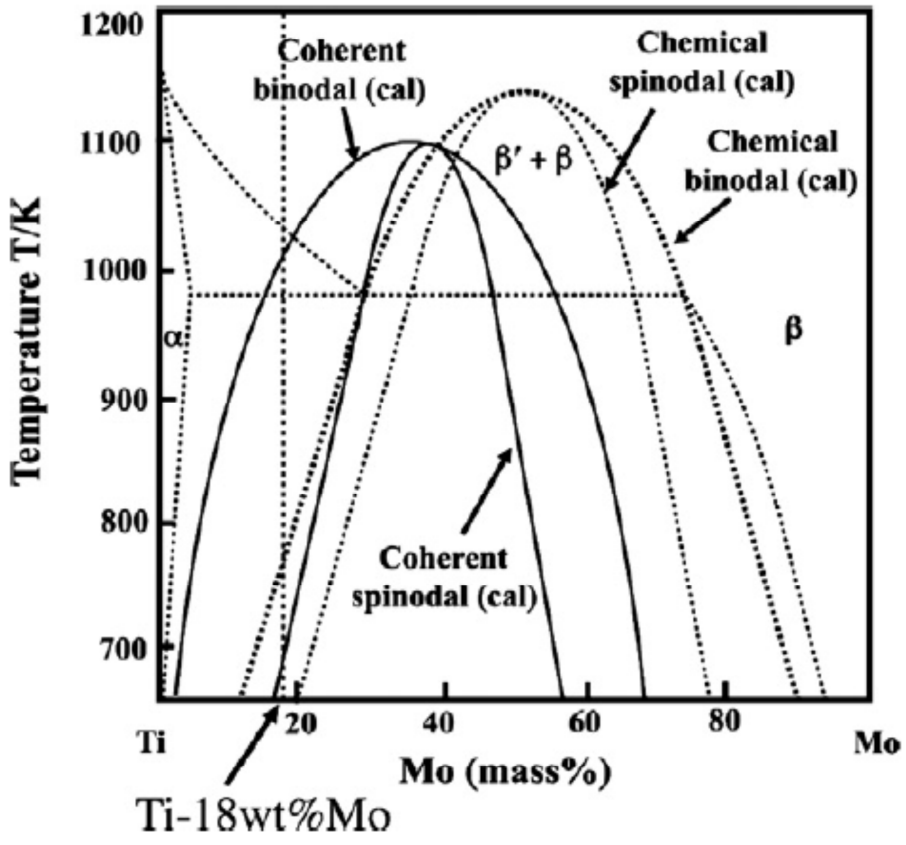

(b)

Figure 2-3: continued

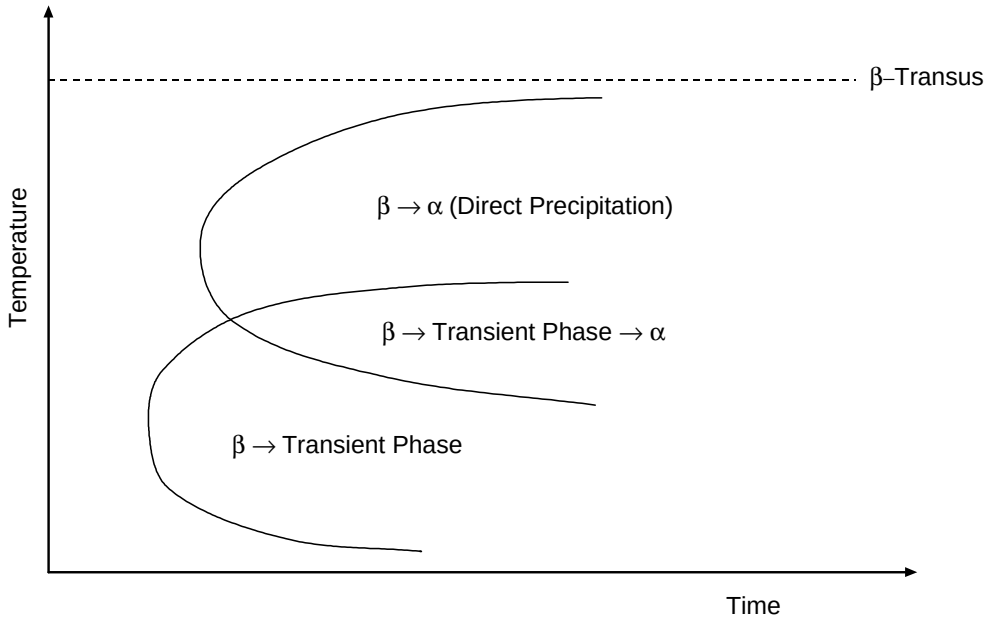

Figure 2-4: Typical TTT diagram for metastable β titanium alloys.

that the ω phase forms in solute lean alloys based on a displacive, diffusion-less transformation on quenching and occurs as a highly uniform distribution of very fine particles, arranged in rows along the $<111>_\beta$ directions [32, 34]. Figure 2-5 illustrates the collapse of a pair of $(111)_\beta$ planes due to a 2/3 $<111>_\beta$ longitudinal displacement wave. A complete collapse in weak alloyed systems leads to an ideal hexagonal ω structure as shown in Figure 6. An incomplete trigonal ω "rumpled" structure is produced by further increasing the alloying content and causing only partial collapse of the $<111>_\beta$ planes. This can be seen in Figure 2-6.

Incorporation of small amounts of interstitial atoms can produce a large suppression in ω start temperature. Results from Williams and Paton in a Ti-(17-20)V-(0.02-0.19)O system (wt%) are shown in Figure 2-7 [40]. The ω start temperature (ω_S) is plotted versus the amount of interstitial oxygen depending on the vanadium content. At the highest investigated vanadium content, 20 weight percent, a small amount (0.01 wt%) of oxygen is addition of more oxygen is necessary to obtain the same result. At the lowest vanadium concentration used in Paton's study (17 weight percent), 0.03 weight percent of the interstitial oxygen is necessary.

These results from the early 70s were not further investigated until Rack et al. in the late 90s used oxygen as an alloying element during their development of the Ti-35Nb-7Zr-5Ta alloy system [41-43]. They also observed the reduction of ω_S with interstitial oxygen inclusion. A correlated observation in further studies by Rack's

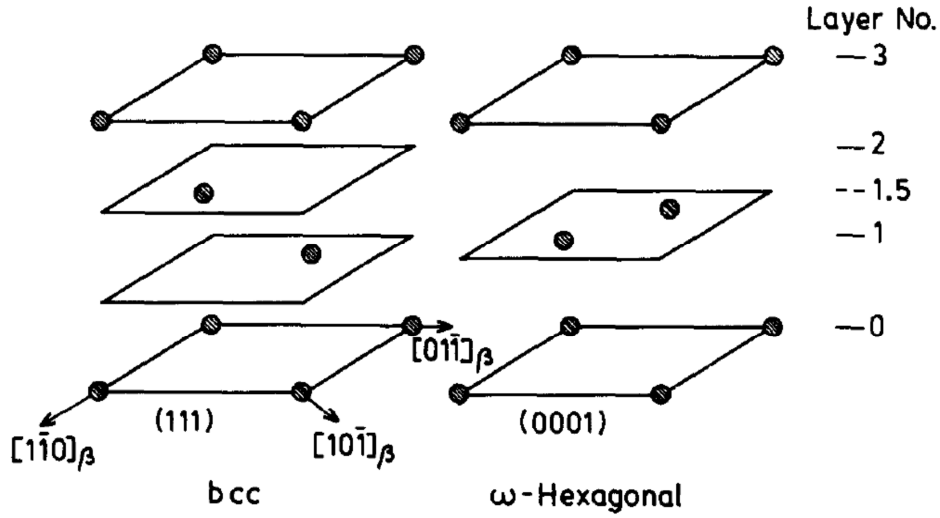

Figure 2-5: <111> plane collapse model: (111) planes in β phase become (0001) in ω phase with central atoms moving from layer 1 and 2 to layer 1.5 [38].

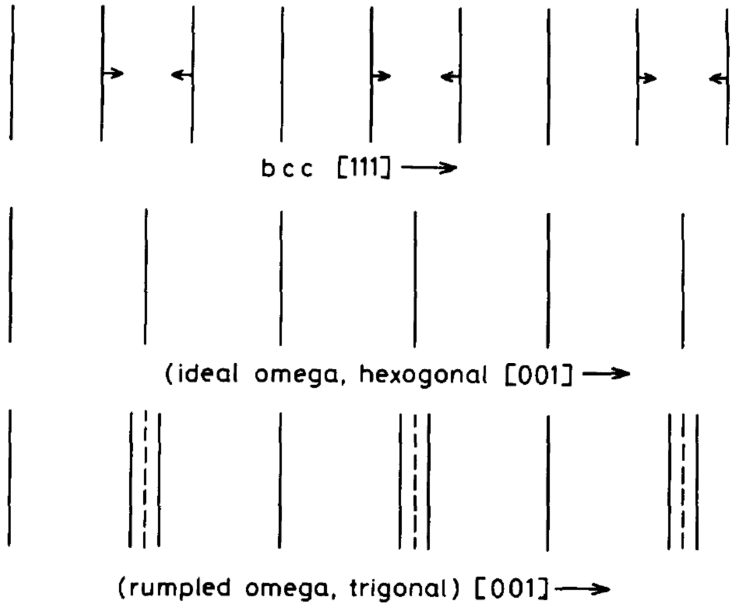

Figure 2-6: Schematic illustration of ideal and rumpled ω phase [38].

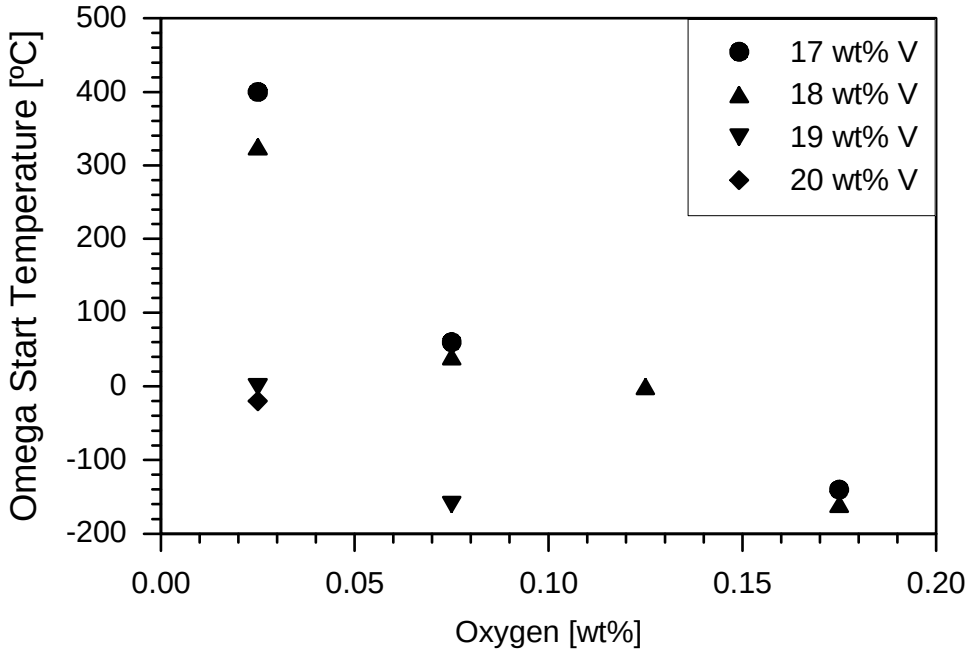

Figure 2-7: Influence of Oxygen Content on the Athermal β-ω Transformation [40].

group demonstrated a relationship between oxygen content and Young's modulus. This relationship, a minimum in modulus being observed with increasing oxygen content was reported within detailed explanation [44]. The same observations were made by Kim and Kim in a simpler Ti-Nb-O system. Their results are shown in Figure 2-8 [45], where the correlation between Young's modulus and niobium, and Young's modulus and associated niobium oxygen content is shown. There is still no explanation available for this phenomenon. This leads to another focal point of this dissertation. No work was found on the Ti-Mo-O system.

Finally, De Fontaine [39], was among the first to recognize that there is no physical basis for differing between "athermal" and "isothermal" ω (ω_a, ω_{iso}). Later Duering et al. [46] suggested that the formation of the ω_{iso} phase during aging below 450˚C cannot be explained by a classical diffusion controlled nucleation and growth process. Their experimental evidence showed that: an unusual rapid ω growth rate of "isothermal" ω in Ti-10V-2Fe-3Al at low temperatures. When diffusion is permitted, the isothermally formed ω particles were very uniform in size at any given temperature, at higher temperatures larger particles and a fewer number was observed, the aging times not having a significant effect on the ω_{iso} particle size. In tutu, the initial morphology of the ω particles was ellipsoidal and changed into cuboidal upon longer aging times. In order to explain their results, an alternative model based on the displacive continuation of "isothermal" ω particles was proposed. Based on their model,

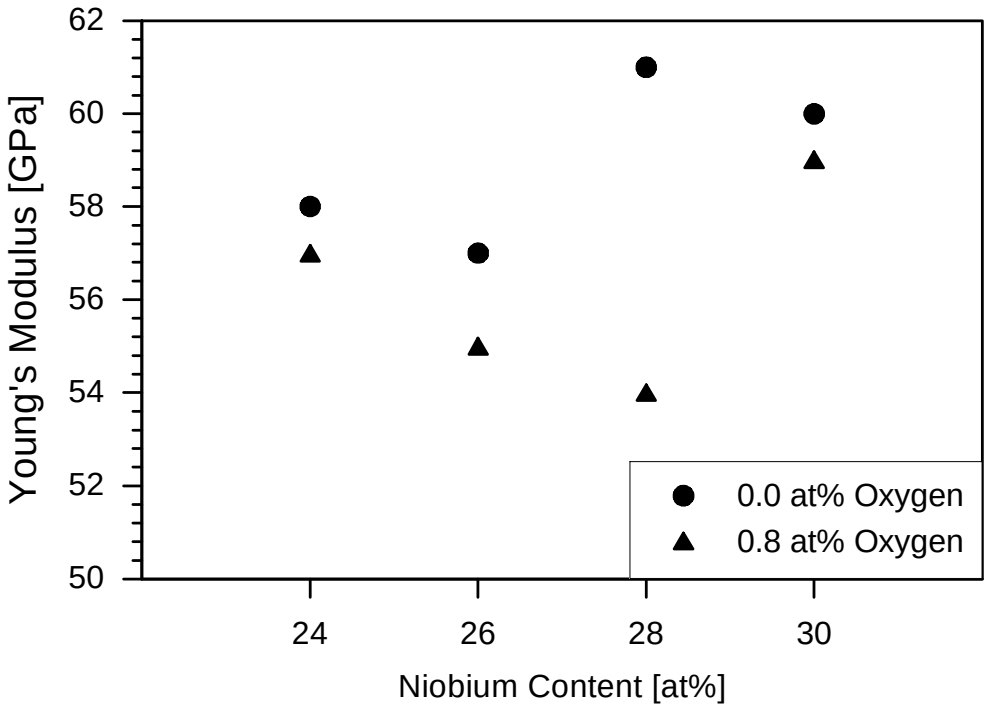

Figure 2-8: Effect of Oxygen on Elastic Modulus of Metastable Ti-Nb-O Based Alloys [45].

upon heating of the β + ω microstructure developed during water quenching, the ω_a embryos persist in a steady state equilibrium with the matrix. When the temperature is increased above the ω solvus temperature, fewer ω_a particles remain, suggesting that the dissolution of the ω_a particles takes place over a wide range of temperatures. Since the remaining particles are subject to random compositional fluctuations, those enriched in Ti become a more stable ω structure and can further grow. Assuming that the ω_{iso} particles are formed through the lattice displacement transformation mechanism by De Fontaine [39, 32] and altered by compositional fluctuations to either grow or dissolve could explain Duering et al. experimental observations.

The anomalous temperature dependency of resistivity (dρ/dT) in metastable β titanium alloys during heat up [48-50] has also been shown to be based on the transition between reversion and further growth of ω particles. Based on a thermal cycling experiment, Prima et al. [51-56] showed that, by examining the recovery of the temperature coefficient of resistivity (TCR) combined with HRTEM that in Timetal LCB, the fully reversible displacive growth reaction of the ω phase can be observed up to 150˚C. Above this temperature, short range diffusion alters the composition of some ω particles in such a way that they cannot reversibly transform to the parent β phase.

These observations make the historical differentiation into “athermal” and “isothermal” ω questionable. A better distinction would be reversible- ideal- ω (ω_{rev}) and chemically altered-modulated- irreversible ω (ω_{irr}). Figure 2-10 illustrates the

thermodynamic basis for this “displacement-assisted growth mechanism”. When the alloy composition is near composition B in Figure 10 is enriched in β-stabilizer content so that ω is unstable, a small increase in the amount of Ti content of the ω phase being sufficient to stabilize the ω structure, moving the composition of the ω particle to B. When the composition of B is attained, the ω particle can grow very quickly through the displacive mechanism. Upon subsequent aging, solute elements continue to diffuse from the ω phase into the β matrix, until the compositions denoted A and C on Figure 10 are reached (metastable equilibrium) [46].

The maximum stability temperature for the ω phase, the so called ω-solvus temperature (ω_{sol}), varies among alloy systems; for example it has been evaluated at about 425˚C in Ti-15Mo-5Zr-3Al [58], above 500˚C in β-III [59], at 390˚C in Timetal LCB [60] and between 300 and 350˚C in B-C [61]. Moreover, the stability range of ω phase is affected by alloying elements. Increasing amounts of α-stabilizers decreases the stability of the ω_{irr} phase reduced through earlier α nucleation [6, 7, 26, 62]. In contrast, increasing β-stabilizers increases the volume fraction of ω_{irr}. Alloying content in general can also suppress the ω_{rev} formation below room temperature [63, 64]. Aging at temperatures above the ω-solvus results in a rapid drop of ω_{irr} volume fraction and particle size until ω_{irr} no longer exists. Upon aging at temperatures below the ω-solvus both ω_{irr} volume fraction and particle size increase with aging time until metastable equilibrium values are reached, the changes occur more rapidly as temperature is increased [12, 62, 64-68].

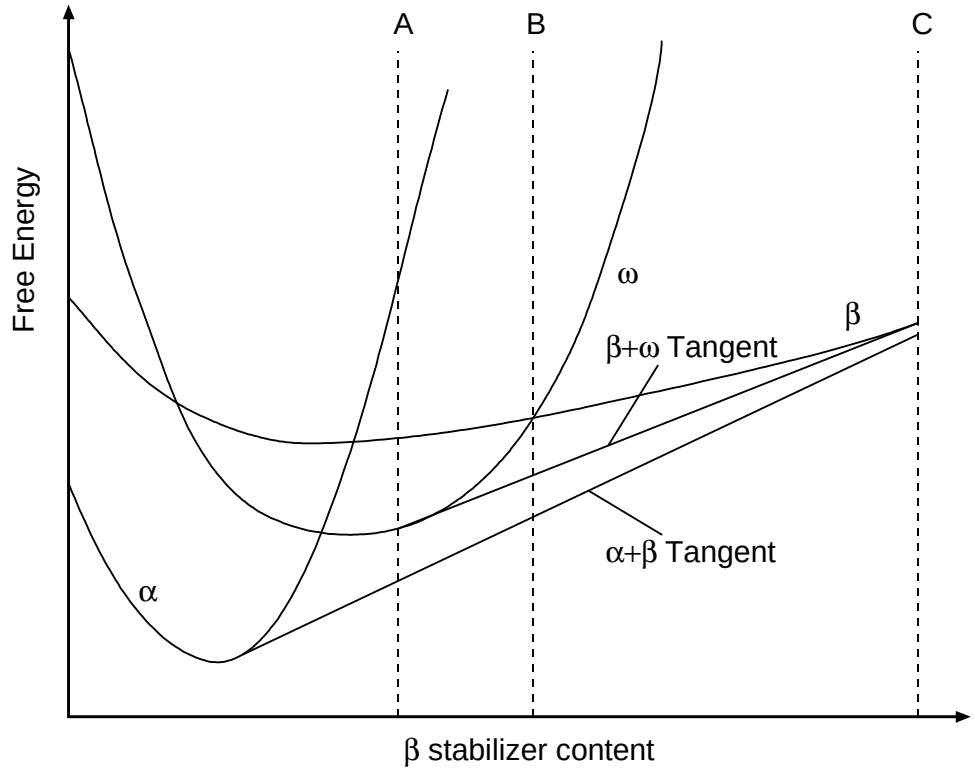

Figure 2-9: Schematic representation of the α, β and ω free energy curves for a hypothetical binary β-stabilized Ti system at a temperature above the athermal ω solvus temperature [46].

At longer aging times or higher temperatures, the ω phase dissolves and the stable α phase is precipitating.

The oxygen content also influences the precipitation of the equilibrium α phase as reported by Rack et al. [41-44]. This precipitation appears with continued aging of a β+ω microstructure. For the metastable β titanium alloy Timetal LCB, different research groups discovered different α nucleation sites with respect to the ω phase and oxygen level: Azimzadeh and Rack [59] reported that α precipitates nucleate at a certain distance from β/ω interface, Figure 2-10 c. On the other hand, Prima et al. [56] found that α particles nucleate within the ω precipitates, Figure 2-10 a. Frasier et al. observed the α/β interface as nucleation origin for the α phase [23], Figure 2-10 b. Qazi et al. also proposed a model that at higher oxygen levels in Ti-35Nb-7Zr-5Ta-xO, oxygen cluster could act as α nucleation sites, Figure 2-10 d. This leads to the final focal point which relates the α nucleation to the stability of the ω phase.

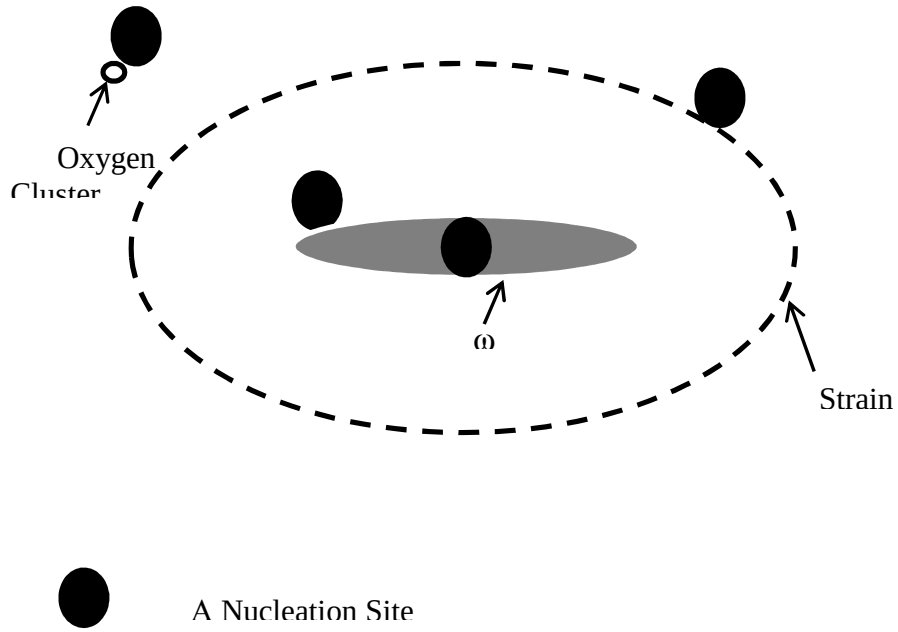

Figure 2-10: A nucleation sites depending on the ω phase and oxygen content [23, 42, 56, 59].

1.2. References

[1] A. W. Bowen, "Ω Phase Formation in Metastable β-Titanium Alloys", in B Titanium Alloys of the 1980´s, ed. R.R. Boyer and H.W. Rosenberg, The Minerals, Metals & Materials Society, Warrendale, PA, 1983: p. 85

[2] C.E. Savrun and D.H. Polonis, "Precipitation and Reversion Process in a B-Titanium Alloy", Material Science and Engineering A, Vol. A119, No. 1-2, (1989), pp. 135-144

[3] M.V. Maltsev and T.N. Volkova, "Thermal Stability of Cold-Worked Titanium Alloys", Metal Science and Heat Treatment, Vol. 27, (1985), pp. 55-58

[4] M.M. Stupel, M. Ron and B.Z. Weiss, "Formation of the ω-Phase During the Aging of B Ti-7.1wt%Fe – A Moessbauer Study", Metallurgical Transactions A, Vol. 9A, No. 2, (1978), pp. 249-252

[5] G. Lütjering and J. C. Williams, "Titanium", Springer 2003: pp. 13-48

[6] T.W. Duering and J.C. Williams, "Overview: Microstructure and Properties of B Titanium Alloys", in B Titanium Alloys of the 1980´s, ed. R.R. Boyer and H.W. Rosenberg, The Minerals, Metals & Materials Society, Warrendale, PA, (1983):pp. 19-67

[7] S. Akem and S. R. Seagle: "Heat Treatment of Metastable B Titanium Alloys", in B Titanium Alloys in the 1980´s, ed. R. R. Boyer and H. W. Rosenberg, The Metallurgical Society of AIME, 1983, pp. 107-126

[8] C. Leyens and M. Peters, "Titanium and Titanium Alloys", Wiley-VCH, Berlin, 2003: 1-39

[9] J. M. Murray, "Ti -V", in Phase Diagrams of Binary Titanium Alloys, ed. J. M. Murray, ASM International (1987): p. 319

[10] P.S. Rudman, "An X-Ray Diffuse-Scattering Study of the Nb-Ti B.C.C. Solution", Acta Metallurgica, Vol. 12, (1964), pp. 1381-1388

[11] J.M. Murray, "Mo-Ti", in Phase Diagrams of Binary Titanium Alloys, ed. J. M. Murray, ASM International (1987): p. 169

[12] T. Furuhara, T. Makino, Y. Idei, H. Ishigaki, A. Takada and T. Maki, "Morphology and Cristallography of α Precipitates in β Ti-Mo Binary Alloys", Materials Transactions, JIM, Vol. 39, No. 1, (1998), pp. 31-39

[13] D.L. Moffat and D. C. Larbalestier, "Competition between Martensite and Ω in Quenched Ti-Nb Alloys", Metallurgical Transactions A, Volume 19A, 1988: p. 1677

[14] K.K. Kharia and H.J. Rack, "Martensitic Phase Transformation in IMI 550 (Ti-4Al-4Mo-2Sn-0.5O), Metallurgical and Materials Transactions A, Volume 32A, March 2001: p. 671

[15] P.J. Bania, "B Titanium Alloys and Their Role in the Titanium Industry", in B Titanium Alloys in the 1990's, ed. R.R. Boyer and H.W. Rosenberg, The Minerals, Metals & Materials Society, Warrendale, Ny, (1993), pp. 3-14

[16] J.J. Polmear, "Titanium Alloys", in Light Alloys, Edward Arnold Publications, London, UK, (1981), p. 165

[17] B.Y. Kokuoz, Y. Kosaka and H.J. Rack, "High-Cycle Fatigue Crack Initiation and Growth in TIMETAL LCB", Journal of Materials Engineering and Performance, Vol. 14 (6), 2005: 773-777

[18] R. Davis, H.M. Flowers and D.R.F. West, "Martensitic transformations in Ti-Mo alloys", Journal of Materials Science, Vol. 14, (1979), pp. 712-722

[19] R. Davis, H.M. Flower and D.R.F. West, "Martensite Formation and Decomposition in Alloys of Titanium containing β-stabilizing Elements", in Titanium and Titanium Alloys - Science & Technology, ed. Williams and Belousov, Vol. 3, Plenum Press, (1982), pp.1703-1715

[20] S. Nag, A. Devaraj, R. Srinivasan, R.E.A. Williams, N. Gupta, G.B. Viswanathan, J.S. Tiley, S. Banerjee, S.G. Srinivasan, H.L. Fraser and R. Banerjee, "Novel Mixed-Mode Transition Involving a Composition-Dependent Displacive Component", Physical Review Letters, Vol. 106, (2011), pp. 245701-1-245701-4

[21] R. Srinivasan, R. Banerjee, S. Nag, J.Y. Hwang, J. Tiley and H.L. Fraser, "The Use of Advanced Characterization to Study Transitions across Solid State Interfaces", JOM, Vol. 62, No. 12, (2010), pp. 64-69

[22] H.P. Ng, A. Devaraj, S. Nag, C.J. Bettles, M. Gibson, H.L. Fraser, B.C. Muddle and R. Banerjee, "Phase separation and formation of ω phase in the β matrix of a Ti-V-Cu alloy", Acta Materialia, Vol. 59, (2011), pp. 2281-2991

[23] A. Devaraj, S. Nag, R.E.A. Williams, S. Banerjee, R. Banerjee and H.L. Fraser, "Experimental evidence of concurrent compositional and structural instabilities leading to ω precipitation in titanium-molybdenum alloys", Acta Materialia, Vol. 60, (2012), pp. 596-609

[24] T. Furuhara, T. Makino, Y. Idei, H. Ishigaki, A. Takada and T. Maki, "Morphology and Cristallography of α Precipitates in β Ti-Mo Binary Alloys", Materials Transactions, JIM, Vol. 39, No. 1, (1998), pp. 31-39

[25] A. W. Bowen, "Ω PHASE EMBRITTLEMENT IN AGED Ti-15%Mo", Scripta Met. Vol. 5, (1971): p. 709

[26] A.W. Bowen, "Ω Phase Formation in Metastable β-Titanium Alloys", in B Titanium Alloys of the 1980´s, ed. R.R. Boyer and H.W. Rosenberg, The Minerals, Metals & Materials Society, Warrendale, PA, 1983: p. 85

[27] B.Y. Kokuoz, J. Hudson and H.J. Rack, "Anisothermal A Phase Precipitation in Ti-3Al-8V-6Cr-4Zr-4Mo (Ti-38644)", in Ti-2007 Science and Technology, ed. M. Ninomi, S. Akiyama, M. Ikeda, M. Hagaiwara and K. Maruyama, The Japan Institute of Metals, (2007), pp. 969-972

[28] M. Gheorghe, J.I. Qazi and H.J. Rack, "Anisothermal A Phase Formation in Ti-6.8Mo-4.5Fe-1.5Al", in Ti-2003 Science and Technology, ed. G. Luetjering and J. Albrecht, Wiley-VCH, Hamburg, (2004), pp. 1155-1161

[29] C.E. Savrun and D.H. Polonis, "Precipitation and Reversion Process in a B-Titanium Alloy", Material Science and Engineering A, Vol. A119, No. 1-2, (1989), pp. 135-144

[30] M.V. Maltsev and T.N. Volkova, "Thermal Stability of Cold-Worked Titanium Alloys", Metal Science and Heat Treatment, Vol. 27, (1985), pp. 55-58

[31] M.M. Stupel, M. Ron and B.Z. Weiss, "Formation of the ω-Phase During the Aging of B Ti-7.1wt%Fe – A Moessbauer Study", Metallurgical Transactions A, Vol. 9A, No. 2, (1978), pp. 249-252

[32] J.C. Williams, "Precipitation in Titanium-Base Alloys", in Precipitation Processes in Solids, ed. K.C. Russel and H.I. Aaronson, AIME, NY, (1978), pp. 191-221

[33] B.S. Hickmann, "Ω Phase Precipitation in Alloys of Titanium with Transient Metals", Trans. Met. Soc. AIME, Vol. 245, (1969), pp. 1329-36

[34] S.L. Sass, “The Structure and Decomposition of Zr and Ti BCC Solid Solutions”, Journal of the Less Common Metals, Vol. 28, (1972), pp. 157-173

[35] P.D. Frost, W.M. Parris, L.L. Hirsch, J.R. Doig, C.M. Schwartz, “Isothermal transformation of titanium-chromium alloys”, Trans. Am. Soc. Metals, 46 (1954), p. 231

[36] J.M. Silcock, “An X-ray examination of the to phase in TiV, TiMo and TiCr alloys”, Acta Metallurgica, Vol. 6, (1958), pp. 481-493

[37] M.J. Blackburn and J.C. Williams, “Phase Transformations in Ti-Mo and Ti-V Alloys”, Trans. Met. Soc. AIME, Vol. 242, (1968), pp. 2461-2469

[38] J.C. Williams, D. De Fontaine and N.E. Paton, “The ω-Phase as an Example of an Unusual Shear Transformation”, Metallurgical Transactions A, Vol. 4, (1973), pp. 2701-2708

[39] D. De Fontaine, “Simple models for the ω phase transformations”, Met. Trans., Vol. 19A, (1988): pp. 169-175

[40] N.E. Paton and J.C. Williams, “THE INFLUENCE OF OXYGEN CONTENT ON THE ATHERMAL β-ω TRANSFORMATION”, Scripta Metallurgica, Vol. 7, (1973), p. 647

[41] J.I. Qazi, V. Tsakiris, B. Marquardt and H. J. Rack, “The effect of duplex aging on the tensile behavior of Ti-35Nb-7Zr-5Ta-(0.06-0.7)O alloys”, Ti-2003: Science and Technology, G. Luertjering and J. Albrecht, eds., Wiley-VCH Verlag Gmbh, Weinheim, Germany, pp.1651-1658.

[42] J. I. Qazi, B. Marquardt, L. Allard and H. J. Rack, “Phase transformations in Ti-35Nb-7Zr-5Ta(0.06-0.7)O alloys”, Material Sci. & Eng., Vol. C25 389(2005).

[43] J. I. Qazi, V. Tsakris, B. Marquardt and H. J. Rack, “Effect of aging treatments on the tensile properties of Ti-35Nb-7Zr-5Ta(0.06-0.7)O alloys”, Jn ASTM(JAI),Vol. 2, #8,19(2005).

[44] T. Ahmed, M. Long, J. Silvestri, C. Ruiz and H.J. Rack, “A New Low Modulus, Biocompatible Titanium Alloy”, in Ti-95 Science and Technology, ed. P. Blenkinsop, W.J. Evans and H.M. Flower, The Institue of Materials, (1996), pp. 1760-1767

[45] W. Kim and H. Kim, “Effect of Oxygen on Elastic Modulus and Mechanical Property of Metastable TiNbO Based Alloys”, Key Engineering Materials, Volume 343-343, (2007), pp. 549-557

[46] T.W. Duering, G.T. Terlinde and J.C. Williams, “Phase Transformations and Tensile Properties of Ti-10V-2Fe-3Al”, Metallurgical Transactions A, Vol. 11A, (1980), pp. 1987-1998

[47] D. De Fontaine, “Mechanical Instabilities in the B.C.C. Lattice and the β to ω Phase Transformation”, Acta Metallurgica, Vol. 18, (1970) PP. 275-279

[48] J.C. Ho and E.W. Collings, “Anomalous electrical resistivity in Titanium – Molybdenum alloys”, Phys. Review B, Vol. 6-10, (1972), pp. 3727-3736

[49] E.W. Collings, “The metal physics of Titanium alloys”, in Titanium ’80, Science & Technology, Vol. I, Kyoto, Japan, (1980), pp. 77-132

[50] M. Ikeda, S.Y. Komatsu, T. Sugimoto and K. Kamei, “Negative temperature dependence of electrical resistivity in Ti-Mo binary alloys”, Proceeding of the 6th World Conference on Titanium, ed. P. Lacombe, R. Tricot and , Vol. 1, (1989), pp. 313

[51] F. Prima, P. Vermaut, D. Ansel, M. Boliveau, H. Francillette and J. Debuigne: “Phase Transformations in Ti-6.8Mo-4.5Fe-1.5Al”, in Titanium’99: Proceedings of the 9th World Conference on Titanium, St. Petersburg, Russia, (1999), pp. 107-114

[52] F. Prima, J. Debuigne, M. Boliveau and D. Ansel, “Control of ω phase volume fraction precipitation in a β titanium alloy: Development of an experimental method”, Journal of Material Science Letters, Vol. 19, (2000), pp. 2219-2221

[53] F. Prima, P. Vermaut, D. Ansel and J. Debuigne, “ω Precipitation in a B Metastable Titanium Alloy, Resistometric Study”, Mater. Trans. , JIM, Vol. 41, No 8, (2000), pp. 1092-1097

[54] F. Prima, P. Vermaut, T. Gloriant, J. Debuigne and D. Ansel, “Experimetal evidence of elastic interaction between ω nanoparticles embedded in a metastable β titanium alloy”, Journal of Material Science Letters, Vol. 21, (2002), pp. 1935-1937

[55] J. Debuigne and F. Prima, “Growth Kinetic Model for Isothermal Ω Phase Particles in Low-Cost B Titanium Ti-6.8Mo-4.5Fe-1.5Al”, Mater. Trans., JIM, Vol. 46, No. 6, (2005), pp. 1433-1435

[56] Prima F, Vermaut P, Texier G, Ansel D, Gloriant T., “Evidence of α-nanophase heterogeneous nucleation from ω particlesbin a β-metastable Ti-based alloy by high-resolution electron microscopy“ Scripta Materialia, Vol. 54, (2006), pp. 645-648

[57] T. Gloriant, G. Texier, F. Sun, I. Thibon, F. Prima and J.L. Soubeyroux, “Characterization of nanophase precipitation in a metastable β titanium-based alloy by

electrical resistivity, dilatometry and neutron diffraction“, Cripta Materialai, Vol. 58, (2008), pp. 271-274

[58] T. Nishimura, M. Nishigaki and H. Kusamichi, “Aging Chararcteristics of B Titanium Alloys”, Titanium and Titanium Alloys – Scientific and Technological Aspects, ed. J.C. Williams and A.F. Belov, Plenum Press, NY, Vol. 3, (1982), pp. 1675-1689

[59] V.A. Belogzov and A.A. Popov, “Decomposition of the Metastable Solid Solution in a B Titanium Alloys”, The Physiscs of Metals and Metallography, Vol. 63, No. 2, (1987), pp. 123-129

[60] S. Azimzadeh and H.J. Rack, “Phase Transformations in Ti-6.8Mo-4.5Fe-1.5Al”, Metallurgical and Materials Transactions A, Vol. 29, No. 10, (1998), pp. 2455-2467

[61] T.J. Headley and H.J. Rack, “Phase Transformations in Yi-3Al-8V-6Cr-4Zr-4Mo”, Metallurgical Transactions A, Vol. 10A, (1979), pp. 909-919

[62] J.C. Williams, B.S. Hickmann and D.H. Leslie, “The Effect of Ternary Additions on the Decomposition of Metastable B-Phase Titanium Alloys”, Metallurgical Transactions, Vol. 2, (1971), pp. 477-484

[63] E. Sukedai, H. Matsumoto and H. Hashimoto, “Electron microscopy study on Mo content dependence of β to ω phase transformation due to cooling in Ti-Mo alloys”, Journal of Electron Microscopy, Vol. 51, (2002), S143-S147

[64] B. S. Hickmann, “Precipitation of Ω Phase in Titanium-Vanadium Alloys”, Journal Institute of Metals, Volume 96, 1968: p. 330

[65] E. Sudekai, H. Hashimoto, T. Horiuchi and M. Shimoda, “Influence of solute elements upon formation of aged ω-phase crystals in β-titanium alloys”, in Metallurgy and Technology of practical Titanium Alloys, ed. S. Fujishiro, D. Eylon anf T. Kishi, The Minerals, Metals & Materials Society, Warrendale, PA, 1994: p. 71

[66] F. Langmayr, P. Fratzl and G. Vogl, “Crossover from ω-phase to α-phase precipitation in bcc Ti-Mo”, Physical Review B, Vol. 49, No. 17, (1994), pp. 11759-11766

[67] P. Fratzl, F. Langmayr, G. Vogl and W. Miekeley, “THE GROWTH OF ω-PHASE INCLUSIONS IN Ti-20 at% Mo AND THE COMPOSITION BETWEEN ELASTIC AND SURFACE ENERGIES”, Acta Metall., Vol. 39, No. 5, (1991), pp. 753-761

[68] A.W. Bowen, “On the Strengthening of a Metastable B Titanium Alloy by Ω and A Precipitation”, in Titanium ’80, Science & Technology, ed. H. Kimura and O. Izumi, TMS of AIME, Warrendale, PA, Vol. I, (1980), pp. 1317-1326

CHAPTER THREE

3. METHODOLOGY

3.1. Material

Two series of Ti-Mo alloys, one provided by ATI Allvac, Monroe, North Carolina as commercially produced α + β warm rolled bar the other by GfE, Erlangen, Germany as as-casted 100 gm vacuum-arc melted buttons, were examined in this investigation, Table 3-1. The latter ones were prepared from high-purity, 99.99%, titanium, titanium oxide and molybdenum powder by double vacuum arc melting in a water cooled copper crucible, the buttons being turned after each melt step.

Figure 3-1 illustrates the microstructures of the α + β processed material. The lowest, 0.15O bar exhibited a non-uniform prior β grain structure (2 μm average grain size) with triple point α, elongated grain boundary α and secondary, intragranular α. Triple point nucleated α displayed a triangular shape, while grain boundary α tended to be elliptical. The intermediate 0.35O bar, exhibited a more uniform and finer prior β grain structure (1.1 μm average grain size) and a higher volume fraction of α. Furthermore the triple point nucleated α particles appeared to be more numerous and smaller in size, while the grain boundary α phase appeared to be thinner and more continuously distributed, with extensive precipitation of intragranular α also being observed within the prior β matrix. Finally the highest oxygen α + β bar had the most uniform and finest prior β grain structure (560 nm average grain size). The triple point

Table 3-1: Chemical composition of Ti-Mo-O alloys.

Element	Ti	Mo	O	Fe	H	Ni
PO75	33.5 mm diameter bar					
Atomic %	bal.	7.78	0.39	-	-	-
Weight %	bal.	14.85	0.15	0.02	0.0017	0.0015
203F	44.5 mm diameter bar					
Atomic %	bal.	7.72	1.22	-	-	-
Weight %	bal.	14.54	0.34	0.026	0.0008	0.0008
204F	38.1 mm diameter bar					
Atomic %	bal.	7.78	1.63	-	-	-
Weight %	bal.	14.57	0.49	0.028	0.0032	0.0032
Ti-15Mo-1O	Button					
Atomic %	bal.	7.9	3.1	-	-	-
Weight%	bal.	14.92	0.92	0.017	0.001	0.003
Ti-35Mo-0.2O	Button					
Atomic %	bal.	21	0.7	-	-	-
Weight%	bal.	34.87	0.18	0.019	0.001	0.004

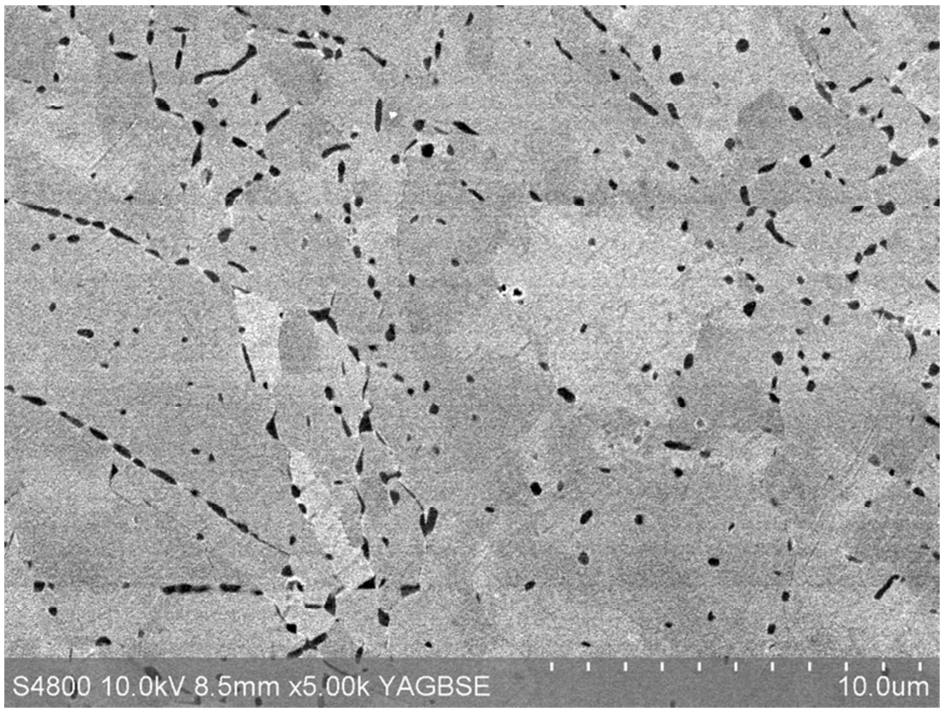

(a)

Figure 3-1: Microstructure of the as-received (a) Ti-15Mo-0.15O, (b) Ti-15Mo-0.35O and (c) Ti-15Mo-0.5O.

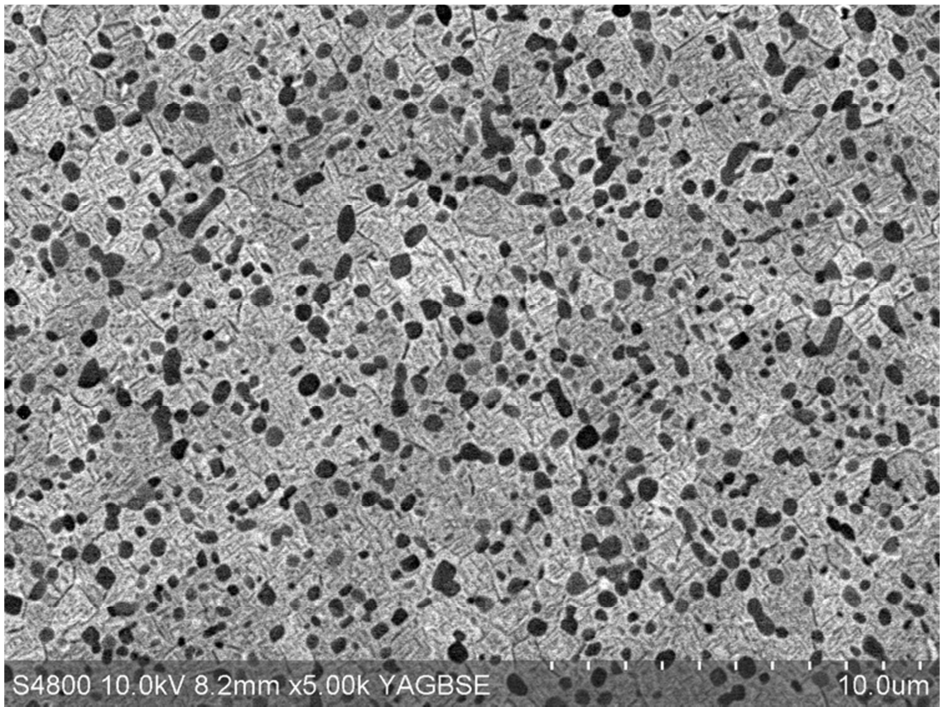

(b)

Figure 3-1: continued

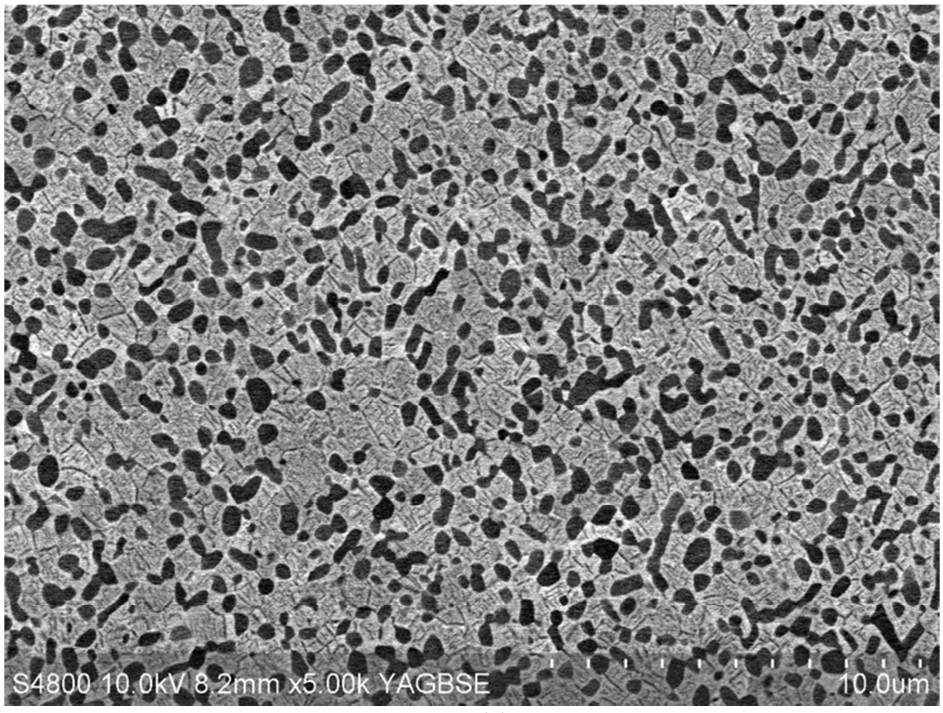

(c)

Figure 3-1: continued

and grain boundary α appeared to be somewhat larger and more circular in shape, several examples of a necklace α structure were being seen in this micrograph, with needle shaped intragranular α phase within the β matrix.

3.2. Heat Treatment

3.2.1 A-B Solution Treatment and Aging

Ten(10) mm thick slices of the Ti-15Mo-(0.15-0.5) O were removed from the as received α + β bar, coated with Y_2O_3, Figure 3-2 a-c, and solution treated at 732˚C, Ti-15Mo-0.15O, or 760˚C, Ti-15Mo-0.35O and Ti-15Mo-0.5O, for 110 minutes followed by water quenching (WQ) [1]. After solution treatment these slices were quartered, recoated with Y_2O_3 and artificially aged, Figure 3-2 c, in a recirculating air furnace at temperatures between 400 to 550°C for times up to 512 hours, the aging process being terminated by air cooling (AC). Both furnaces used were mapped to ensure a homogeneous heat zone using a K-type thermocouple (+/- 2˚C). In addition the heating rates to the solution treatment and aging temperatures as well as cooling rates following heat treatments were monitored by a K-type type thermocouple (+/- 2˚C) located in the center of a dimensionally similar dummy specimen, all time intervals reported herein having commenced when the center of the sample reached either the solution or aging temperature. Figure 3-3 shows that the heating rate to the solution treatment temperature was 90˚C/ min, Figure 3-3 a, while the heating rate to the aging temperatures was 30˚C/ min., Figure 3-3 b. Finally the cooling curves for both, solution

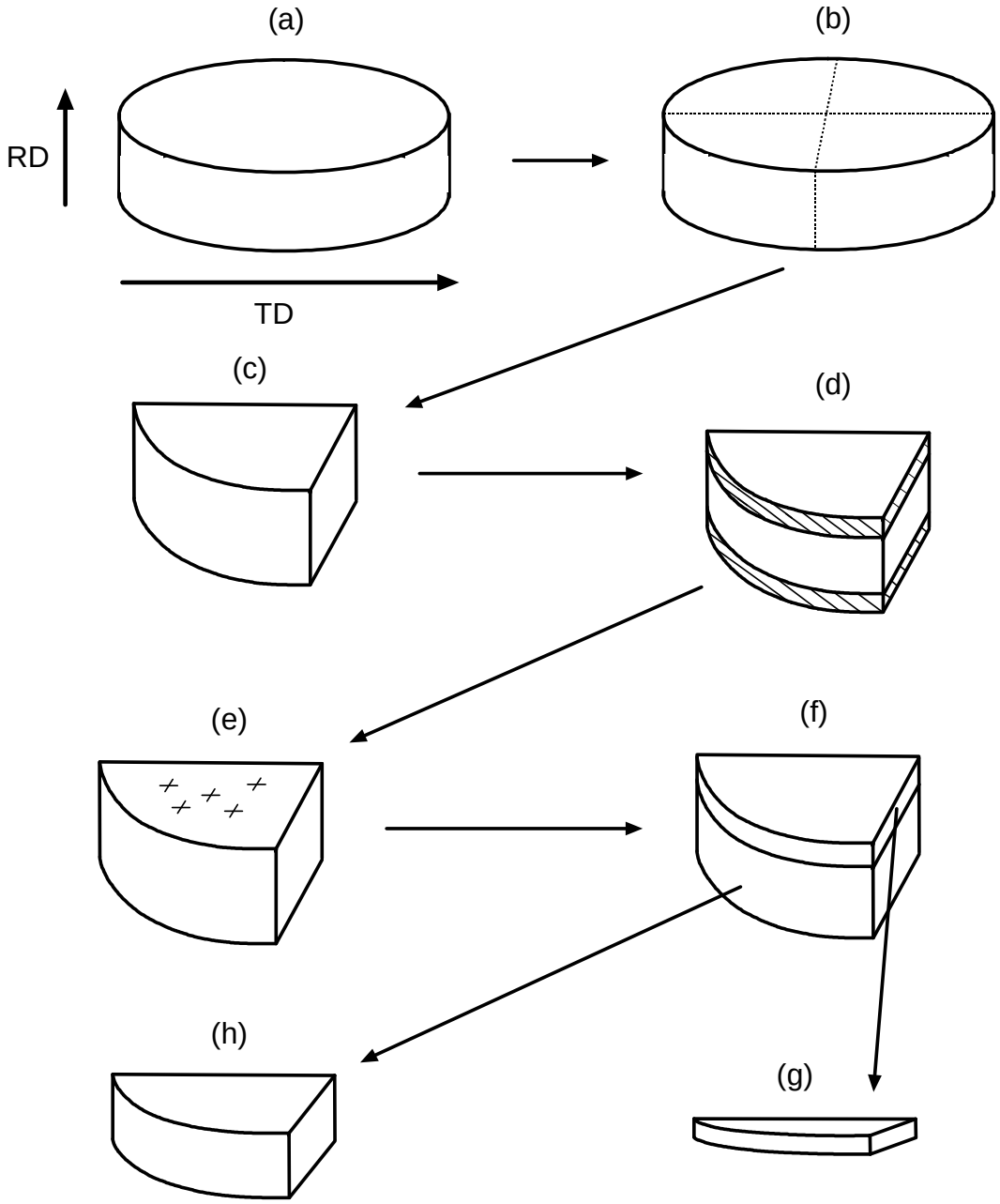

Figure 3-2: Steps of sample preparation: (a) 10 mm bar cut off of the as received material and rolling direction; (b) quartering of solution treated material for further heat treatments; (c) sample geometry used for further heat treatments; (d) grinding of oxidized layers after heat treatment; (e) hardness measurements; (f) wafering of XRD sample from the opposite side of the hardness indents; (g) TEM specimens: (h) XRD sample.

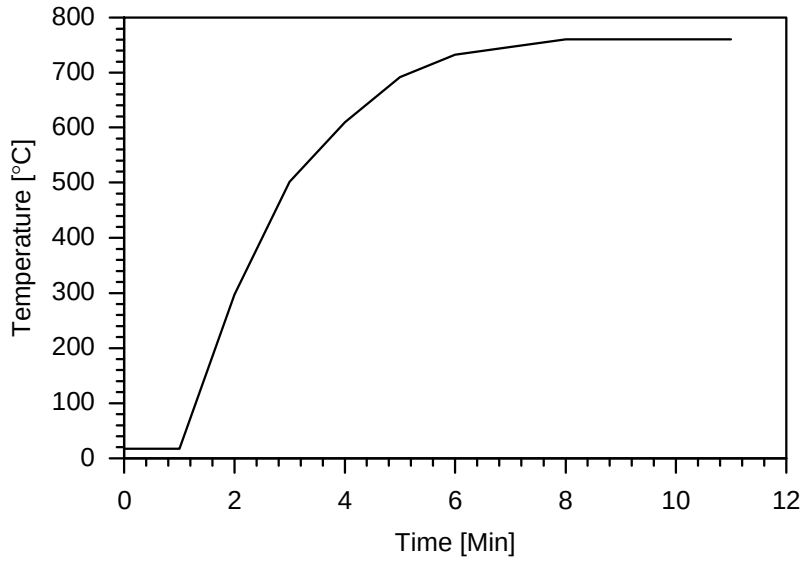

(a)

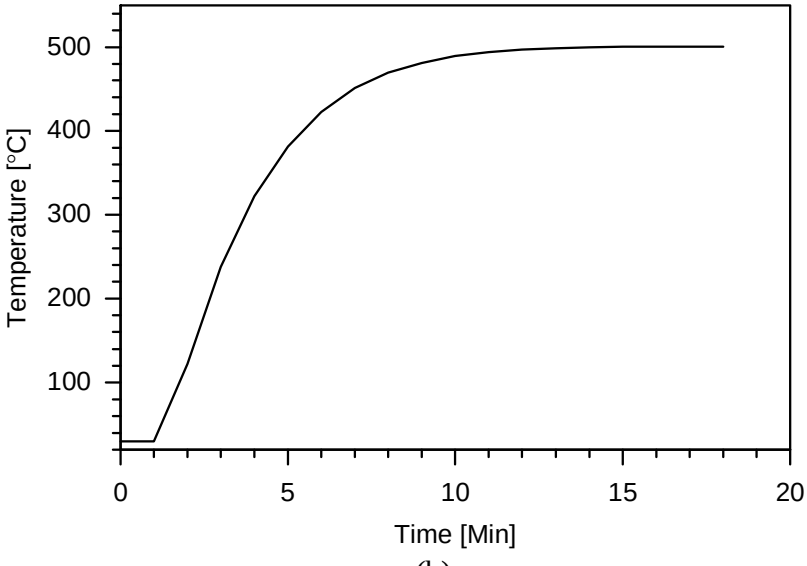

(b)

Figure 3-3: Typical heat transfer curves relevant for Ti-Mo specimens in air furnaces; (a) heating to 760˚C; (b) beating to 500˚C; (c) water quenching from 760˚C; (d) air cooling from 500˚C.

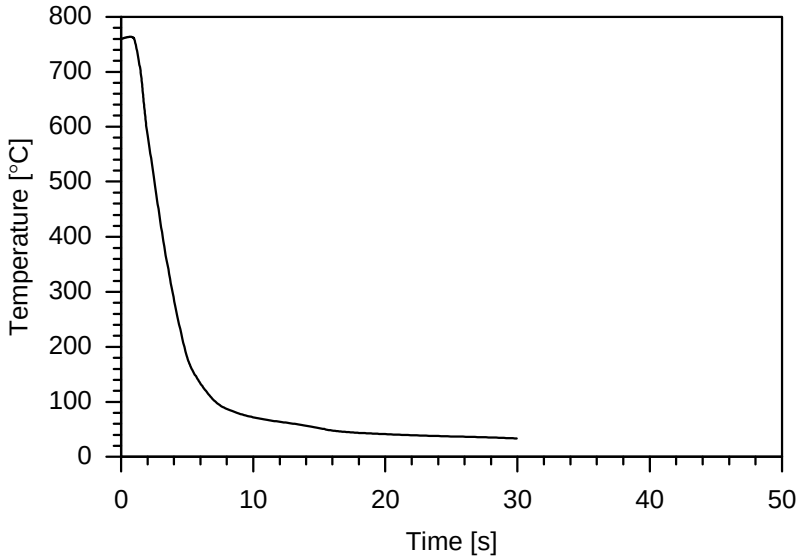

(c)

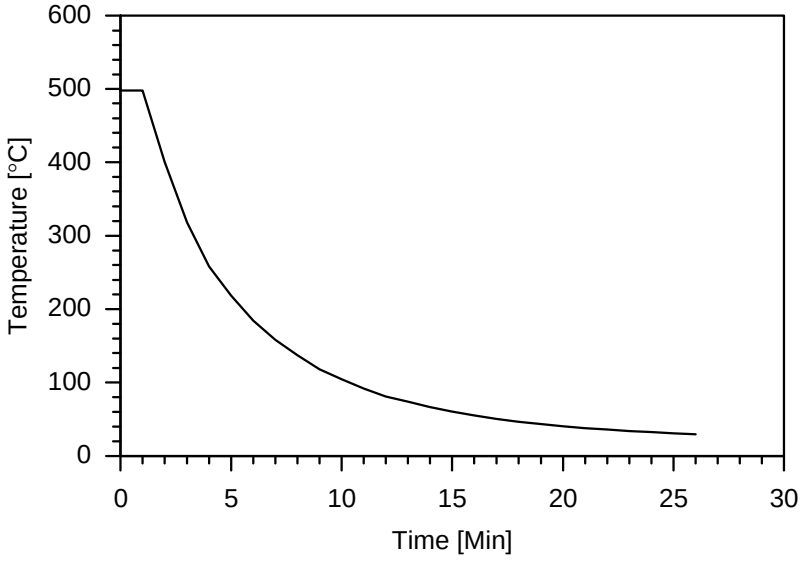

(d)

Figure 3-3: continued

treatment and aging temperature, are shown in Figure 3-3 c and d, water quenching from the solution treatment temperature taking less than a minute, Figure 3-3 c, with air cooling after aging for example from 500˚C, taking approximately 25 minutes.

3.2.2 B Solution Treatment

B solution treatment followed by water quenching was also performed to retain a β + ω microstructure. 10 x 20 x 6 mm sections of Ti-15Mo-(0.12- 1.0) were coated with Y2O3 and β solution treated for 1 hour at temperatures predicted by Pandat calculations which defined the effect of oxygen on the β transus temperature as shown in Figure 3-4.

3.2.3 Single Crystal Growth

Single crystals were grown for the following materials: Ti-15Mo-(0.15/0.5/1.0) O and Ti-35Mo-0.2O. 5 x 5 x 20 mm specimens were cut from each alloy, coated with Y_2O_3 and wrapped in tantalum foil prior to encapsulation. Additionally, each encapsulation vial was filled with titanium chips to getter any remaining oxygen left in the vial. Following vacuum encapsulation in a quartz tube, the samples were treated for 4 (Ti-15Mo-(0.15/0.5) O), 14 (Ti-15Mo-1O) and 38 days (Ti-35Mo-0.2O) at 1195˚C in a tube furnace operated under a dynamic Argon atmosphere. Finally the vials were broken under water to produce a nominal single phase β/β+ω

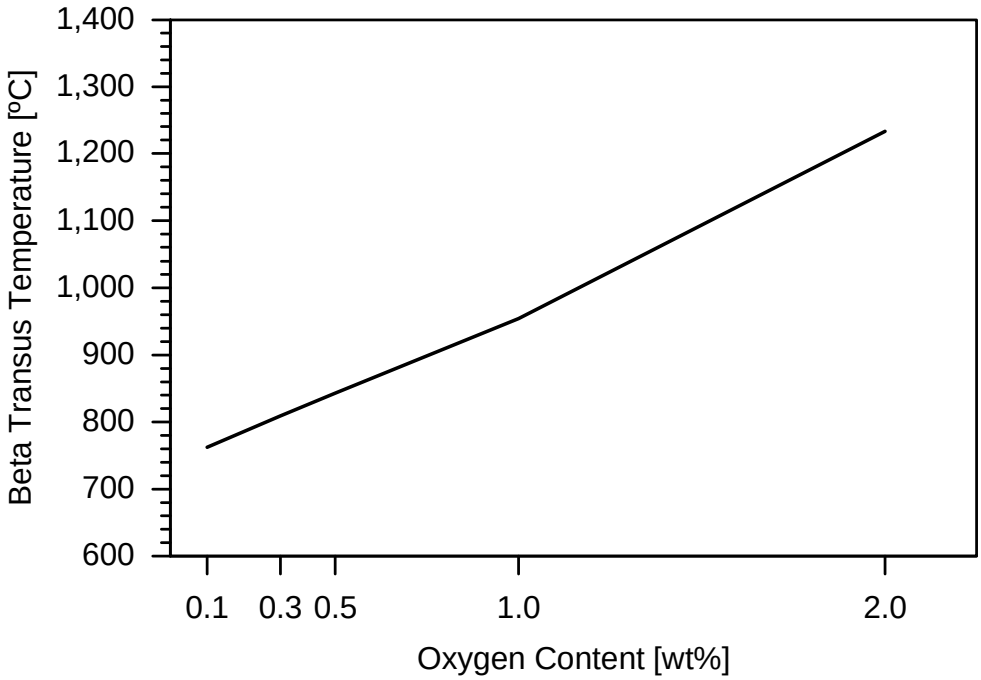

Figure 3-4: Effect of oxygen content on the β-transus temperature for Ti-15Mo.

3.3. Metallography

Metallographic preparation of the solution treated and aged Ti-Mo-O samples involved standard grinding and polishing procedures. The intended examination surface, transverse to the rolling direction, were initially surface ground to remove any α-case oxidized layer that may have formed during heat treatment, Figure 3-2 d, utilizing Buffalo Abrasive® SiC particle-vitrified bonded grinding wheels at a speed of 32 meters/second with a water-oil mixture lubrication. The grinding schedule involved 15 passes of a depth of 0.0254 mm per pass with a 220 grit grinding wheel followed by 20 passes of a 320 grit wheel and 25 passes by 400 grit wheel. 50 passes of 0.01 mm each pass with a 600 grit wheel finished the grinding schedule for a total removal from the top and bottom of each sample of 2.05 mm, Figure 3-2 d, the sample being rotated by 90˚ after each wheel change.

Hardness measurements were performed with a Wilson Instruments® Rockwell C hardness tester at a load of 150 kilograms, the hardness values reported being the average of 5 measurements, Figure 3-2 e, with a standard sample being tested before and after each sample to ensure data validity. After hardness measurements the sample was inverted, this opposite face being utilized for further investigations, Figure 3-2 f. After removal of possible surface contamination by surface grind as described previously the specimen were given a vibratorial polish utilizing a 0.3 and 0.05 µm alumina solution, polishing with a colloidal silica 0.06 µm finishing the operation. As-polished samples were used for XRD or backscatter electron imaging (BSEI), with

thinner slices, 1 mm thick, being prepared for TEM sample, Figure 3-2 g-h. Ultimately site specific sample preparation was carried out using a FEI Dual Beam FIB, Helios NanoLab, combined with a Fishione Instruments Model 1040 NanoMill®.

Finally, preparation of single crystals involved equal removal of material from both sides using 600 and 800 grit SiC paper until a thickness of less than 200 µm was attained. Vibratorial polishing with 0.3 µm, 0.05 µm alumina and colloidal silica completed the process. These samples were etched with Kroll's etchant, 1.5 ml HF, 3.5 ml HNO_3 and 95 ml distilled H_20 to identify the grain structure, a grain near the sample center being isolated using an optical microscope and a scalpel. Samples of 0.75 mm diameter, or smaller, were cut from this grain for single crystal XRD.

3.4. Thermal Analysis

Thermal analysis utilized a Netzsch Pegasus 404 C DSC equipped with a low temperature head (Sample carrier 6.235.4-61/ K-Type Thermocouple, ± 0.5K) and an Ag wound furnace. Prior to commencing the analysis the furnace chamber was repeatedly evacuated < 6 mbar using a vacuum pump and refilled with Ar while maintaining an under ultra-high 1 ppb purity static Ar atmosphere during testing. Isochronal runs at 1˚C, 5˚C, and 50˚C per minute (1CPM, 5CPM and 50CPM) heating rate to temperatures in the range 200-550˚C were initially examined for the β solutionized samples. These were supplemented by isothermal excursions by setting the furnace control in such a manner, that the heating rate was slowly allowed to decrease

commencing at approximately 15˚C below the preselected isothermal temperature, this preventing system overshoot. Aging times up to 24 hours were considered after reaching the isothermal temperature with cooling at 15˚C/min being used to return the system to room temperature, Table 3-2. Isochronal runs for the α + β solution treated Ti-15Mo-(0.15-0.5)O were carried out using 30˚C per minute 30CPM) heating rate, the same heating rate as the air furnace in which the aging study was undertaken. The isothermal runs were carried out at the same temperatures as the aging was carried out: 400˚C, 450˚C, 500˚C and 550˚C for 18 hours followed by furnace cooling. Finally a separate baseline procedure for the isochronal and isothermal sections of the thermal analysis experiments was utilized. The former utilized a sample that had been aged for 512 hours at 550˚C to stabilize the matrix thereby minimizing the formation of the metastable ω phase. Figure 3-6 illustrates the isochronal results for the baseline sample of Ti-15Mo-0.5O, it still exhibited the two peaks during heat-up for the investigated temperature range, although the magnitude had been reduced to a very low level. By using different heating rates, the lag time of the system was determined to be roughly 70˚C for 5 CPM and 150˚C for 30 and 50 CPM. All recorded DSC curves were adjusted for the weight difference of the samples used by superimposing each one of them at the starting point of 70˚C and 150˚C respectively.

The experimental isothermal data was analyzed within the framework of the Johnson-Mehl-Avrami-Komolgorov (JMAK) model, the isothermal baseline being established as $dJ/dt = 0$.

Table 3-2: Calorimetric runs performed at Ti-15Mo-(0.12-2) O β solution treated alloys.

Alloy	Heating rate	Isothermal temperature									Time at isothermal temperature	Cooling rate from isothermal temperature
		200˚C	250˚C	300˚C	350˚C	400˚C	450˚C	500˚C	550˚C	600˚C		
Ti-15Mo-0.12O	5˚C/ min	X	X	X	X	X	X	X	X	X	4 hours/ 12 hours	15˚C/min
	50˚C/ min	-	X	X	X	X	X	X	X	X		
Ti-15Mo-0.15O	5˚C/ min	X	X	X	X	X	X	X	X	-	4 hours/ 12 hours	15˚C/min
	50˚C/ min	-	X	X	X	X	X	X	X	-		
Ti-15Mo-0.35O	5˚C/ min	X	X	X	X	X	X	X	X	-	4 hours/ 12 hours	15˚C/min
	50˚C/ min	-	X	X	X	X	X	X	X	-		
Ti-15Mo-0.5O	5˚C/ min	X	X	X	X	X	X	X	X	-	4 hours/ 12 hours	15˚C/min
	50˚C/ min	-	X	X	X	X	X	X	X	-		
Ti-15Mo-2O	1˚C/ min	X	X	X	X	X	X	X	X	-	12 hours	Furnace cooled
	5˚C/ min	X	X	X	X	X	X	X	X	-		
	50˚C/ min	-	X	X	X	X	X	X	X	-		

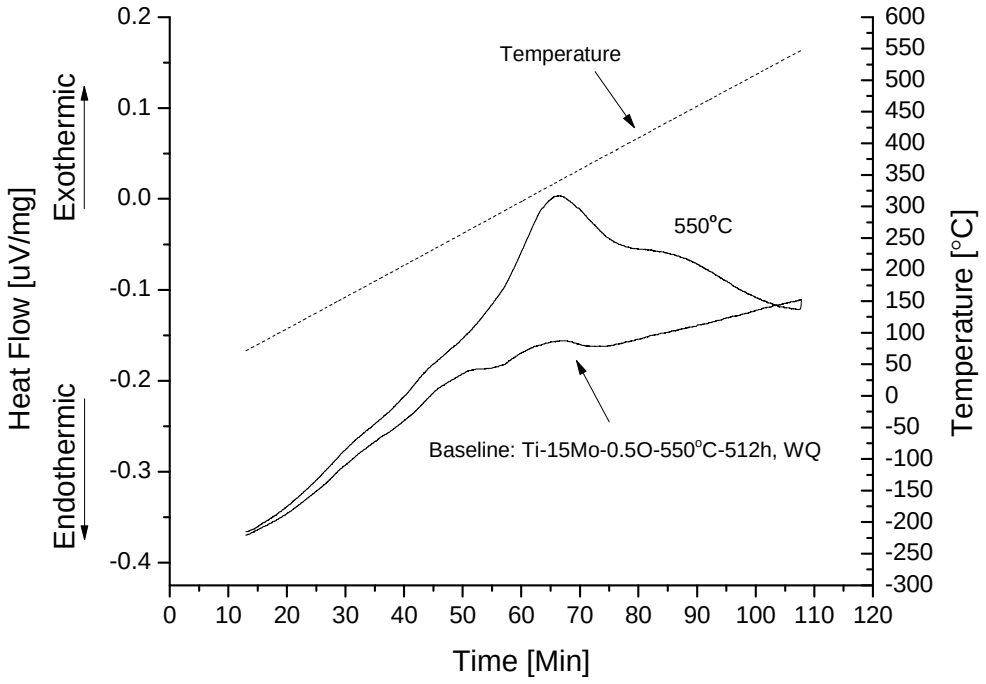

Figure 3-5: Isochronal calorimetric run of Ti-15Mo-0.5O, β solutionized at 927˚C for 1 hours followed by water quenching and baseline run of Ti-15Mo-0.5O, aged at 550˚C for 512 hours followed by water quenching.

3.5. X-Ray Diffraction

Polycrystalline x-ray diffraction measurements were performed with a Scintag XDS-2000 θ- 2θ diffractometer operated at 40 kV and 30 mA. This system was equipped with a Li doped Si Mostek® detector and utilized CuKα radiation (λ=1.54056 Å). Data collection and processing were controlled through the Data Management Software for Windows NT (DMSNT) software program Version 1.37 which allowed linear background removal, $K\alpha_2$ stripping and Pearson VII peak fitting [2]. Based on the Carine simulations, two standalone peaks were used to determine the ω particle size. These peaks were at 51.14˚, hkl of (2-11), and 79.55˚, hkl of (301), 2θ and did not overlap with other peaks Scans from 50.5-53.5˚ and 78-81˚ 2θ were carried out at a step size of 0.005˚ and a scan rate of 0.012˚/min. Following data acquisition, linear background subtraction and $K\alpha_2$ removal, the integrated intensities for each diffraction line was calculated by the DMSNT software based on Pearson VII fitting, with the 2Θ values for each peak being based on the maximum of the Pearson VII fitting. These were subsequently compared to Carine® simulations to establish hkl values for the used reflections and crystal structures considered. After processing the data, an available DSMNT software subroutine as outlined below was used to determine the average ω particle size for each hkl reflection. The broadening of x-ray diffraction lines can occur for several reasons: instrumental effects, diffraction-order-independent (size) and diffraction-order dependent (strain) broadening [4, 5], Figure 3-6. The measured peak

profile h(s) can therefore be considered as the convolution of a function for the pure peak profile f(s) and a function for the instrumental broadening g(s):

$$h(s) = g(s) * f(s) \qquad (11)$$

instrumental broadening g(s) can be treated as the wavelength distribution and geometrical aberrations characteristics of the used instrument. Equation 1 can furthermore be rewritten as a product of the Fourier transform for instrumental broadening F(g) and the pure peak profile F(f):

$$F(h) = F(g) * F(f) \qquad (12)$$

The Warren-Averbach method involves obtaining F(g) from an analysis of a line-width standard, e.g., LaB_6 which allowed F(f) to be found. A subsequent inverse Fourier transformation on F(f) was used to obtain f(s) , peak broadening associated with microstructural strain/ distortion. The result can be written as a Fourier series:

$$f(s) = \sum_{L=-\infty}^{\infty} (A(L)\cos[2\pi\,(s - s_0)L] + B(L)\sin[2\pi\,(s - s_0)L])$$

where A(L) and B(L) are the cosine and sine coefficient and L is the length of a column of unit cells perpendicular to the diffracting planes. A(L) is also called the size coefficient while B(L) is denoted as the distortion coefficient. A plot of the size coefficient, A(L), versus L was used to determine the are average crystallite size <D>, Figure 3-7, the intercept of the initial slope with the x-axis.

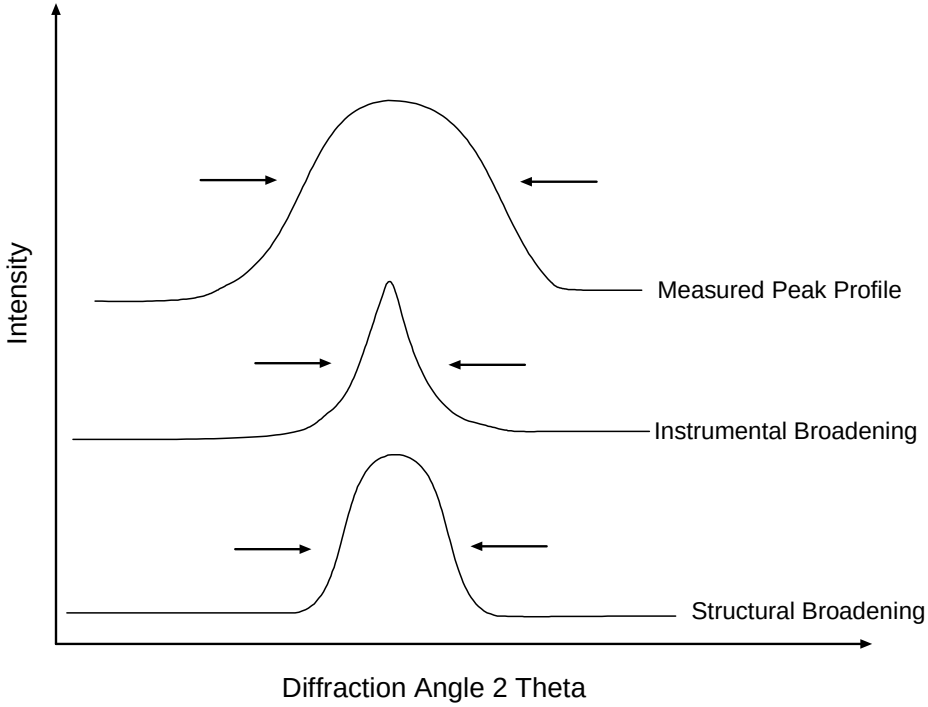

Figure 3-6: Composition of the measured diffraction profile [5].

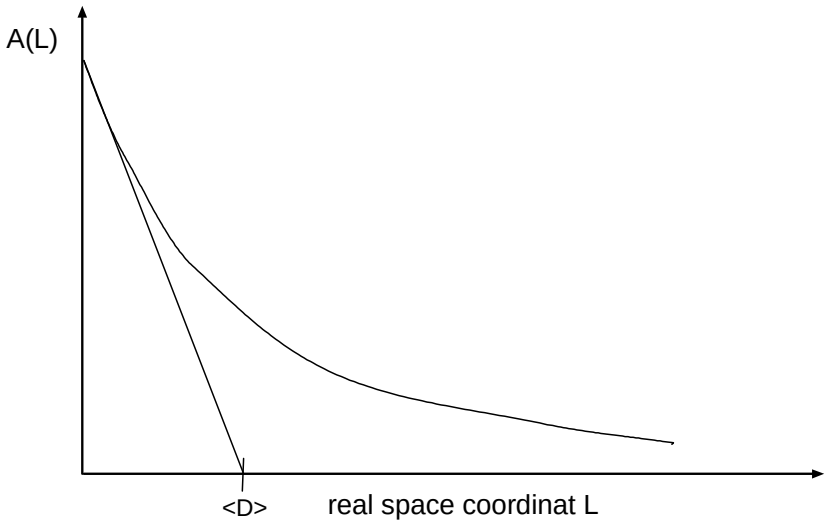

Figure 3-7: Determining the average colum size <D> from the size coefficient plot, Particle size coefficient against L, the real distance along the columns of cells, and the intercept of the initial slope with the x-axis [5]

The data management software (DMSNT) Version 1.37 facilitated background removal and Pearson VII peak fitting for the LaB_6 standard and the 51.14 and 79.55 2Θ standalone ω peaks. The add-on for crystalline size determination was used to determine the particle size from a single peak using the Warren-Averbach approach. In this study, measurement of the LaB_6 standard was made over the range 70-82˚ and 45-65˚ 2 Θ Once combined with the corresponding ω peak run 50-53 and 78-81˚ 2 Θ, the particle sizes were determined in nm.

3.6. Single Crystal X-Ray Diffraction

A Rigaku AFC8 diffractometer equipped with a Mercury CCD area detector, Figure 3-8 E, and Mo Kα (λ=0.71073 Å) radiation generated from a graphite monochromatic tube, and a collimator to narrow the beam to 0.8 mm diameter was used in this study, Figure 3-8 . Single crystals smaller than 0.75 mm in size were placed on a tip of glass fiber using a fast drying epoxy and mounted on a three degrees of rotation, ω, χ and φ, goniometer. A Crystal Clear software package was used to operate the instrument, collect data and integrate the reflections [6], the crystal to detector distance being 27.1 mm for all experiments. Initial crystal screening was performed using 8 scans where ω was varied (8, 16, 24, 32, 40, 48, 56 and 64˚) while χ and φ remained fixed at 0˚. A 5 second exposure time was used for screening purposes. Following this a

preliminary reduced cell was obtained from these scans to ensure single crystalinity. If the crystal was suitable, a full data set consisting of 480 total images was collected, the exposure time for the full data scans being set to 3 seconds. For the first 360 images, ω was scanned from -90˚ to 90˚ in 0.5˚ increments while χ was held at 45˚ and φ held at 0˚. The last 120 images were collected by scanning ω from -30 to 30˚, also in 0.5˚ steps while holding χ at 45˚ and φ at 90˚. After all data was collected it was integrated and a high resolution unit cell obtained, the integrated data being converted into a usable form using the Crystal Clear software. The resulting hkl intensity file was then transferred to the SHELXTL software package [7] for structure determination and refinement with heavy atoms, Mo and Ti, being located using direct methods, with subsequent Fourier peak refinements being used to locate oxygen atoms. For the latter their position was assigned by locating areas of electron density, using the DIAMOND software package [8].

3.7.Scanning Electron Microscopy

A Hitachi 4800 field emission scanning electron microscopy (FESEM) and a FEI Quanta SEM operated under backscattering electron imaging (BSEI) conditions were used to examine the polished unetched specimens. Operating conditions for both SEM's were 10-15 kV and a 4-10 mm working distance.

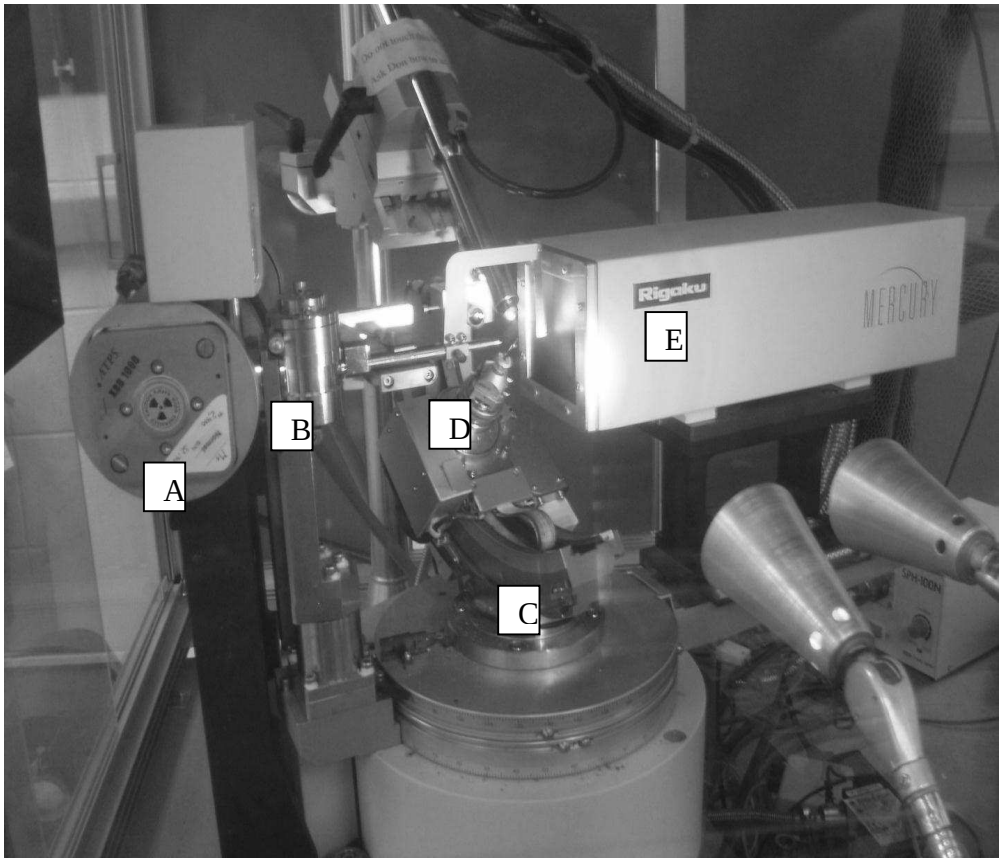

Figure 3-8: Mo-X-Ray source (A), Collimator, 0.8 mm diameter (B), Goniometer (C) with sample in rotatable sample holder (D) and CCD area detector (E).

3.8. Optical Microscopy

Optical microscopy utilized a Nikon Epiphot 300® optical microscope with samples etched using Kroll's reagent (1.5 ml HF, 3 ml HNO_3, bal. dist. H_2O).

3.9. Transmission Electron Microscopy

Focused ion beam (FIB) milling, specifically the lift-out technique, was used to prepare site specific TEM samples [9-12]. Initially the specimen to be examined was metallograhically polished and mounted with Ag paint on the FIB holder, which was tilted to 20˚ from the horizontal for the initial milling operation. After deposition of a platinum line approximately 50 µm long near the area of interest, two large stair-step trenches were cut on both longitudinal sides of the platinum line with a FEI Helios NanoLab FIB at 30 kV and below 50 nA , the final TEM specimen lying benith the protectuive platinum layer. Subsequent to this trenching operation the sample was undercut and trenched on both transversal sites, so that only a small catwalk remained to hold the specimen in place, Figure 3-9. A tungsten needle was welded onto the platinum layer on one side, prior to the catwalks being removed, Figure 3-10. The lifted sample was 180 nm thick and 40 µm long, with the height differing due to the angeled undercut. Typically one side was 10 µm and the opposite being 17 µm, Figure 3-11. Finally thesample was mounted on a copper grit, Figure 3-12, again using a platinum deposit. The site away from the finger was subsequent thinned using 5 kV and below 50

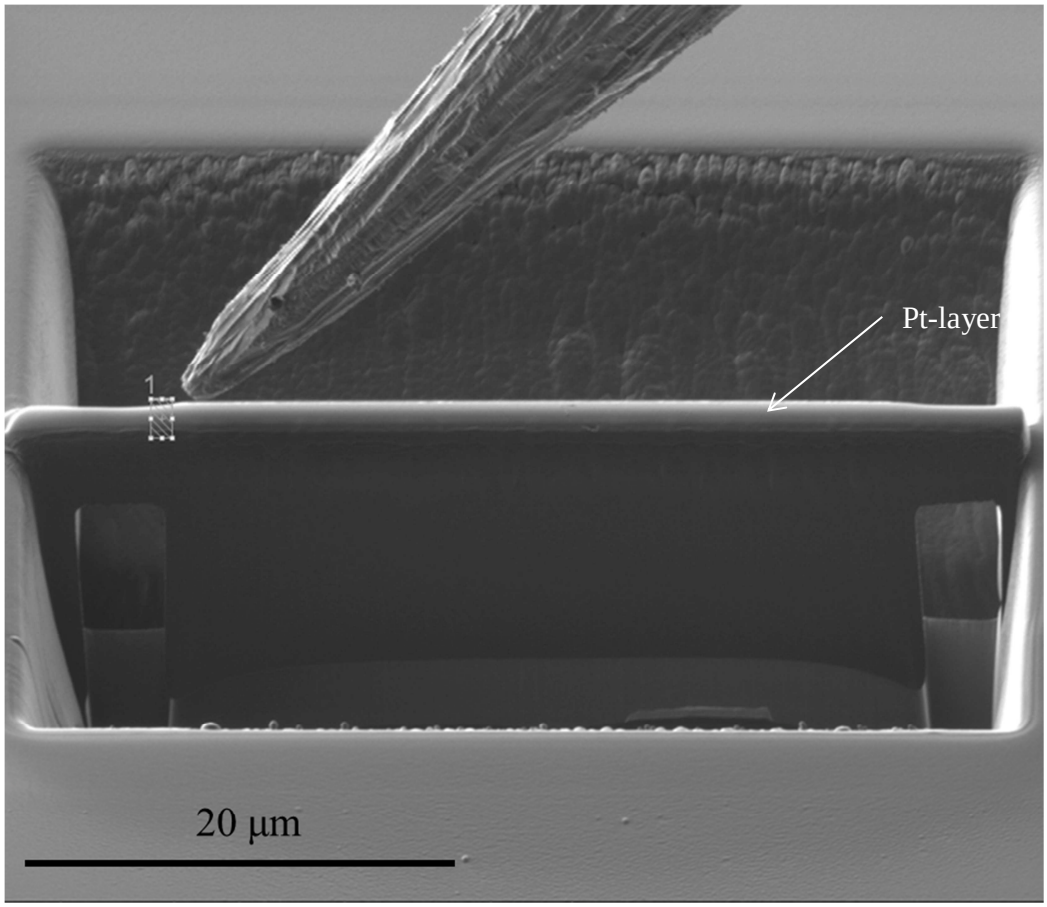

Figure 3-9: Step trenched and undercut specimen with tungsten needle to get attached for lift out.

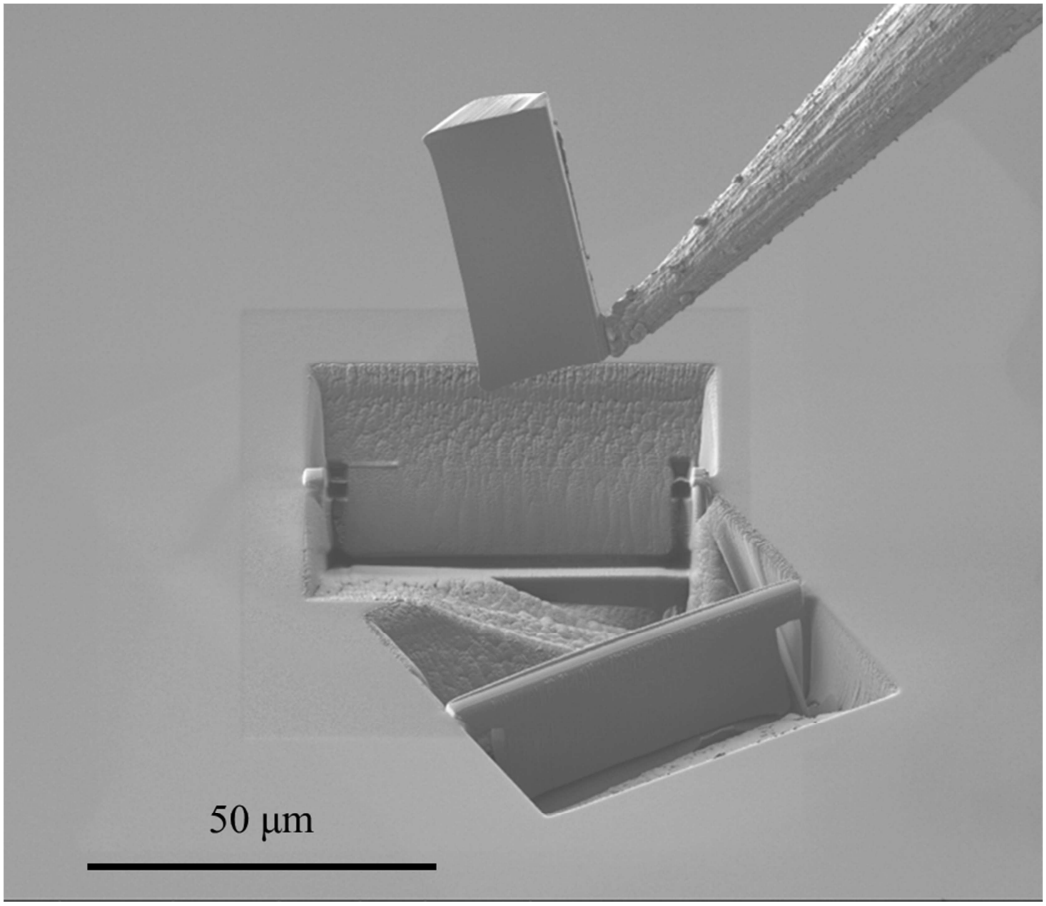

Figure 3-10: Trenched and undercut sample and sample lifted out attached to tungston needle

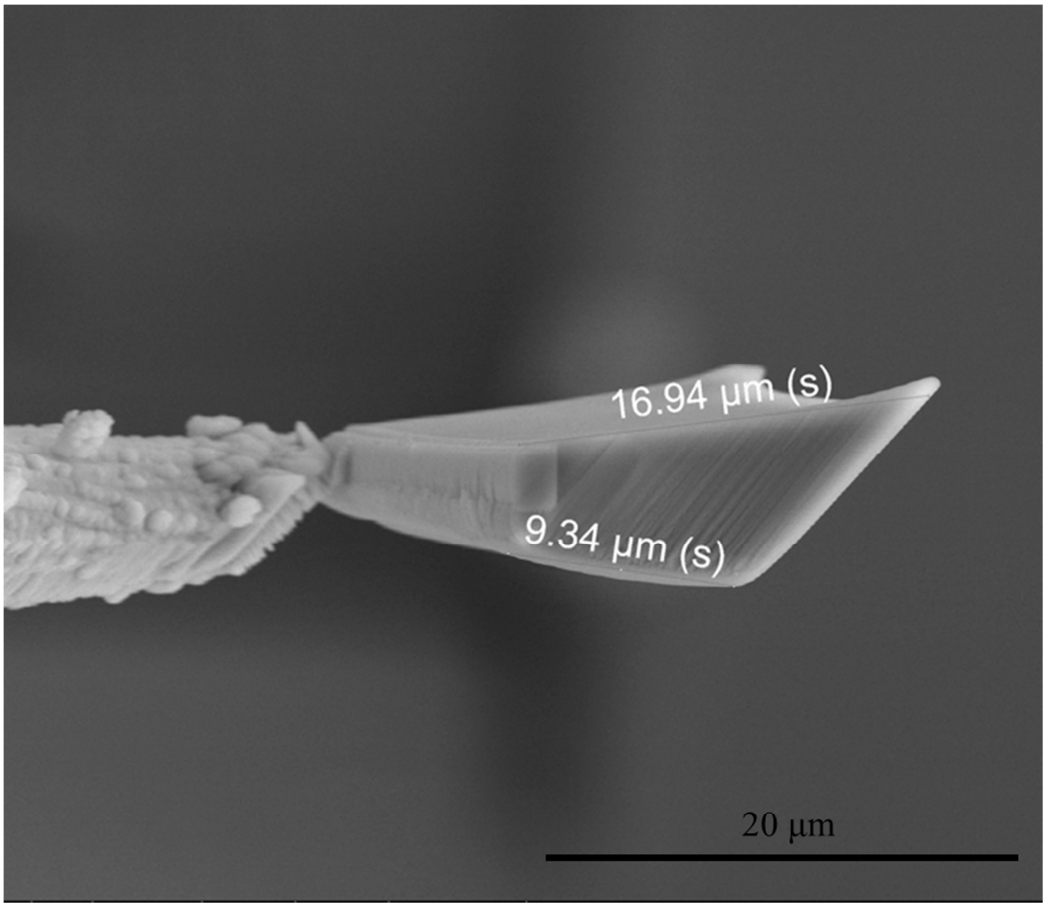

Figure 3-11: Geometry of removed FIB specimen, different height due to undercutting at an angle of 20˚.

pA over a length of 10 µm in multiple steps alternating from each side, removing approximately 100 nm during each step, until a final thickness of 2-300 nm was achieved,the bulk of the sample being left thicker to stabilize the thin area and prevent it from bending, Figure 3-13.

Ultimately after cutting and thinning, a Fishione Nano-mil® operated at 900 eV and low nA was used to remove the amorphous surface layer and any damage associated with the thinning process [7-11], with final observation utilizing a FEI Tecnai® G2 and CM 200 equipped with a double tilt stage and operated at 200-300 kV.

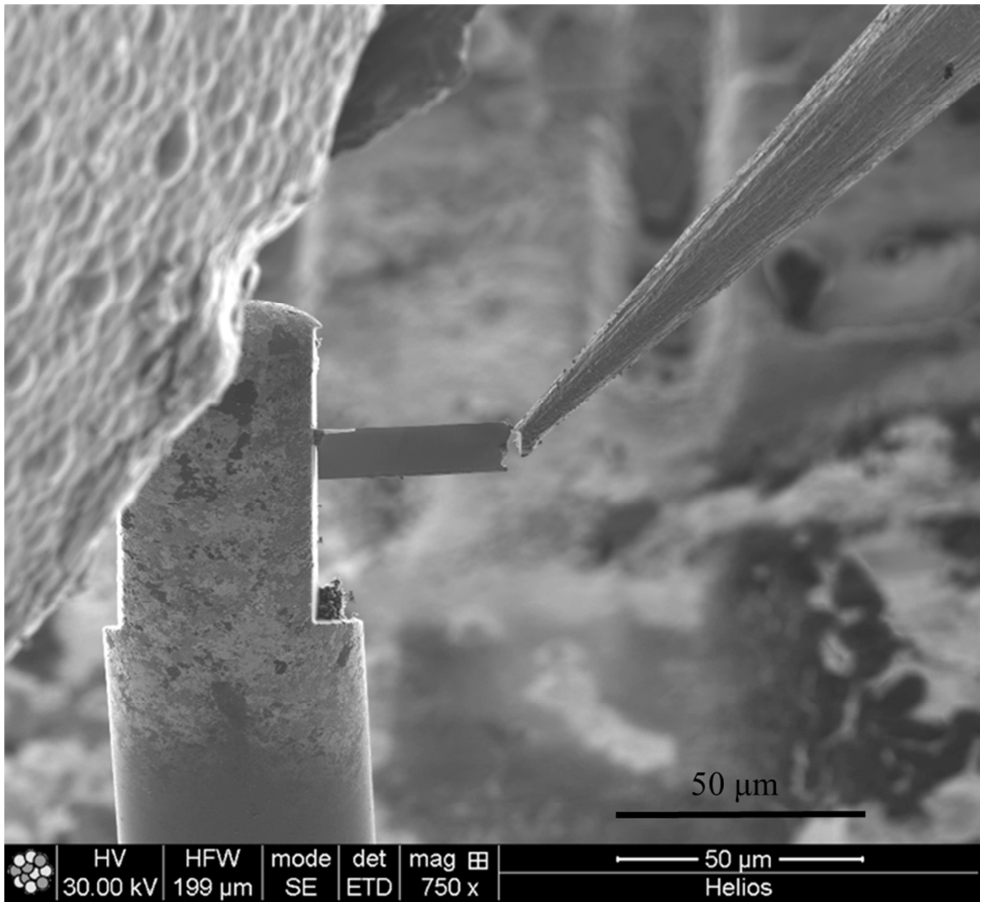

Figure 3-12: Attached FIB specimen on copper grit/ finger.

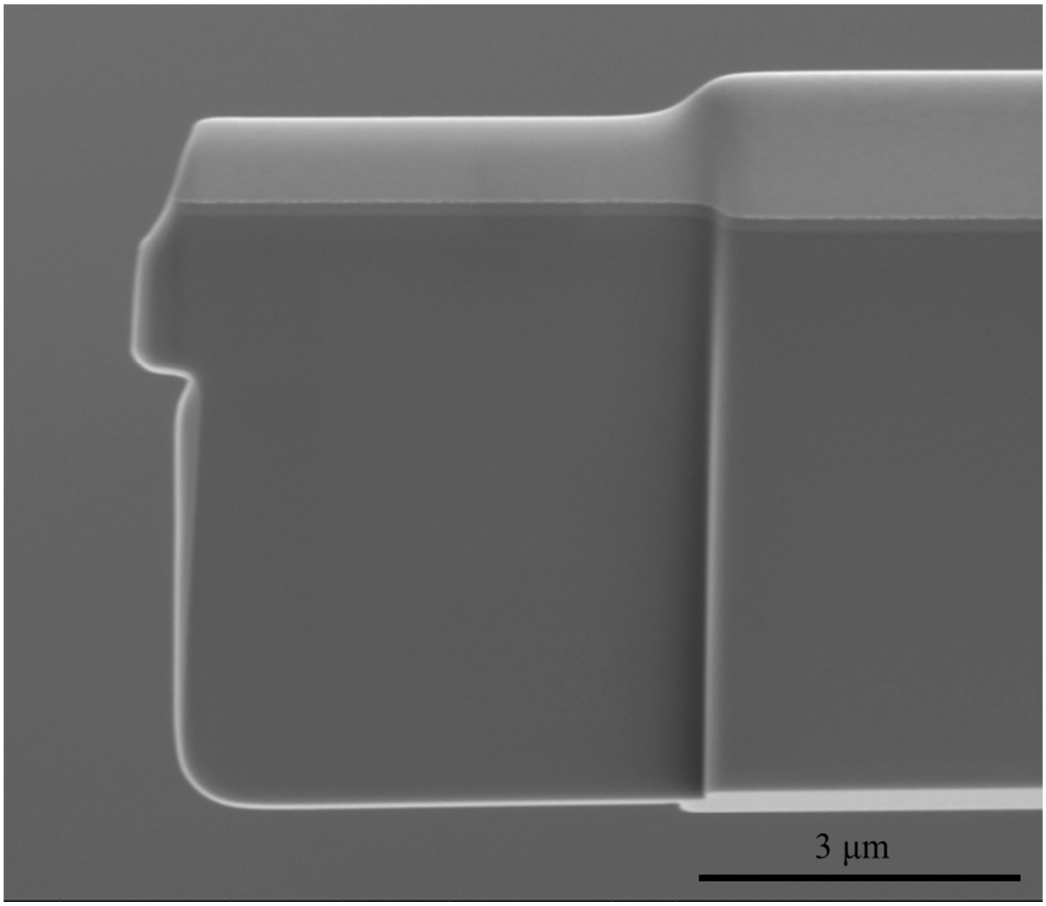

Figure 3-13: FIB thinned area of a site specific prepared sample.

3.10. References

[1] H. Boeckels, Diplomarbeit:"Dissolution and Coarsening of A Phase in Ti-15Mo-X O Alloys", TU Clausthal, 2008

[2] T. J. Devine, MS Thesis: "Comparison of Full-Profile Peak Finding Methods for use in X-ray Residual Stress Analysis", Northwestern University, 1985

[3] A.F. Giamei and E.J. Freise, Trans. AIME, 1967, Vol. 239, pp. 1676-85

[4] B. D. Cullity: "Elements of X-Ray Diffraction", Addison-Wesley, 1978

[5] B. E. Warren: "X-RAY DIFFRACTION", Dover, 1990, Chapter 13, pp. 251-314

[6] R. Jacobson, (1998). *REQAB* Version 1.1. Molecular Structure Corporation, The Woodlands, Texas, USA. Molecular Structure Corporation & Rigaku (2006). *CrystalClear* MSC, The Woodlands, Texas, USA, and Rigaku Corporation, Tokyo, Japan.

[7] G. M. Sheldrick, (2008). *SHELXTL* Version 6.10 Acta Cryst. A64, 112-122. Mercury CSD 2.0 - New Features for the Visualization and Investigation of Crystal Structures

[8] K. Brandenburg, (1999). DIAMOND, Crystal Impact GbR, Bonn, Germany

[9] L.A. Giannuzzi et al., "Applications of the FIB Lift-Out Technique for TEM Specimen Preparation", Microscopy Research and Technique, Vol. 41, 1998, p. 285-290

[10] L.A. Giannuzzi and F. A. Stevie, "A Review of focused ioan beam milling techniques for TEM specimen preparation", Micron, Vol. 30, 1999, p. 197-204

[11] unpublished research and private communication with Dr. R. E. A. Williams, The Ohio State University

[12] L.A. Gianuzzi, ”Introduction to Focused Ion Beams: Instrumentation, Theory, Technique and Practice”, Springer, 2005, p. 201-228

CHAPTER FOUR

4. RESULTS

4.1. α + β Processed Ti-15Mo-(0.15-0.5)O

4.1.1 Hardness

The hardness results are summarized in Table 4-1. Ti-15Mo-0.15O exhibited a hardness of 26.6 Hardness Rockwell C (HRC) in the α + β solution treated condition. With increasing oxygen content, the solution treated hardness increased to 33 HRC for both Ti-15Mo-0.35O and Ti-15Mo-0.5O. After 400˚C aging temperature, the hardness for Ti-15Mo-0.15O increased to approximately 47 HRC after 0.75 h, Figure 4-1, this plateau being maintained to 128 h aging. Overaging was observed at longer aging times. Increasing the aging temperature to 450°C had little influence on the maximum hardness attainable at this temperature relative to that achieved at 400°C. However the plateau hardness interval time was decreased to between 0.25 h and 8 h, overaging being observed at longer aging times. Indeed aging Ti-15Mo-0.15O at 500°C, resulted in a slight decrease in peak hardness to 44 HRC, this level being maintained for a short period of time between 0.25 and 0.5 h, hardness decreasing sharply at longer aging times, Figure 4-1 c. Finally at the highest aging temperature examined, 550°C, the hardness observed in Ti-15Mo-0.15O exhibited a hardness plateau of 34 HRC, from 0.25 to 8 h after which overaging and a hardness decreased to 28.8 HRC was observed, Figure 4-1 d.

A rapid increase in hardness at short aging times, 0.75 h, to 47 HRC was observed for Ti-15Mo-0.35O aged at 400°C, Figure 4-2 a. This was followed by a further gradual increase to 49.1 HRC after aging for 4 h, this level being maintained until 256 h when overaging commenced. An increase in aging temperature to 450°C, Figure 4-2 b, resulted in a slight decrease in the maximum harness achievable in Ti-15Mo-0.35O and a decrease in the aging time required to achieve this hardness level. Overaging was again observed after aging for times beyond 16 h. Further increases in aging temperature to 500 and 550°C resulted in the appearance of a maximum hardness at early aging times, 0.25 h, continued exposure resulting in a continuous decrease in hardness with increasing aging times.

A similar hardness response was observed in Ti-15Mo-0.5O when compared to Ti-15Mo-0.35O, Figure 4-3, a rapid increase in hardness after aging at 400 and 450°C being followed by a more gradual increase to a plateau level. Overaging was not however observed at 400°C, while that observed at 450°C was more gradual than in Ti-15Mo-0.35O. Continuous overaging was also observed after aging at 500 and 550°C, the rate of decrease in hardness being lower in Ti-15Mo-0.5O when compared to Ti-15Mo-0.35O.

The hardness response depending on oxygen content was visualized combining the isothermal hardness response for all oxygen contents at a fixed temperature into a single representation, Figure 4-4. The hardness response of Ti-15Mo-0.35O and Ti-15Mo-0.5O was almost identical over the investigated temperature range. Ti-15Mo-

Table 4-1: Influence of aging time and temperature on the hardness of Ti-15Mo-(0.15-0.5)O

Ti-15Mo-0.15O

Temperature	Time (hrs)													
	ST	0.03	0.25	0.5	0.75	1.75	3.75	7.75	16	32	64	128	256	512
400˚C	26.6	41.6	44.5	46.9	45.3	46.3	47.3	47	47.3	48.1	47.2	47	45	44.3
450˚C	26.6	-	46.6	45.6	45.9	46.3	45.6	45.6	44.2	43.4	41.5	41.2	37.2	34.5
500˚C	26.6	-	42.4	43.4	40.6	39.8	38.8	36.7	35.8	34.6	33.8	31.6	31.4	30.5
550˚C	26.6	-	33.4	34.3	33.4	33.5	33.8	34.7	30.9	30.1	28.8	-	-	-

Ti-15Mo-0.35O

Temperature	Time (hrs)													
	ST	0.03	0.25	0.5	0.75	1.75	3.75	7.75	16	32	64	128	256	512
400˚C	33.2	42.7	45.2	46.2	47.1	47.8	48.8	48.9	48.6	48.6	49.8	49.2	45.2	47.8
450˚C	33.2	-	47.8	48.1	46.9	48	48	47.8	47.9	46.8	45.6	43.5	40.9	40.5
500˚C	33.2	-	45.5	44.4	44	42.8	42	39	39.7	40.8	39.4	38.7	38.3	37
550˚C	33.2	-	39.4	39.8	38.9	38.8	38.5	38.1	36.9	36.9	36.3	-	-	-

Ti-15Mo-0.5O

Temperature	Time (hrs)													
	ST	0.03	0.25	0.5	0.75	1.75	3.75	7.75	16	32	64	128	256	512
400˚C	32.8	41.9	46.3	47	46.1	47.8	47.9	48.6	49.2	49.4	49.3	49.4	48.3	48.8
450˚C	32.8	-	47.9	48	46.9	47.2	47	47.2	47.4	46.5	45.9	45.6	43.1	43.1
500˚C	32.8	-	44.6	44.4	42.3	42.5	41.2	41.8	41	41.6	41	41.7	40.5	39.6
550˚C	32.8	-	39.4	39.9	37.8	38.5	39	39	38.3	38.5	36.2	-	-	-

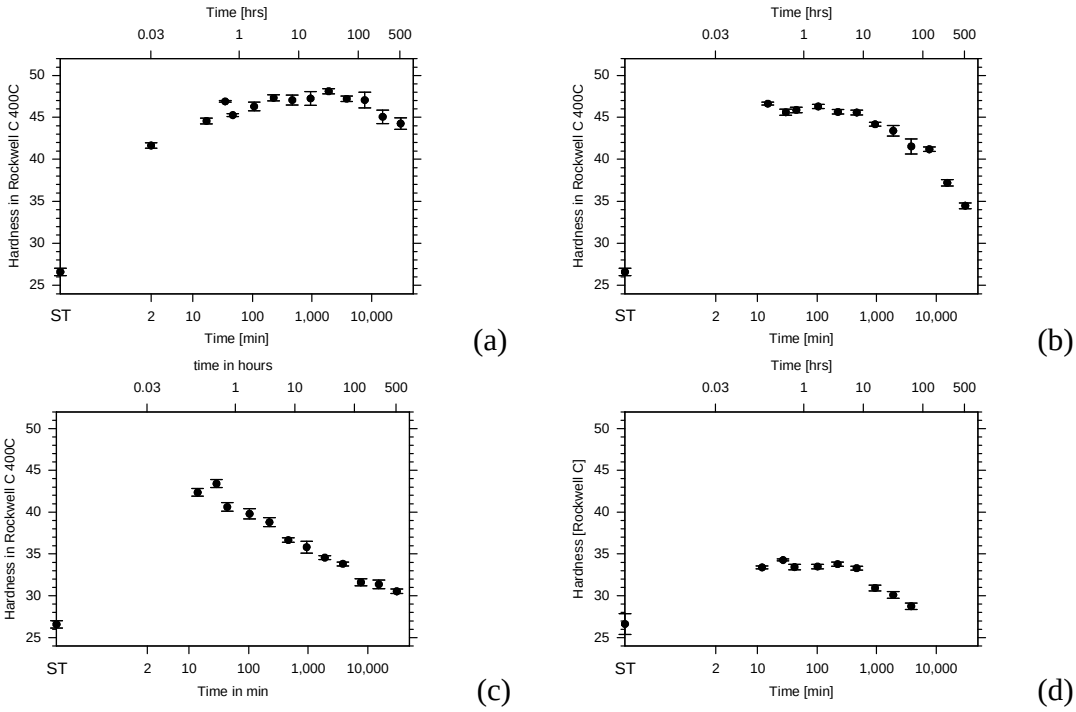

Figure 4-1: Influence of aging time and temperature on hardness on aged Ti-15Mo-0.15O: (a) at 400˚C aging temperature; (b) at 450˚C aging temperature; (c) at 500˚C aging temperature; (d) at 550˚C aging temperature; ST is the solution treated condition.

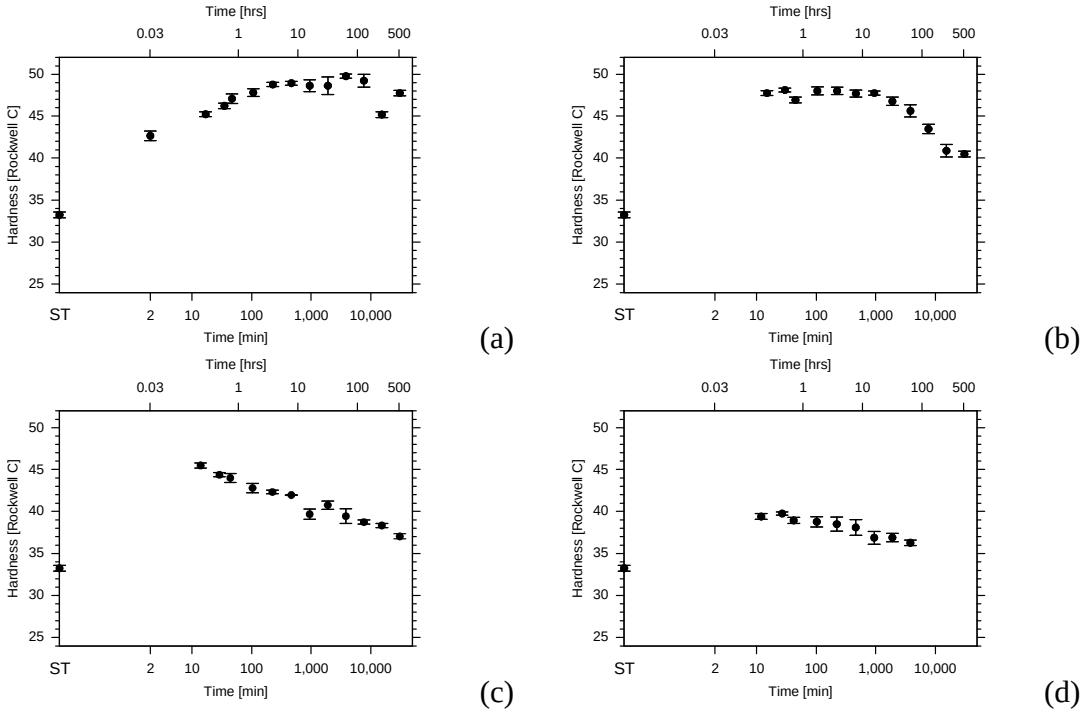

Figure 4-2: Influence of aging time and temperature on hardness on aged Ti-15Mo-0.35O: (a) at 400˚C aging temperature; (b) at 450˚C aging temperature; (c) at 500˚C aging temperature; (d) at 550˚C aging temperature; ST is the solution treated condition.

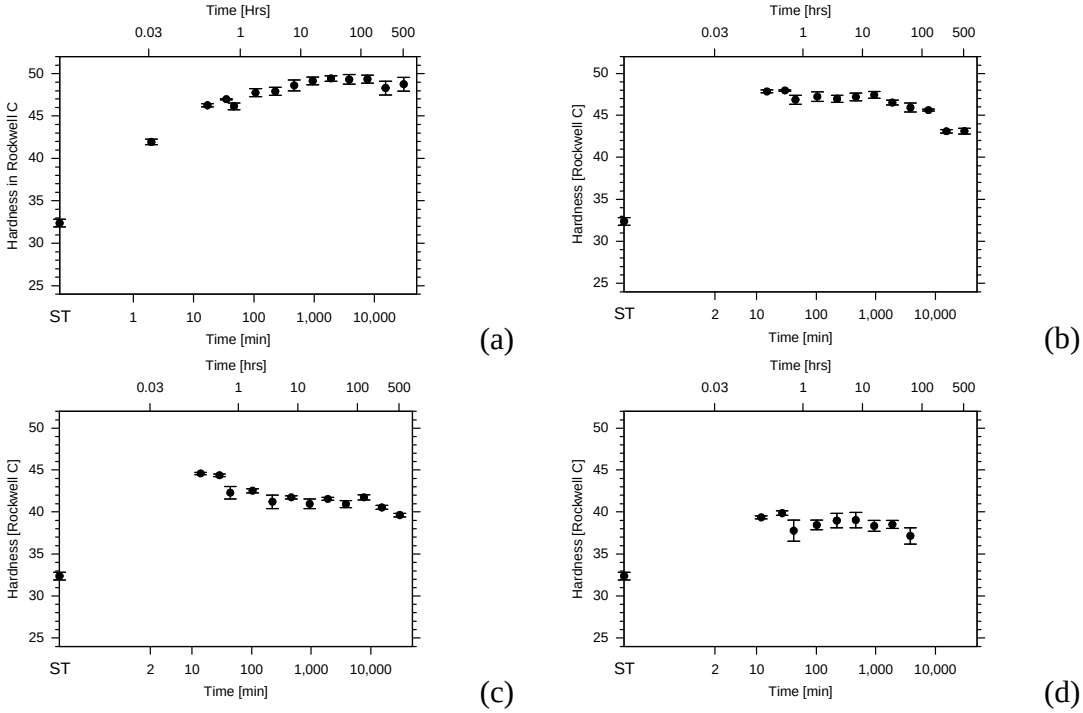

Figure 4-3: Influence of aging time and temperature on hardness on aged Ti-15Mo-0.5O: (a) at 400˚C aging temperature; (b) at 450˚C aging temperature; (c) at 500˚C aging temperature; (d) at 550˚C aging temperature; ST is the solution treated condition.

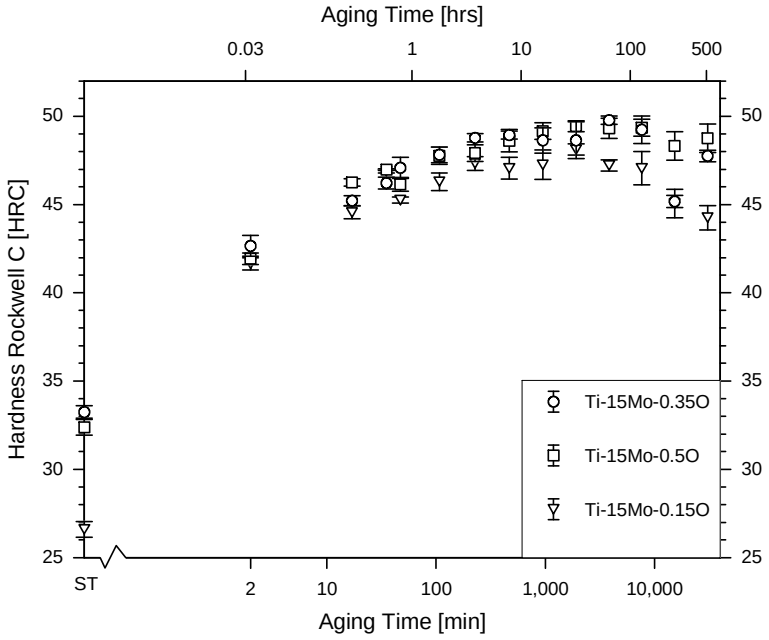

(a)

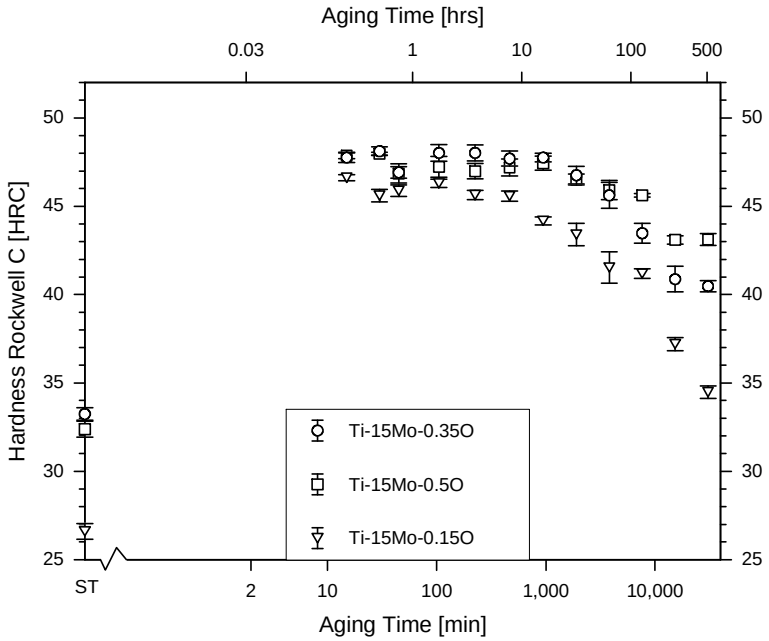

(b)

Figure 4-4: Isothermal plots of the dependence of hardness upon time and oxygen content for Ti-15Mo-0.15O,Ti-15Mo-0.35O and Ti-15Mo-0.5O at 400°C (a), 450°C (b), 500°C (c) and 550°C (d).

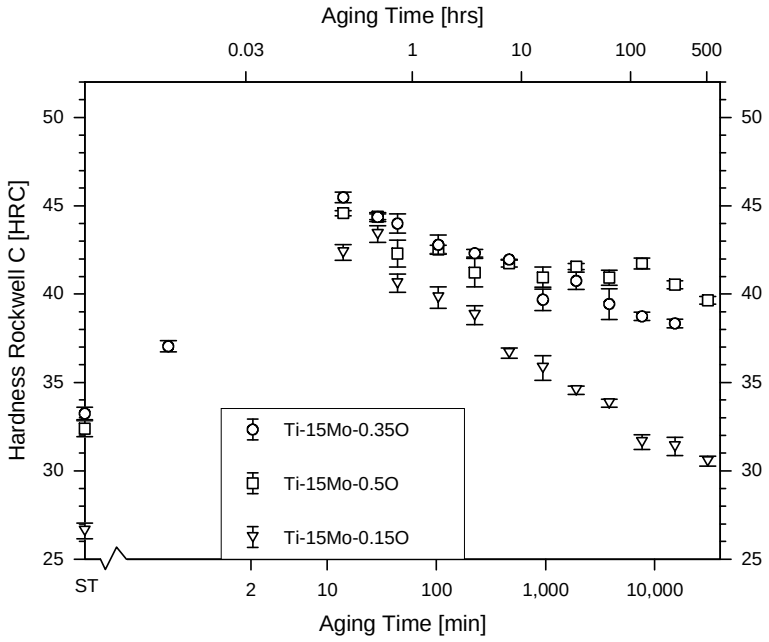

(c)

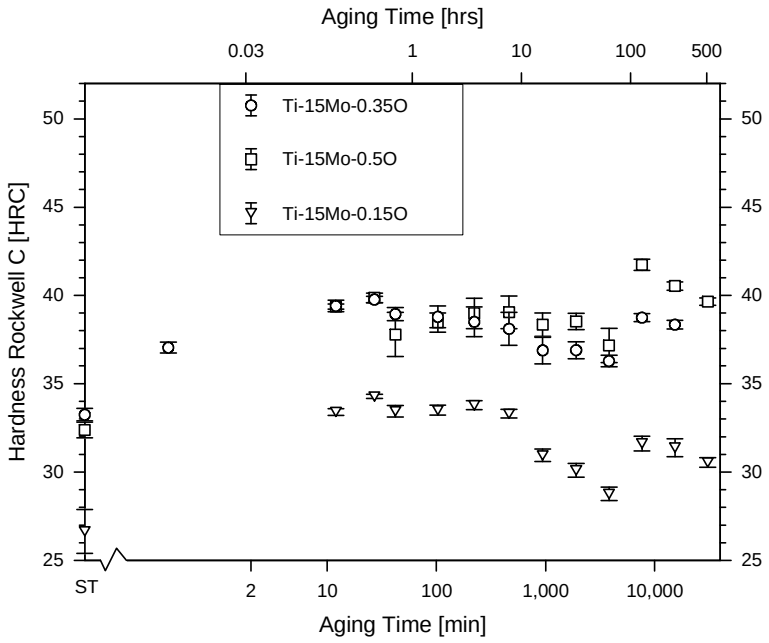

(d)

Figure 4-4: continued

0.15O exhibited a lower overall hardness, when compared to the higher oxygen containing alloys and faster aging kinetics which resulted in earlier overaging. The difference in overaging response between the low oxygen alloy and both higher oxygen containing alloys were more pronounced with increasing aging temperature.

4.1.2 X-Ray Diffraction (XRD)

Figure 4-5 illustrates a typical x-ray diffraction pattern for the 2Θ range between 35 and 90˚ 2Θ for Ti-15Mo-0.15O, the two peaks used for the ω size measurements being defined with Table 4-2 listing the complete spectrum analysis.

4.1.3 ω Size

Aging Ti-15Mo-0.15O at 400°C initially increased (2-11)/(301) ω size 5.8/8.6 nm to 13/15 nm following which no further ω size increase was observed until 16/64 h aging times were exceeded when the ω size again increased. Finally, at the longest aging times examined, no (2-11) ω peaks were observed, Figure 4-6 a and d. A similar behavior was observed after aging at 450°C, (2-11)/ (301) ω sizes stabilizing at approximately 17.5/22.5 nm. The ω size increased from below the detectable limit to 15 nm after 0.75 hours at 450°C or 22.5 nm after 4 hours for the (301) ω respectively, Figure 4-6 b and e. These remained constant at approximately 15 nm/ 22.5 nm until 32 hours. At 64 hours, a maximum of 35 nm was observed for the (2-11) ω peak followed by a steady decline to 15 nm at 512 hours, Figure 4-6 b. No peak was visible for the (301) ω peak, a decline was also observed after 32 hours, Figure 4-6 e. The average ω size increased at 500°C up to 28 nm to 8 hours, after when the size declined below the

detectable minimum, Figure 4-6 c. The (301) ω peak exhibited a similar increase up to 34.5 nm and 16 hours followed by a decline in size below the detectable minimum at 32 hours, Figure 4-6 f.

For Ti-15Mo-0.35O, the ω size increased continuously from below the detection minimum to 34/35 nm at 512 hours at 400°C for both ω peaks, Figure 4-7 a and d. This increase was gradually rising from below the detection minimum to 14 nm after 8 hours and 17/19 nm at 256 hours. A further increase to 34/35 nm after 512 hours aging was much more pronounced than that observed during the early aging times. At 450°C, the ω size evolution exhibit a maximum of 35 nm after 16 hours for the (2-11) ω peak, the initial value detected being 8.6 nm after 0.25 hours decreasing after the aforementioned maximum to 20.3 nm after 512 hours, Figure 4-7 b. In contrast, the (301) ω size exhibited a constant value at, approximately 19 nm up to 128 hours, increasing after 256 hours to 35 nm. Finally at the highest temperature investigated, 500°C, and an initial maximum value 18.3 / 23 nm after 0.25 hours was observed, after which the (2-11) ω size decreased until it could no longer be detected after 3.75 hours, Figure 4-7 c. In contrast, the (301) ω size measured maintained a constant size until 8 hours, thereafter decreasing below the detectable minimum, Figure 4-7 f.

The (2-11) ω size was constant at 9 nm between 0.03 and 0.75 hours during initially aging of Ti-15Mo-0.5O at 400°C, the size then increasing to 15 nm at 1.75 hours where it remained until 64 hours, after which it increased further to 28 nm at 128 hours before decreasing below the detection minimum at 512 hours, Figure 4-8 a.

Table 4-2: X-ray spectrum analysis of Ti-15Mo-xO at room temperature, 2θ is the observed value, $2\theta_{th}$ is the computed value.

$2\theta_{obs.}$	$2\theta_{th}$	Phase (hkl)
35.3	35.64	α (100)
38.48	38.55	α (002)
	39.13*	ω (101)
39.2	39.98	β (110)
40.3	40.69	α (101)
51.14	51.25	ω (2-11)
53.1	53.51	α (102)
56.13	56.31	β (200)
56.6	56.55	ω (201)
63.1	64.01	α (2-10)
70.5	70.60	β (211)
70.75	70.91	ω (3-11)
70.97	71.20	α (103)
76.29	76.21	α (200)
77.47	77.28	α (2-12)
79.6	79.49	ω (301)
83.7	83.72	β (220)
83.9	84.13	ω (202)

*peak beneath the (110) β peak

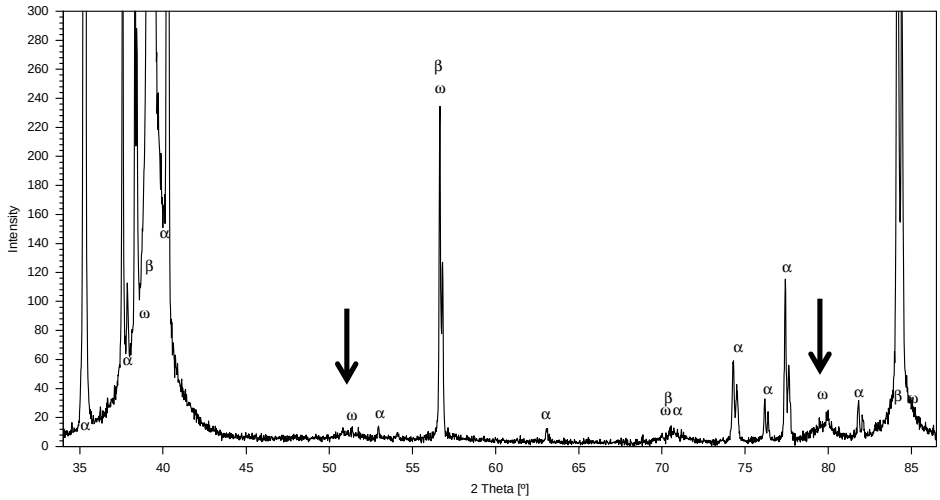

Figure 4-5: Diffraction pattern trace for Ti-15Mo-0.15O aged for 15 minutes at 400˚C from 34 to 90˚ 2Θ, using Cu radiation.

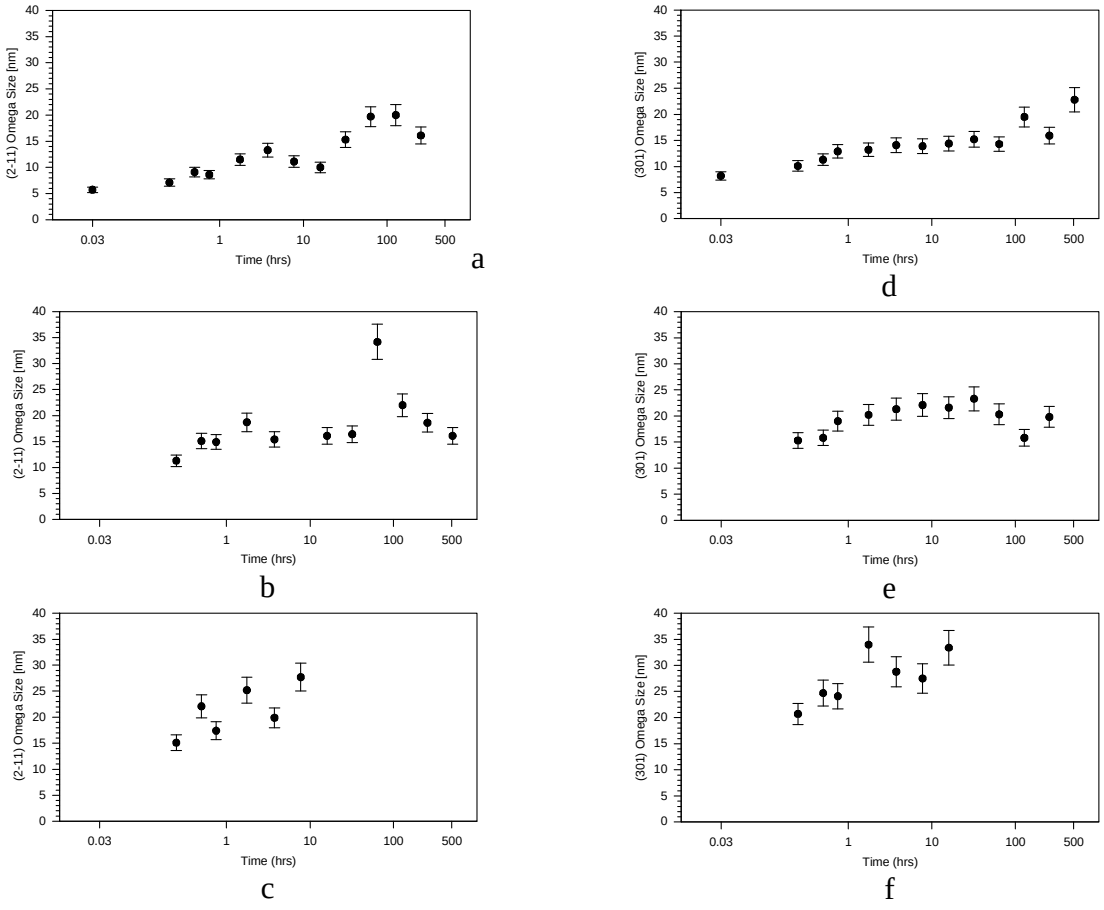

Figure 4-6: Average ω size for Ti-15Mo-0.15O plotted versus aging time at 400°C (a), 450°C (b) and 500°C (c) for (2-11) and at 400°C (d), 450°C (e) and 500°C (f) for (301).

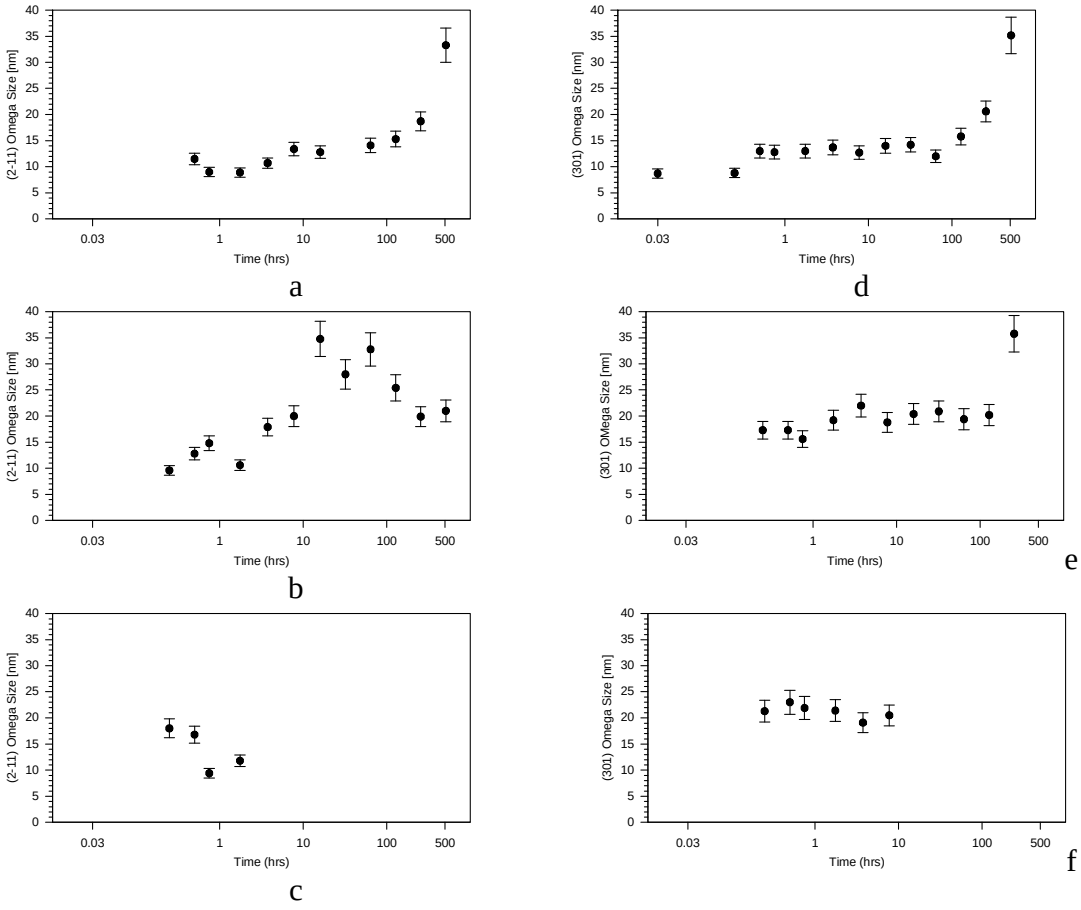

Figure 4-7: Average ω size for Ti-15Mo-0.35O plotted versus aging time at 400°C (a), 450°C (b) and 500°C (c) for (2-11) and at 400°C (d), 450°C (e) and 500°C (f) for (301).

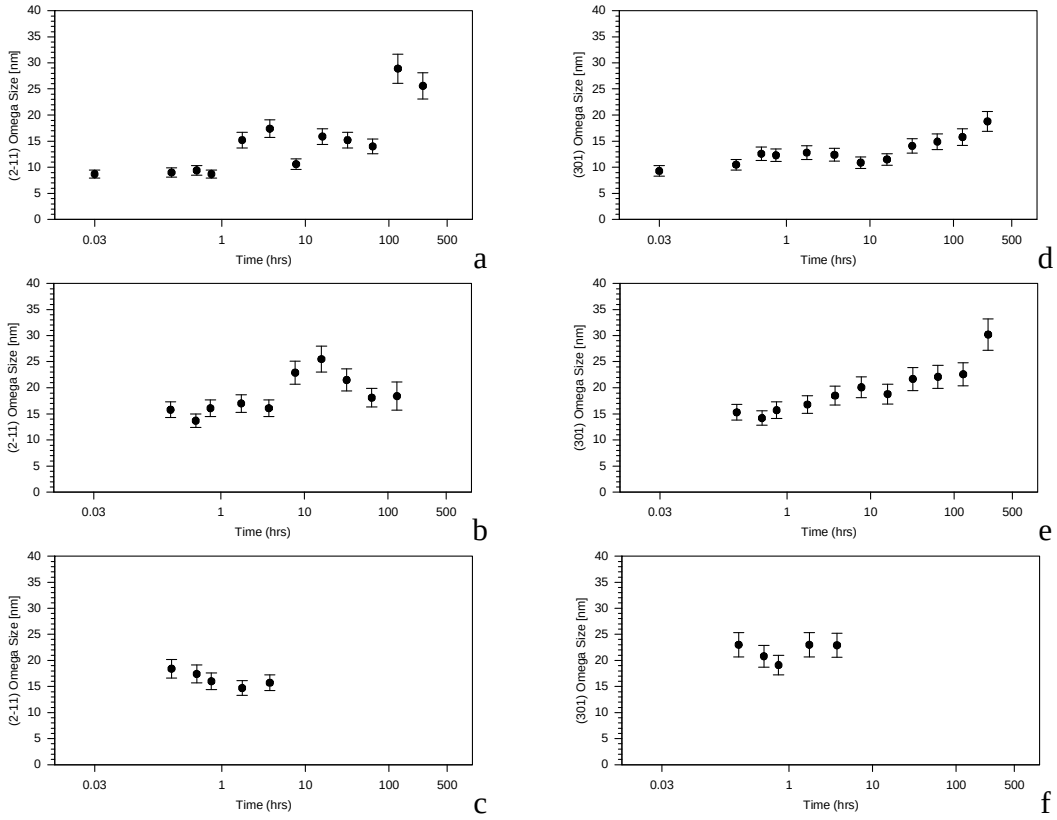

Figure 4-8: Average ω size for Ti-15Mo-0.5O plotted versus aging time at 400°C (a), 450°C (b) and 500°C (c) for (2-11) and at 400°C (d), 450°C (e) and 500°C (f) for (301).

Similarly, the (301) ω size was 9 nm at 0.03 hours, increasing slightly to 13.5 nm at 16 hours before increasing to a maximum at 256 hours, Figure 4-8 d. The (2-11) ω size following aging at 450°C initially increased slightly when compared with the 400˚C 15 nm between 0.25 and 3.75 hours where upon it increased to a maximum of 25 nm at 16 hours before the size decreasing below the detection minimum after 256 hours, Figure 4-8 b. A plateau at 15 nm for up to 0.75 hours was also visible for the (301) ω peak of Ti-15Mo-0.5O aged at 450˚C, further aging resulting in ω size increasing to a maximum of 33 nm at 256 hours, Figure 4-8 e. Finally, a similar ω size plateau between 0.25 and 7.75 hours was observed after aging at 500°C between 18/20 nm and 16.5/25 nm before the ω size declined below the detection minimum again at 16 hours, Figure 4-8 c and f.

4.1.4 Calorimetry

Figure 4-9 summarizing the isochronal DSC observations within the temperature range between 400 and 550°C, the heat flow (J) being plotted versus aging time and temperature. The solid lines are the uncorrected isochronal DSC results, the dashed line below being the DSC baseline, as determined from Ti-15Mo-(0.15-0.5)O samples aged for 512 hours at 550°C. All the observed results overlapped and followed the same trends, this observation confirming the uniformity and reproducibility of the aging results. At the highest isochronal temperature, a simple peak was observed. This peak being at lower temperatures partially resolved, e.g. at 400˚C, no peak, only an increase

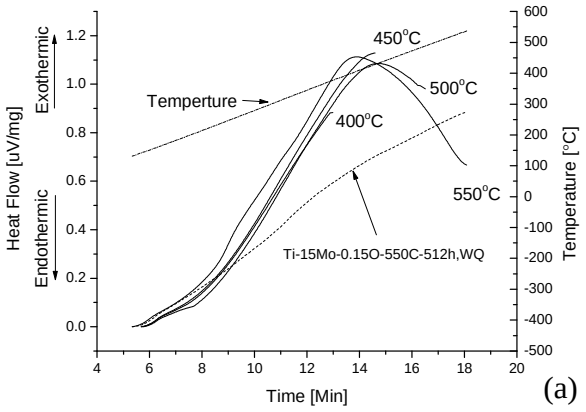

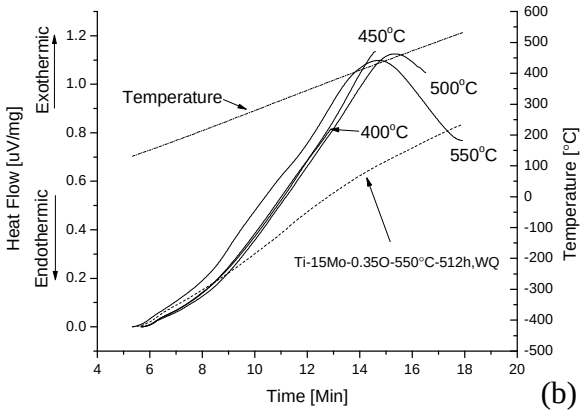

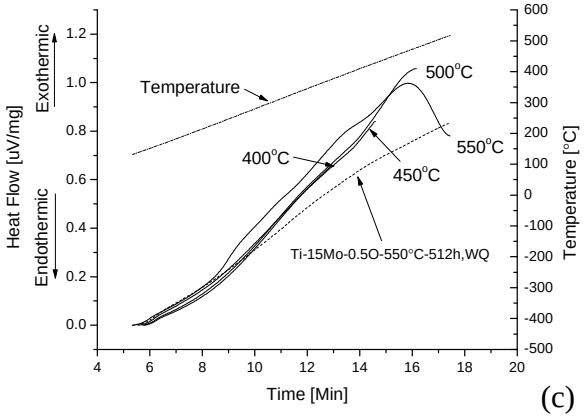

Figure 4-9: Compilation of isochronal DSC results for α + β processed Ti-15Mo-(0.15-0.5)O at a heating rate of 30 CPM for temperatures in the range of 400 to 550°C.

in heat flow, could be observed, Figure 4-9. Increasing oxygen content resulted in an increase in the maximum peak temperature from 430˚C for Ti-15Mo-0.15O, increasing to 445˚C for Ti-15Mo-0.35O and reaching 469˚C for Ti-15Mo-0.5O, Figure 4-9 a-c. This shift in temperature was accompanied by a decline in peak intensity.

Further analysis of the baseline corrected isochronal thermal analysis observations during continuous heating of α+β- processed Ti-15Mo-(0.15-0.5)O are shown in Figures 4-10 – 4-12.

Three reactions were observed for To-15Mo-0.15O and Ti-15MO-0.35O while Ti-15Mo-0.5O displayed 4 reactions, each being defined by a local maximum in J. The first derivative of the heat flow J, J', exhibited, that each reaction peak observed in J was based on multiple reactions, based on multiple local minima in J'. J' also showed that the observed reactions were overlapping with each other. Table 4-5 summarizes the observed reaction temperatures. Increasing oxygen content lead to a decrease in the observed reaction temperature, R4 was only being observed at the highest oxygen content examined. For example, the initial reaction R1 being observed in all three alloys at approximately 150°C. The same observation can be made for the second reaction, R2, at approximately 309°C as well as for R3 at approximately 400°C. The fourth reaction observed, R4, is only present in Ti-15Mo-0.5O at 460°C.

The isothermal analysis results are presented in Figures 4-13 through 4-15, the heat flow during isothermal aging being plotted versus time. The isothermal results

could be divided into three temperature regions for Ti-15Mo-0.15O, a low temperature regime ≤400°C, an intermediate temperature regime ≤500°C and a high temperature regime >500°C. Two peaks, P1 and P2, were observed at 400˚C, Figure 4-13 a, the transformation causing P2 was not finished during the investigated time frame. At intermediate temperatures, three separate peaks were observed, while at the highest temperature only one peak was recorded. Increasing Oxygen content, Ti-15Mo-0.35O, resulted in appearance of two peaks ≤ 450˚C, Figure 4-14 a and b. Three peaks were observed at 500˚C while only one peak was observed at 550°C, Figure 4-14 c and d. Finally, isothermal analysis of Ti-15Mo-0.5O exhibited two peaks ≤ 500˚C, with only one isothermal peak being found during exposure at 550˚C, Figure 4-15 a-d.

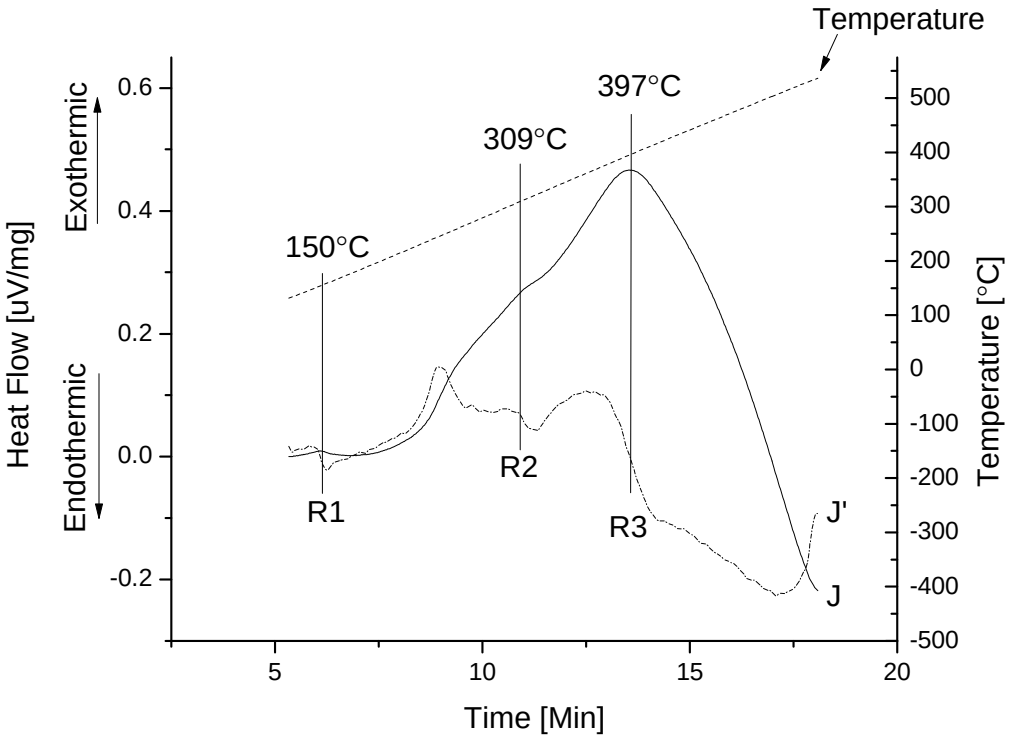

Figure 4-10: Baseline corrected isochronal DSC results α + β solution heat treated Ti-15Mo-0.15O.

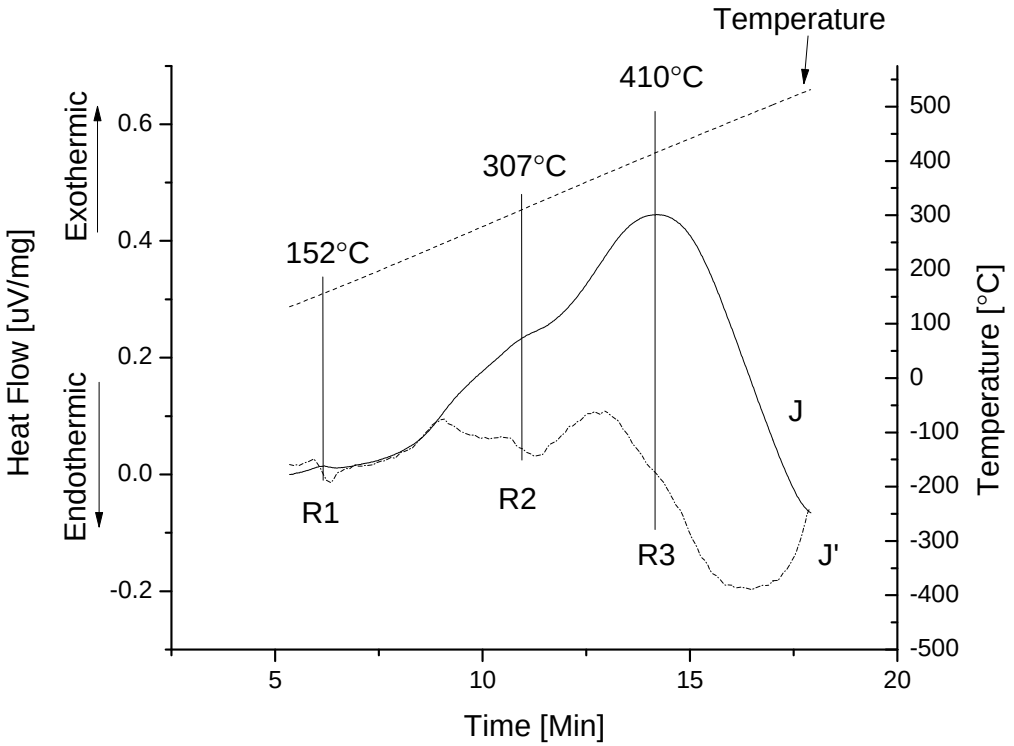

Figure 4-11: Baseline corrected isochronal DSC results α + β solution heat treated Ti-15Mo-0.35O

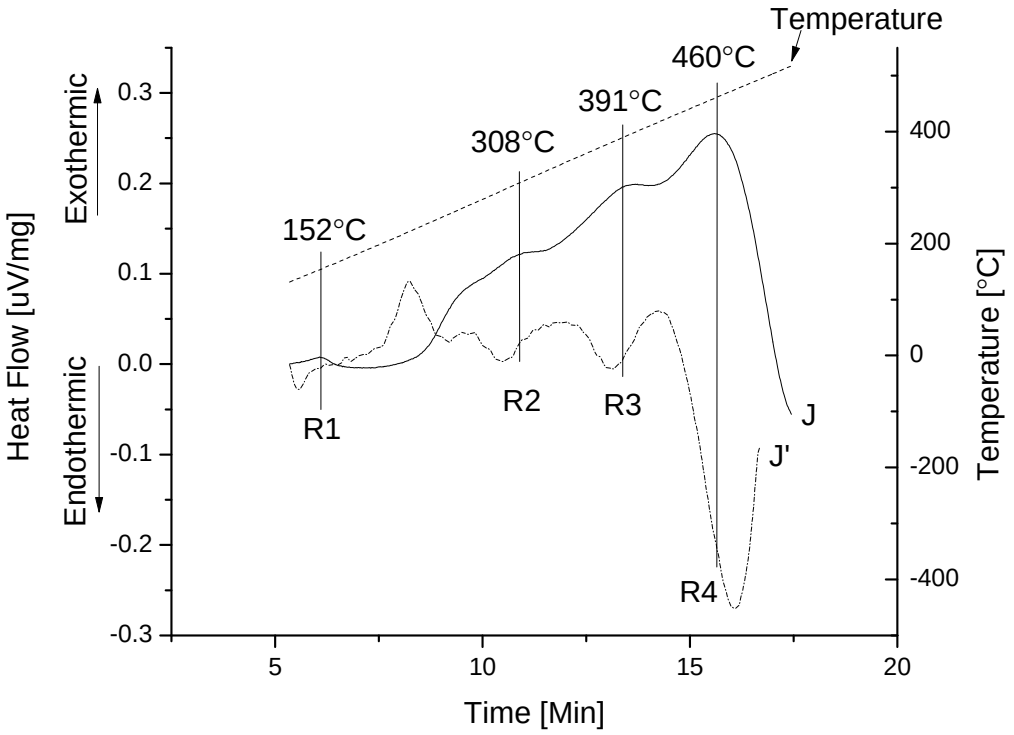

Figure 4-12: Baseline corrected isochronal DSC results α + β solution heat treated Ti-15Mo-0.5O.

Table 4-3: Peak temperature for the occurring phase transformations during the 30°C per minute heat up of α+β processed Ti-15Mo-(0.15-0.5)O alloys to 550°C

Ti-15Mo-0.15O: Observed Reactions	Observed Peak Temperature
R1	150˚C
R2	309˚C
R3	397˚C
Ti-15Mo-0.35O: Observed Reactions	Observed Peak Temperature
R1	152˚C
R2	307˚C
R3	410˚C
Ti-15Mo-0.5O: Observed Reactions	Observed Peak Temperature
R1	152˚C
R2	308˚C
R3	391˚C
R4	460˚C

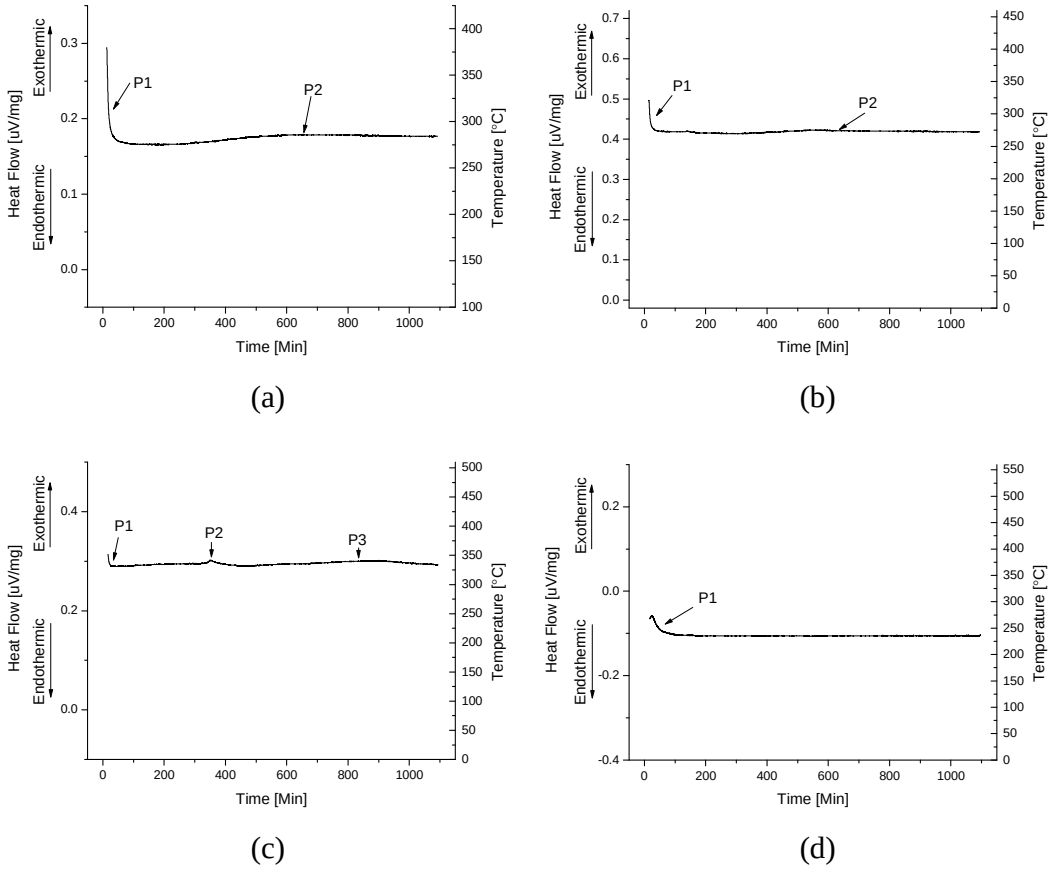

Figure 4-13: Thermal response of Ti-15Mo-0.15O aged at 400°C (a), 450°C (b), 500°C (c) and 550°C (d).

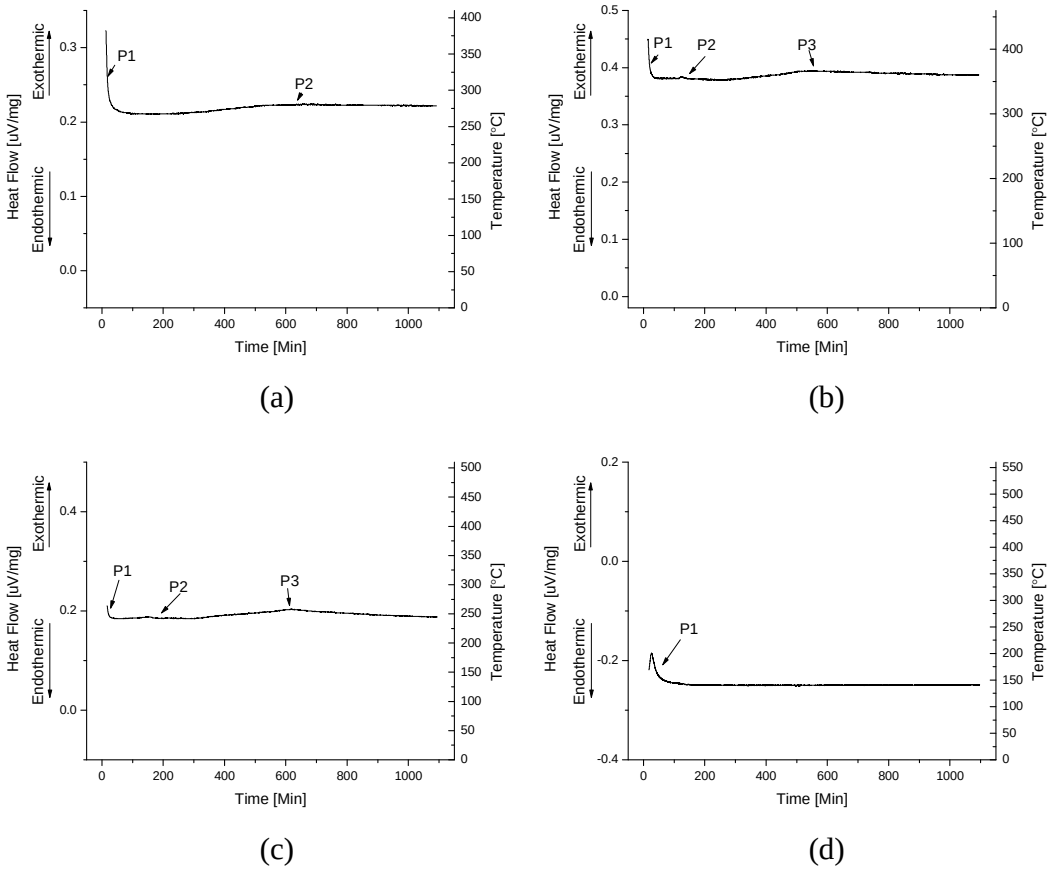

Figure 4-14: Thermal response of Ti-15Mo-0.15O aged at 400°C (a), 450°C (b), 500°C (c) and 550°C (d).

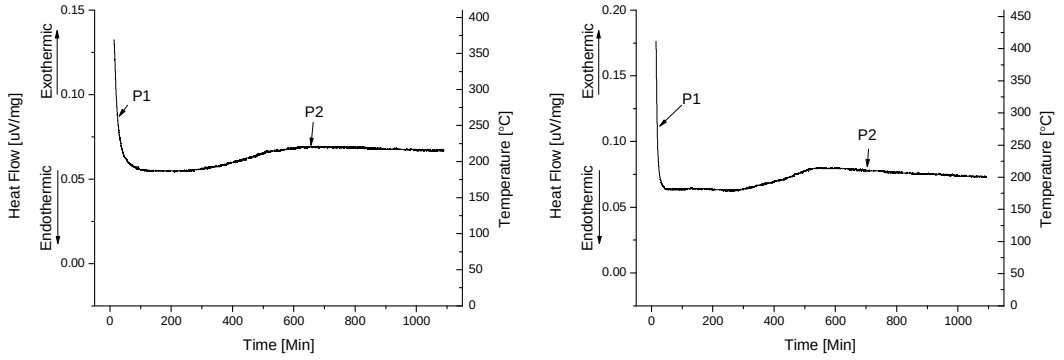

(a)

(b)

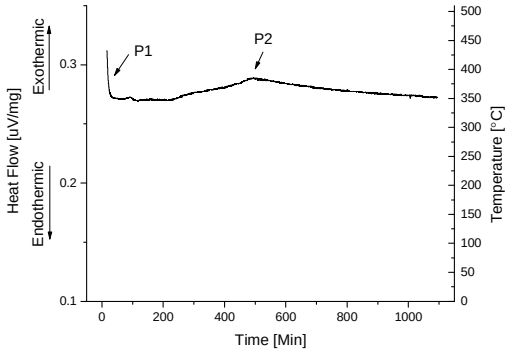

(a)

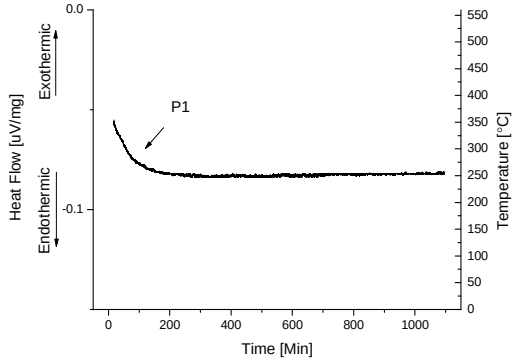

(b)

Figure 4-15: Thermal response of Ti-15Mo-0.5O aged at 400°C (a), 450°C (b), 500°C (c) and 550°C (d).

4.2. β Solution Heat Treated Ti-15Mo-(0.12-2)O

4.2.1 Calorimetry

The results of the thermal analysis during continuous heating of β- solution heat treated Ti-15Mo-(0.12-2)O are presented in Figures 4-16 through 4-31. Three different heating rates were applied for the isochronal experiments, 1°C per minute (1CPM), 5°C per minute (5CPM) and 50°C per minute (50CPM), the isochronal results including their baseline plotted for the respective heating rates being included. Further analysis of the baseline corrected isochronal heat flow curves, J, and their first derivative J' were used to define the transformation start, peak and finish temperature, for each reaction observed, then being summarized for each oxygen content, Tables 4-4 through 4-8.

Ti-15Mo-0.12O exhibited one peak during isochronal heat up at 5 CPM at approximately 350˚C with a extending shoulder at 420˚C in the uncorrected heat flow curve, Figure 4-16 a, only the peak formed at 420°C with a maximum at 420°C being observed at 50CPM, Figure 4-16 b. The corrected isochronal heat flow J exhibited two distinct peaks having maxima at approximately 210 and 341˚C, a third peak being visible as a shoulder at 411˚C, Table 4-4. At 50 CPM, the single peak observed had a maximum at approximately 443˚C, Figure 4-17 and 4-18, Table 4-4.

Ti-15Mo-0.15O exhibited also a single peak with a shoulder at higher temperatures in the uncorrected heat flow curves, Figure 4-19. At 5 CPM, the peak maximum temperature remains at approximately 350˚C and for the shoulder at 420˚C,

with increasing the heating rate to 50CPM, increased similarly the maximum peak temperature to 475˚C. Following background correction, three peaks were observed, Figure 4-20. The first at 200˚C was similar to that observed in Ti-15Mo-0.12O, Figure 4-20, Table 4-5. The second peak had a maximum at 364˚C and the third, still a shoulder to the second, becoming more pronounced with a maximum at 426˚C, Figure 4-20. Finally heating at 50CPM resulted in the development of a single having a maximum at 450˚C, Figure 4-21.

Ti-15Mo-0.35O and Ti-15Mo-0.5O follow the same trends as the lower oxygen alloys, Figures 4-22 and 4-25, with the maximum at 350˚C at 5CPM. They also exhibit a single peak at approximately 475˚C at 50 CPM, Figures 4-23 and 4-26 as well as Tables 4-6 and 4-7. The second shoulder peak observed at the lower 5CPM heating rate, appears to be more widely separated from the main peak for Ti-15Mo-0.35O, peak maxima at approximately 442˚C. For Ti-15Mo-0.5 shifts the latter again to lower temperatures and becomes a shoulder again. At 50CPM, both alloys exhibited a single peak having a maximum at 426˚C and 438˚C respectively, Figures 4-24 and 4-27.

The highest investigated oxygen content, 2 wt%, was examined using 3 heating rates, the lowest 1 CPM, being intended to allow better peak separation. For example at 1 CPM Ti-15Mo-2O exhibited 3 distinct peaks at 250˚C, 350˚C and 480˚C, one more than the other alloys, Figure 4-28 a. The same peaks at the same temperatures are visible at 5 CPM, Figure 4-28 b. In contrast only a single peak at 450˚C for Ti-15Mo-2O heated at 50 CPM was observed, Figure 4-28 c. This peak was smaller and had a

less pronounced shape when compared with the peaks at lower oxygen concentrations. Figures 4-29 - 4-31 represent the corrected isochronal results suggesting that four, four, and two peaks were observed for the various heating rates, i.e. Ti-15Mo-2O heated at 1 CPM exhibits four peaks at 214, 306, 413, and 471˚C, Figure 4-29, that heated at 5CPM, had also four peaks. But the observed main peaks were split into two peaks as shown in Figure 4-30: R1.1 at 85°C, R 1.2 at 168°C, R 2.1 at 226°C, R2.2 at 269°C, R3.1 at 315°C, R3.2 at 350°C and R4 at 460°C, Table 4-8. At 50 CPM were two peaks, one more that at the lower Oxygen alloys, at 465°C and 523°C observed, Figure 4-31.

Finally all the isochronal observations at 1 and 5 CPM are summarized in Figure 4-32, increasing oxygen content resulted in an increase in the maximum peak area and height. Furthermore, an additional peak for Ti-15Mo-20 was observed (marked with arrow). The isothermal calorimetry results were presented in Figure 4-33 – 4-38 for 1 and 5 CPM. All alloys exhibited a reaction peak at 550˚C isothermal aging within the first 30 minutes of aging time. With increasing oxygen content, the area and intensity of this peak first increased before it decreased for the highest oxygen concentration. All other isothermal aging temperatures exhibited a decreasing or flat isothermal response.

Similarly the isochronal runs at 50 CPM with increasing oxygen are summarized in Figure 4-39. The single peak observed during heating is shifted to higher temperature with increasing oxygen, above 450˚C for up to 0.5 wt% O. At 2 wt% O, the peak maximum decreased to 400˚C. The area and intensity of the peak also decreased for Ti-15Mo-2O when compared with the other alloys.

It is important to note at this junction of the thesis, that the results of the 50CPM are in need of further investigation due to the effect of system lag time of the used DSC associated with the sample weight as well as the furnace thermal load and will not be analyzed in the discussion.

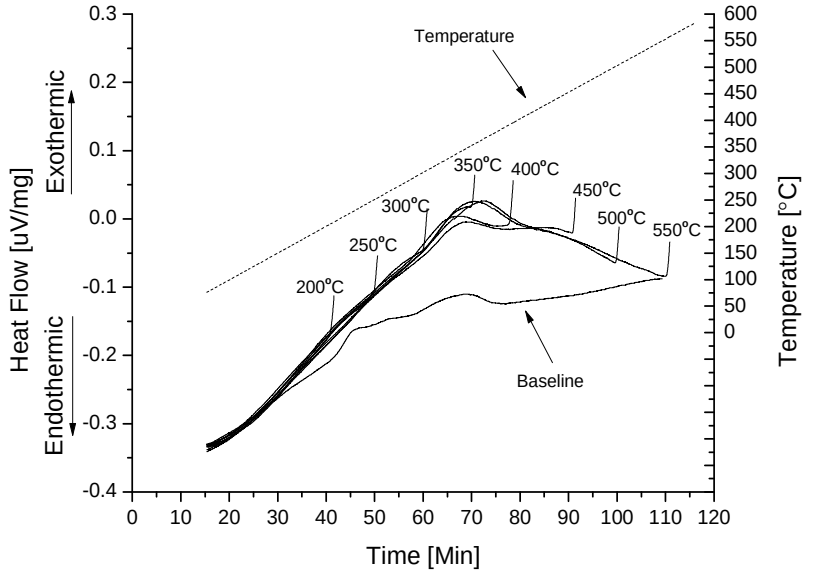

(a)

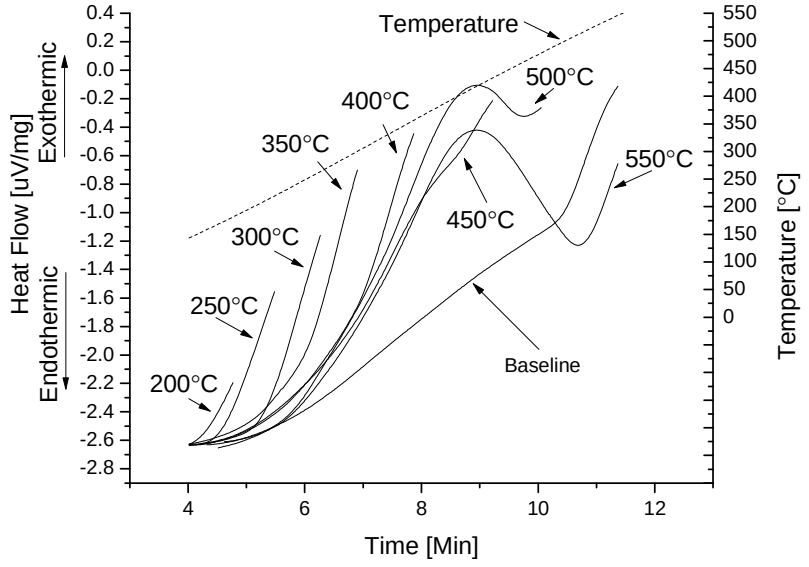

(b)

Figure 4-16: Uncorrected isochronal DSC results for β solution heat treated Ti-15Mo-0.12O at a heating rate of 5 and 50 CPM for temperatures in the range of 200 to 550°C.

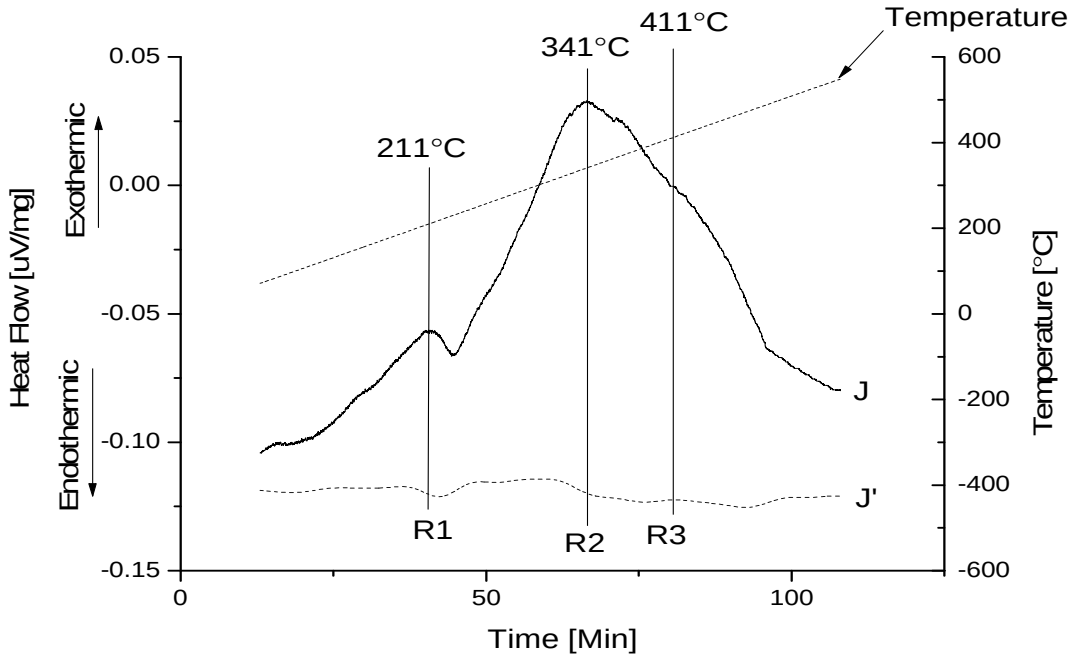

Figure 4-17: Corrected Heat Flow (J): dQ/dt vs time plot for solutionized Ti-15Mo-0.12O up to 550˚C with a scan rate of 5˚C per minute with baseline subtracted; dotted line below is the first derivative of J.

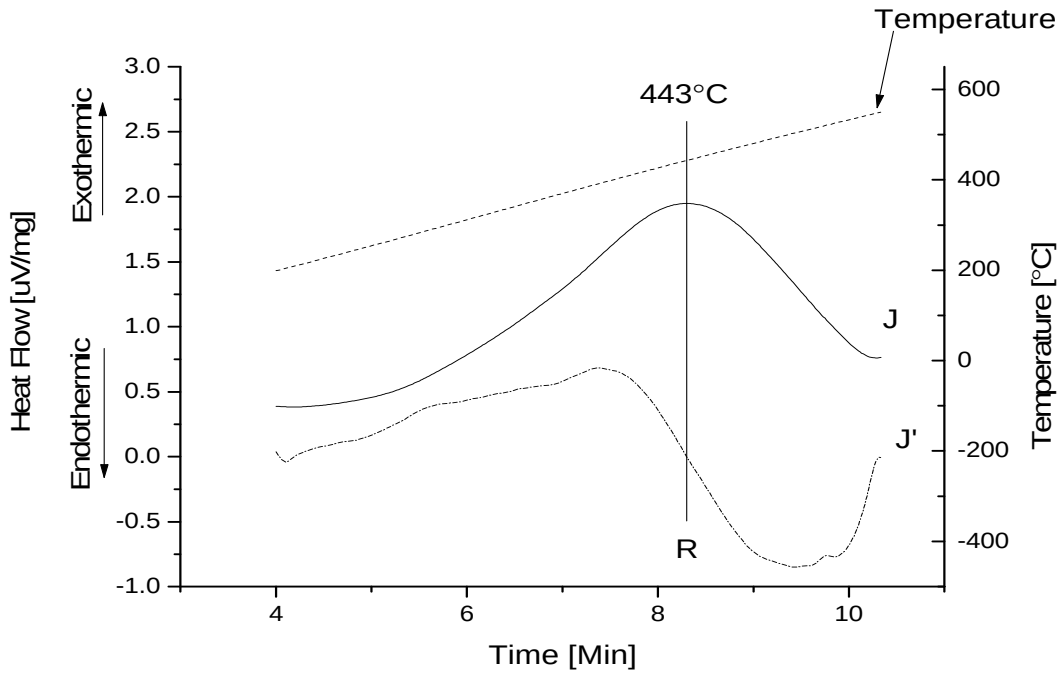

Figure 4-18: Corrected Heat Flow (J): dQ/dt vs time plot for solutionized Ti-15Mo-0.12O up to 550˚C with a scan rate of 50˚C per minute with baseline subtracted; dotted line below is the first derivative of J.

Table 4-4: Peak temperature for the occurring phase transformations during the 5 and 50°C per minute heat up of Ti-15Mo-0.12O alloy.

Reaction	T_{Peak}
5˚CPM	
R1	211°C
R2	341°C
R3	411°C
50°CPM	
R	443°C

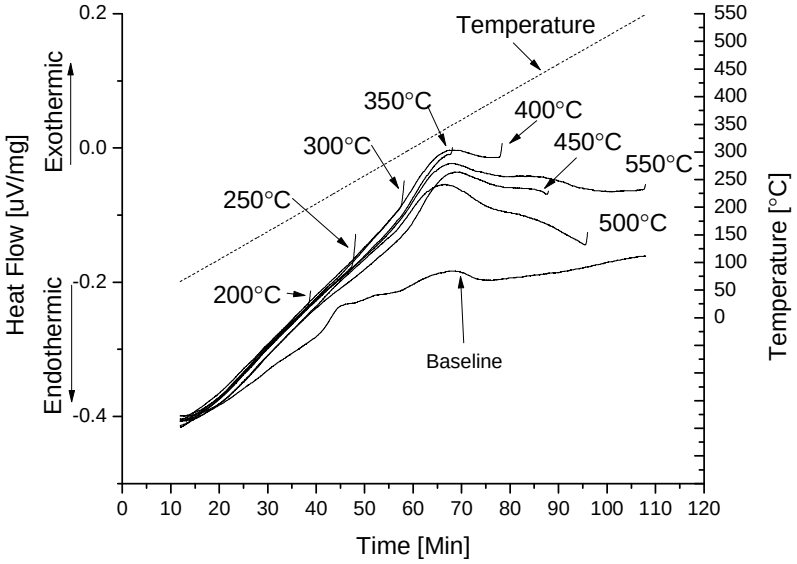

(a)

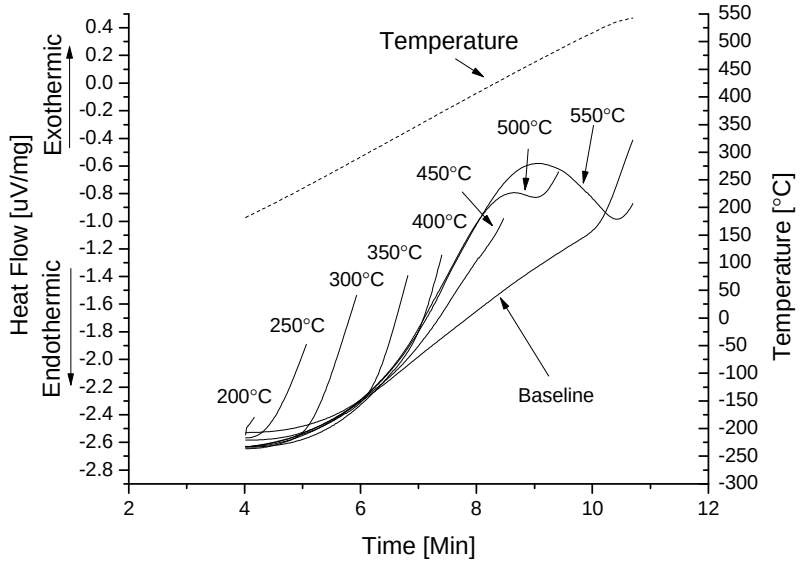

(b)

Figure 4-19: Uncorrected isochronal DSC results for β solution heat treated Ti-15Mo-0.15O at a heating rate of (a) 5 and (b) 50 CPM for temperatures in the range of 200 to 550°C.

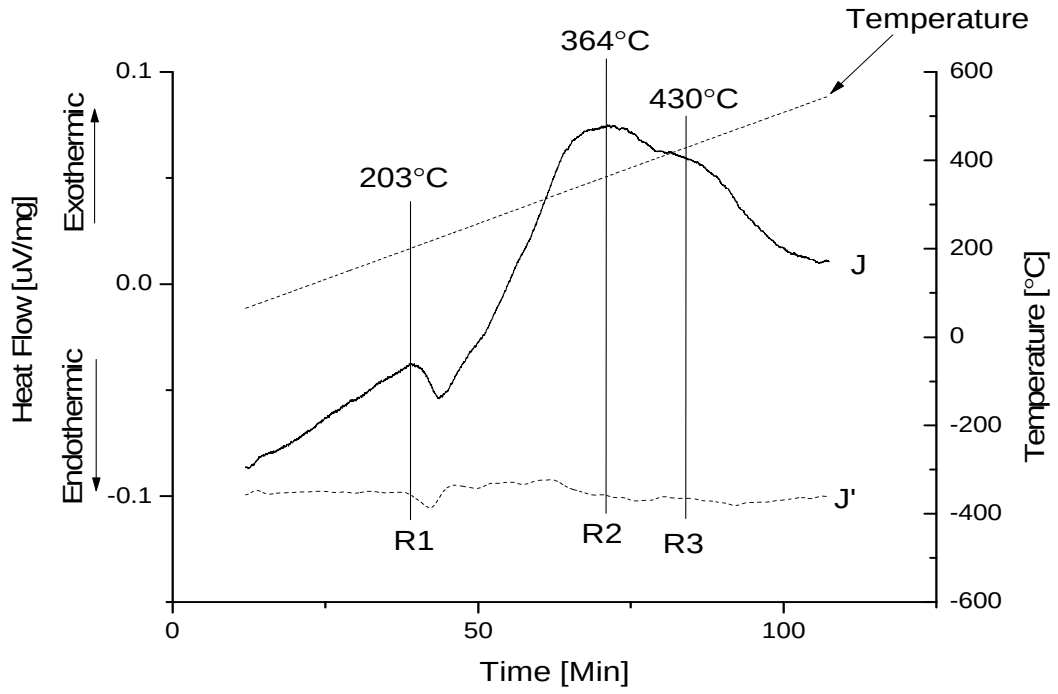

Figure 4-20: Corrected Heat Flow (J): dQ/dt vs time plot for solutionized Ti-15Mo-0.15O up to 550˚C with a scan rate of 5˚C per minute with baseline subtracted; dotted line below is the first derivative of J.

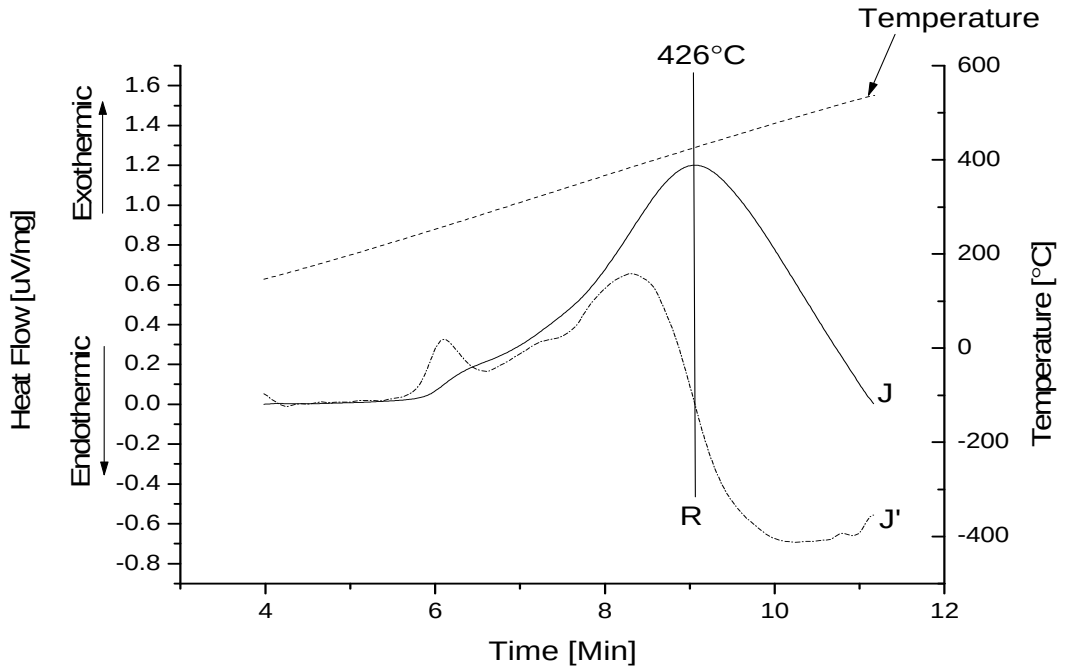

Figure 4-21: Corrected Heat Flow (J): dQ/dt vs time plot for solutionized Ti-15Mo-0.15O up to 550˚C with a scan rate of 50˚C per minute with baseline subtracted; dotted line below is the first derivative of J.

Table 4-5: Peak temperature for the occurring phase transformations during the 5 and 50°C per minute heat up of Ti-15Mo-0.15O alloy

Reaction	T_{Peak}
5˚CPM	
R1	203°C
R2	364°C
R3	430°C
50°CPM	
R	426˚C

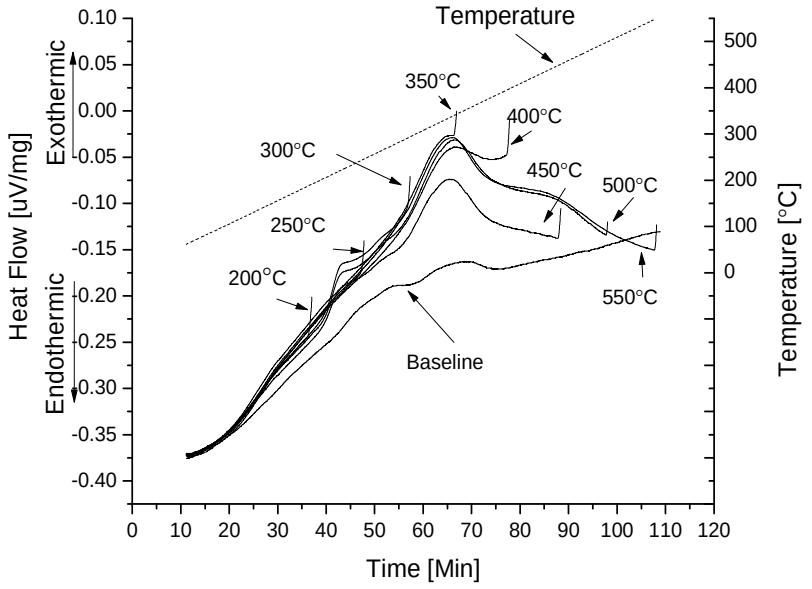

(a)

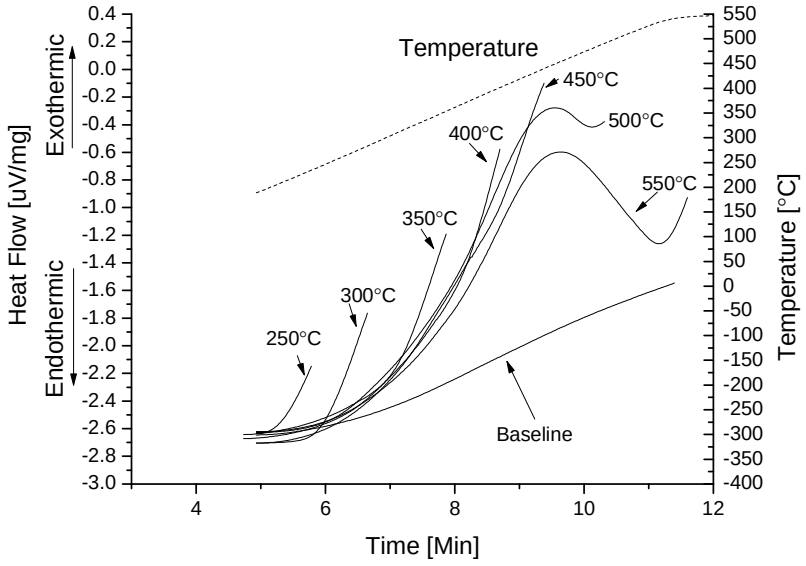

(b)

Figure 4-22: Uncorrected isochronal DSC results for β solution heat treated Ti-15Mo-0.35O at a heating rate of 5 and 50 CPM for temperatures in the range of 200 to 550°C.

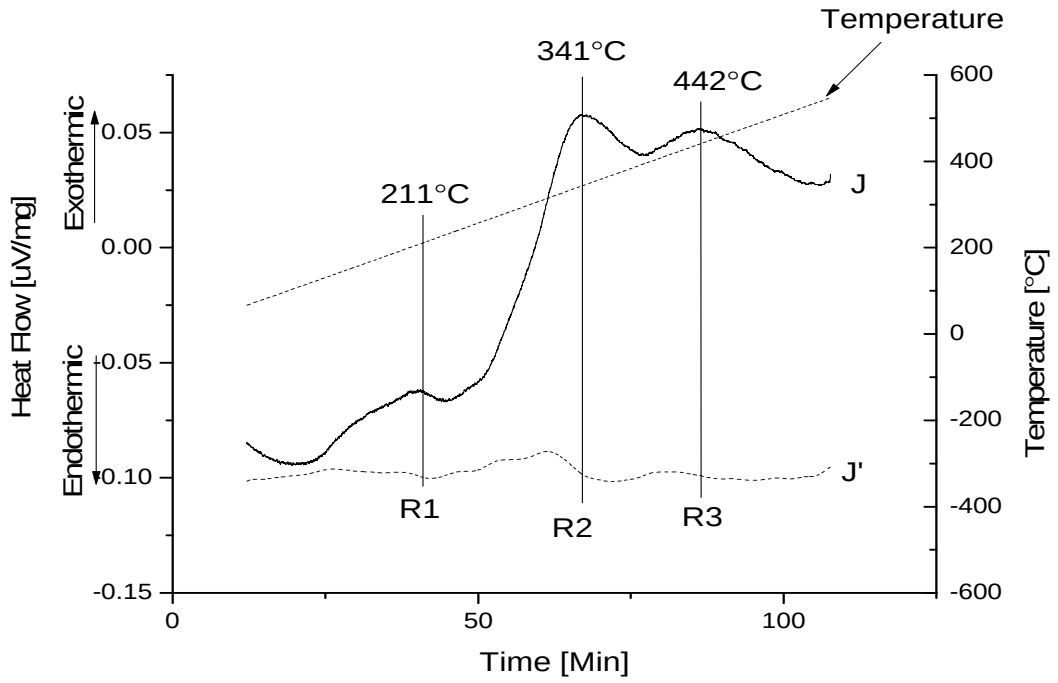

Figure 4-23: Corrected Heat Flow (J): dQ/dt vs time plot for solutionized Ti-15Mo-0.35O up to 550˚C with a scan rate of 5˚C per minute with baseline subtracted; dotted line below is the first derivative of J.

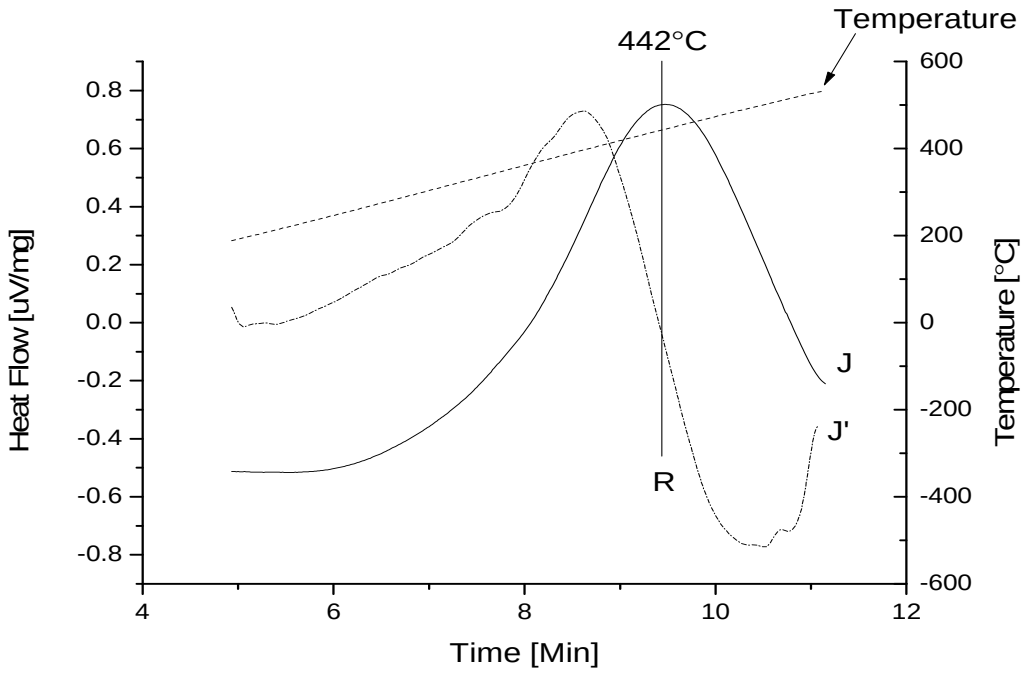

Figure 4-24: Corrected Heat Flow (J): dQ/dt vs time plot for solutionized Ti-15Mo-0.35O up to 550˚C with a scan rate of 50˚C per minute with baseline subtracted; dotted line below is the first derivative of J.

Table 4-6: Peak temperature for the occurring phase transformations during the 5 and 50°C per minute heat up of Ti-15Mo-0.35O alloy.

Reaction	T_{Peak}
5˚CPM	
R1	211°C
R2	341°C
R3	442°C
50°CPM	
R	442°C

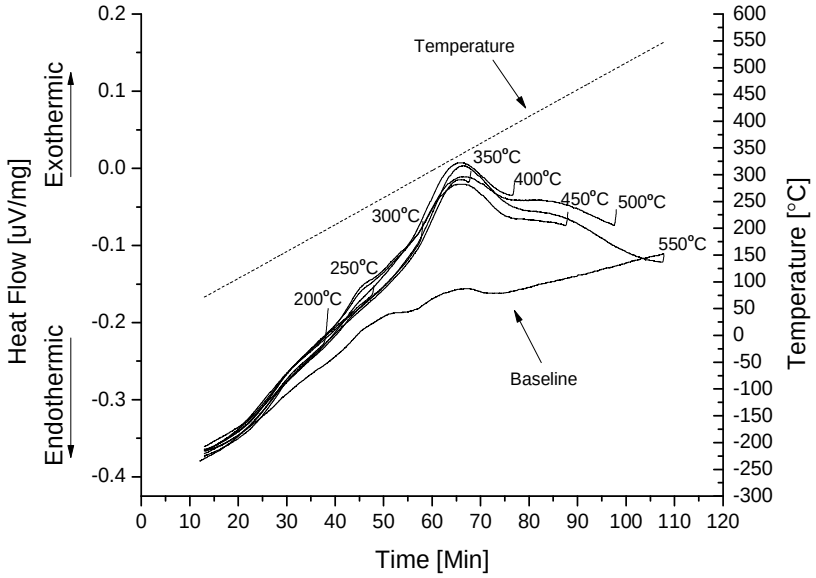

(a)

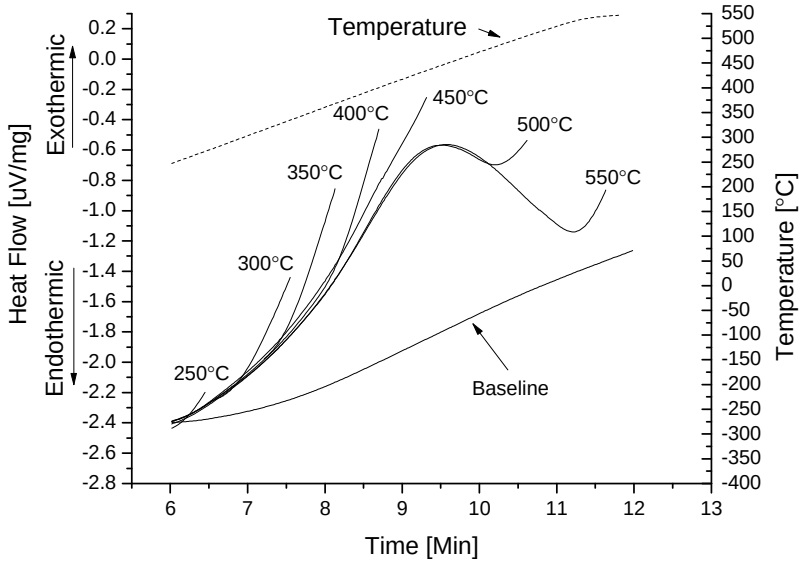

(b)

Figure 4-25: Uncorrected isochronal DSC results for β solution heat treated Ti-15Mo-0.5O at a heating rate of 5 and 50 CPM for temperatures in the range of 200 to 550°C.

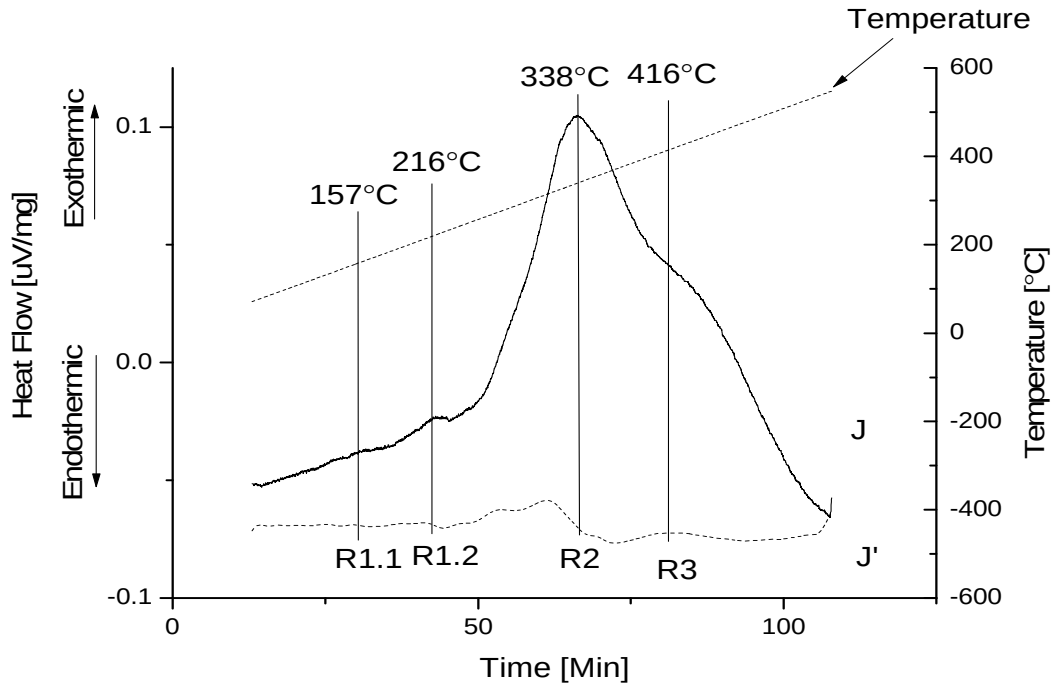

Figure 4-26: Corrected Heat Flow (J): dQ/dt vs time plot for solutionized Ti-15Mo-0.5O up to 550˚C with a scan rate of 5˚C per minute with baseline subtracted; dotted line below is the first derivative of J.

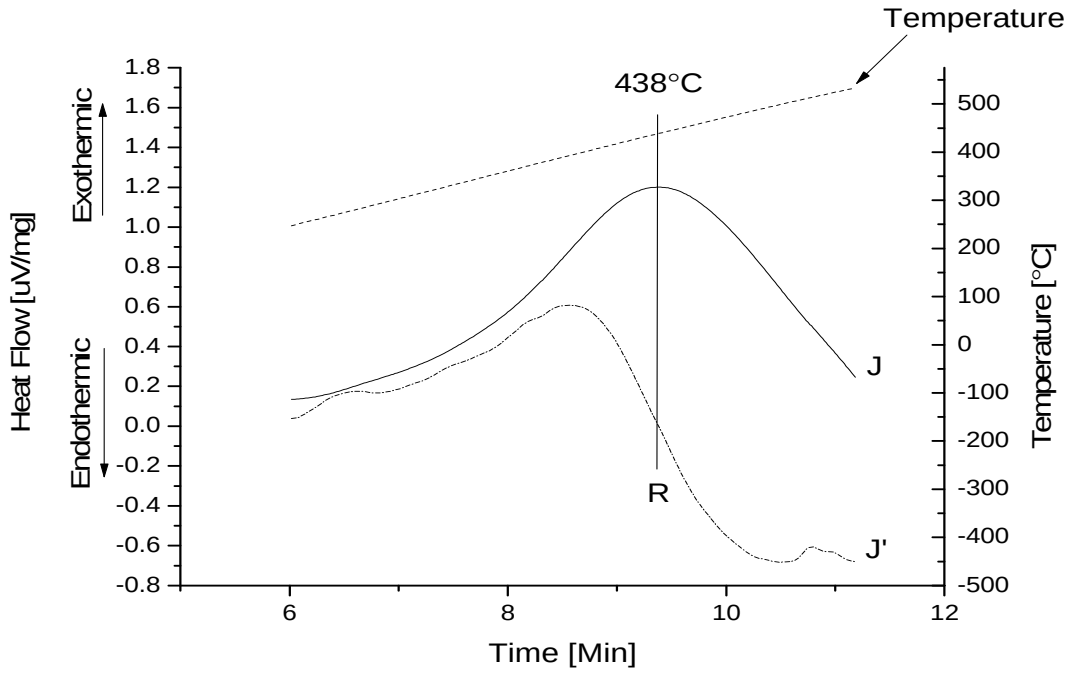

Figure 4-27: Corrected Heat Flow (J): dQ/dt vs time plot for solutionized Ti-15Mo-0.5O up to 550˚C with a scan rate of 50˚C per minute with baseline subtracted; dotted line below is the first derivative of J.

Table 4-7: Peak temperature for the occurring phase transformations during the 5 and 50°C per minute heat up of Ti-15Mo-0.5O alloy.

Reaction	T_{Peak}
5˚CPM	
R1.1	157°C
R1.2	216°C
R2	338°C
R3	416°C
50°CPM	
R	438°C

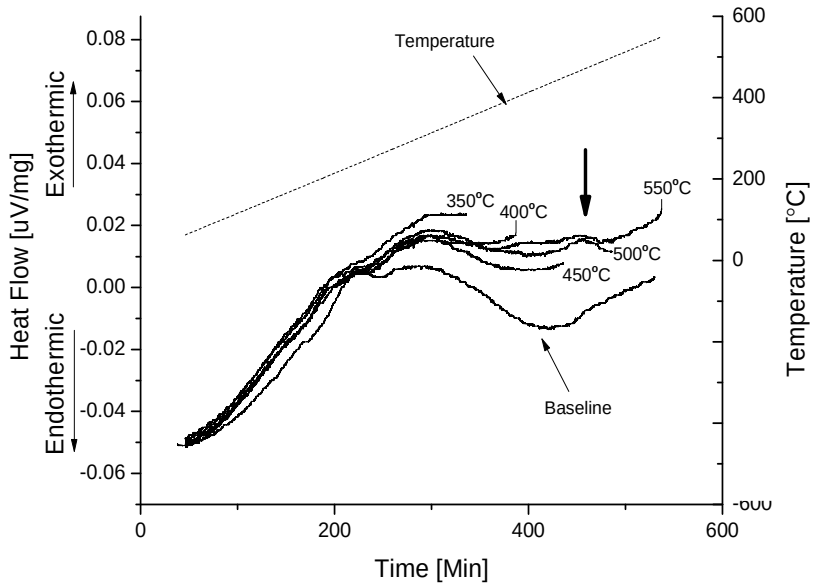

(a)

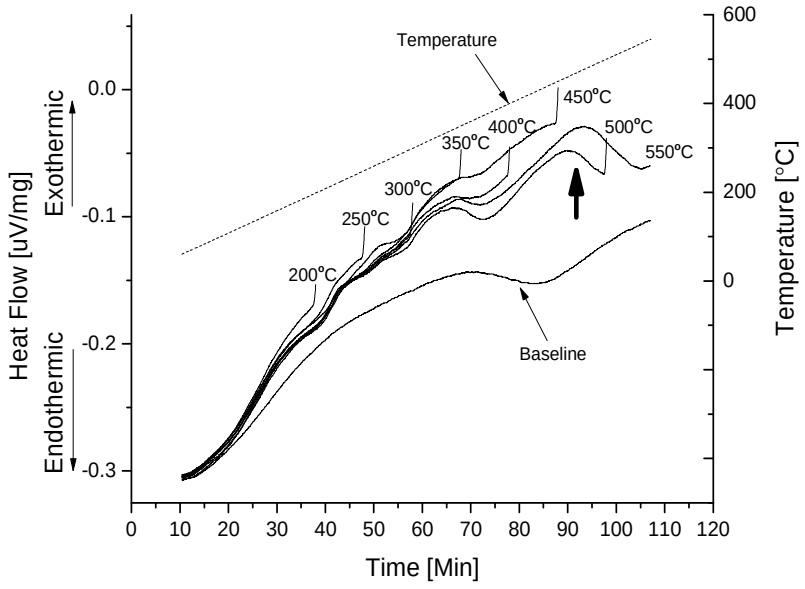

(b)

Figure 4-28: Uncorrected isochronal DSC results for β solution heat treated Ti-15Mo-2O at a heating rate of 1 (a), 5 (b) and 50 CPM (c) for temperatures in the range of 200 to 550°C.

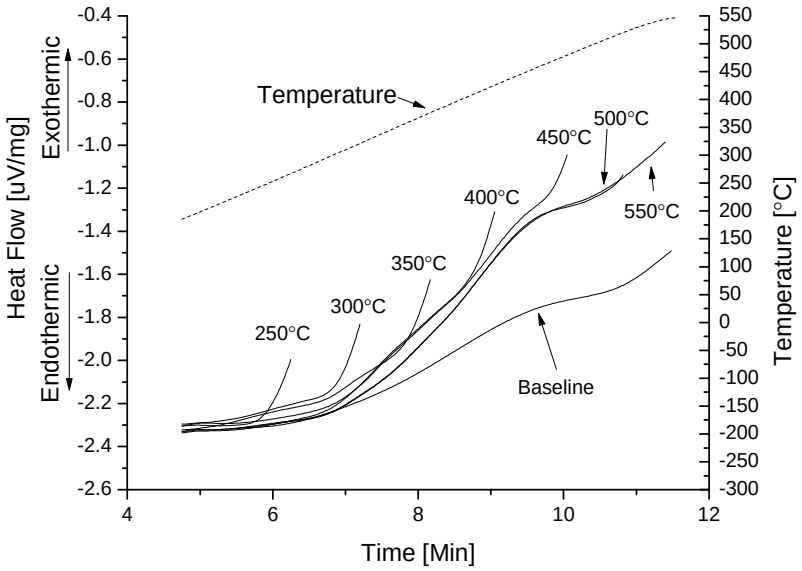

(c)

Figure 4-28: continued

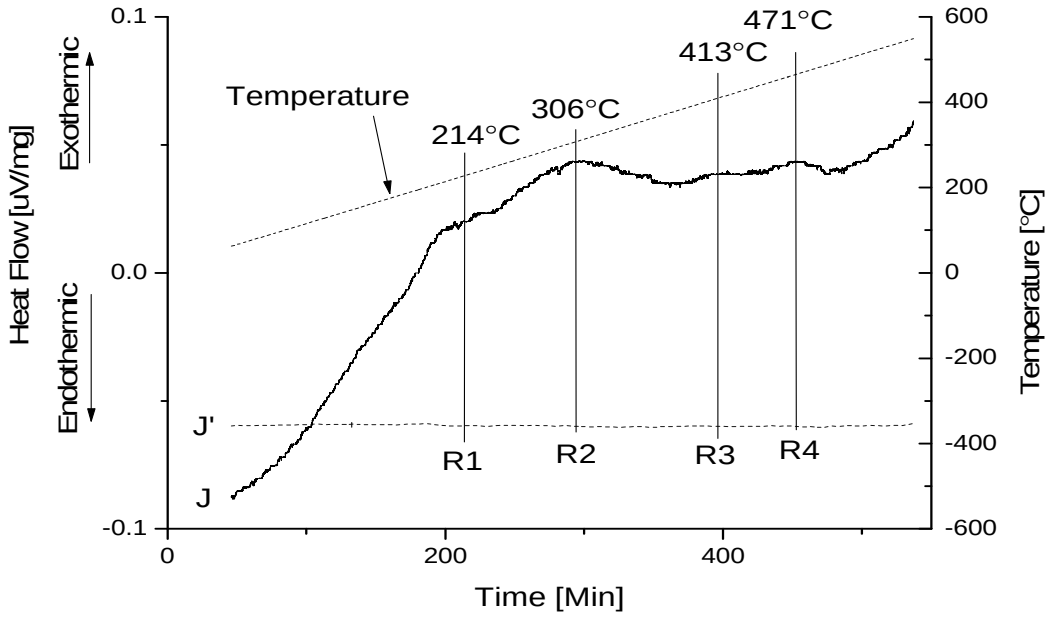

Figure 4-29: Corrected Heat Flow (J): dQ/dt vs time plot for solutionized Ti-15Mo-2O up to 550˚C with a scan rate of 1˚C per minute with baseline subtracted; dotted line below is the first derivative of J.

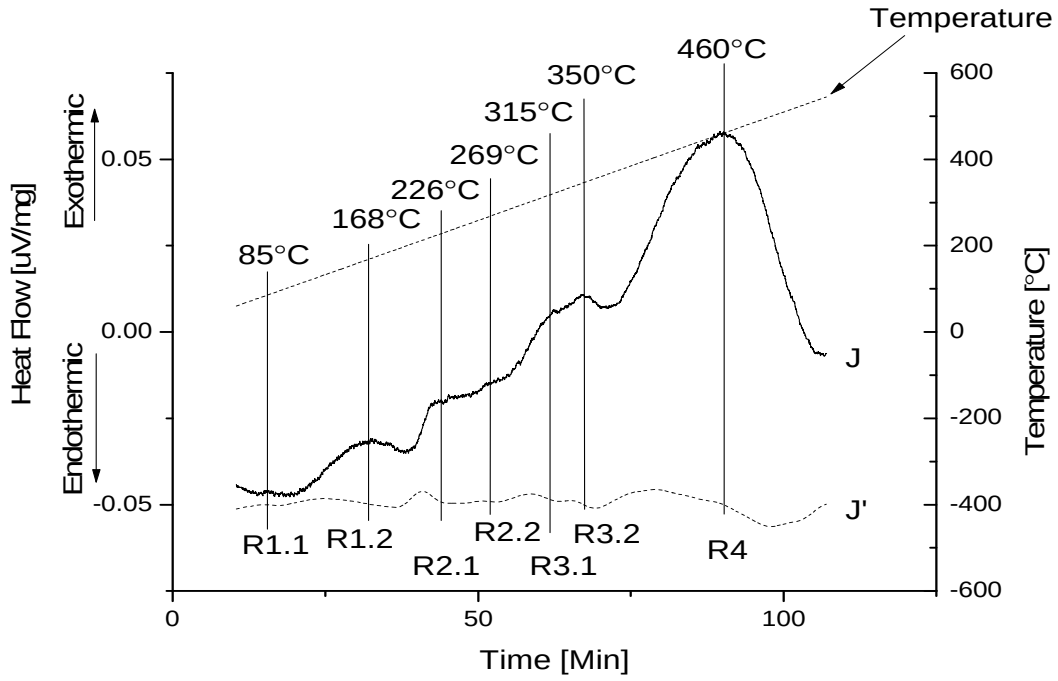

Figure 4-30: Corrected Heat Flow (J): dQ/dt vs time plot for solutionized Ti-15Mo-2O up to 550˚C with a scan rate of 5˚C per minute with baseline subtracted; dotted line below is the first derivative of J.

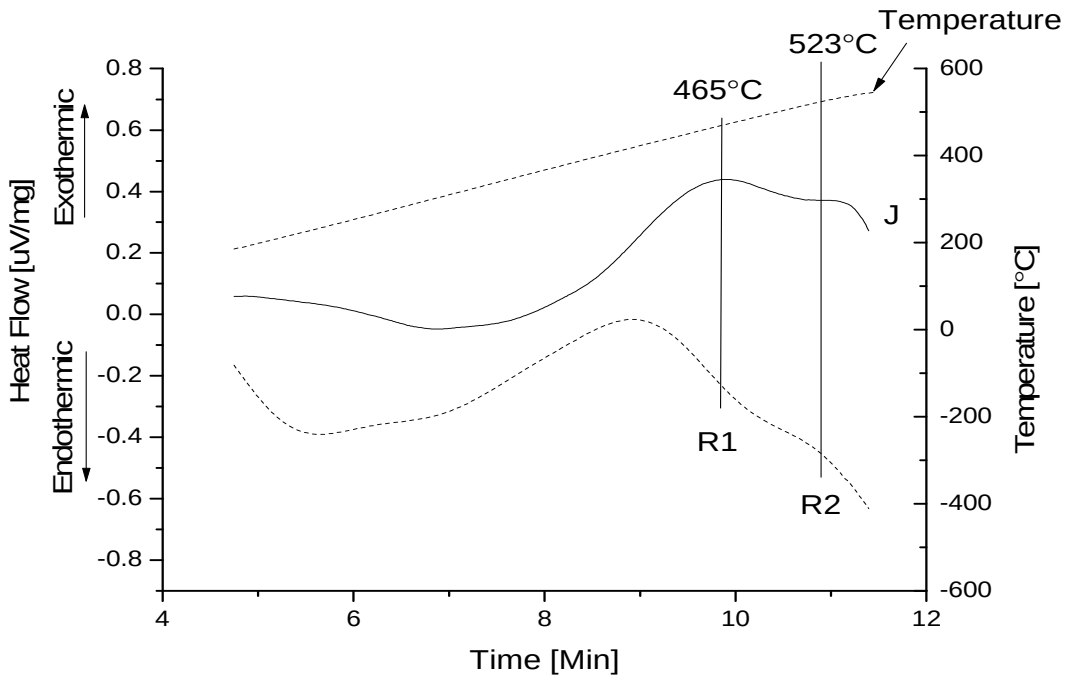

Figure 4-31: Corrected Heat Flow (J): dQ/dt vs time plot for solutionized Ti-15Mo-2O up to 550˚C with a scan rate of 50˚C per minute with baseline subtracted; dotted line below is the first derivative of J.

Table 4-8: Peak temperature for the occurring phase transformations during the 5 and 50°C per minute heat up of Ti-15Mo-2O alloy.

Reaction	T_{Peak}
Ti-15Mo-20-1CPM	
R1	214C
R2	306°C
R3	413°C
R4	471°C
Ti-15Mo-20-5°CPM	
R1.1	85°C
R1.2	168°C
R2.1	226°C
R2.2	269°C
R3.1	315°C
R3.2	350°C
R4	460°C
50˚CPM	
R1	465°C
R2	523°C

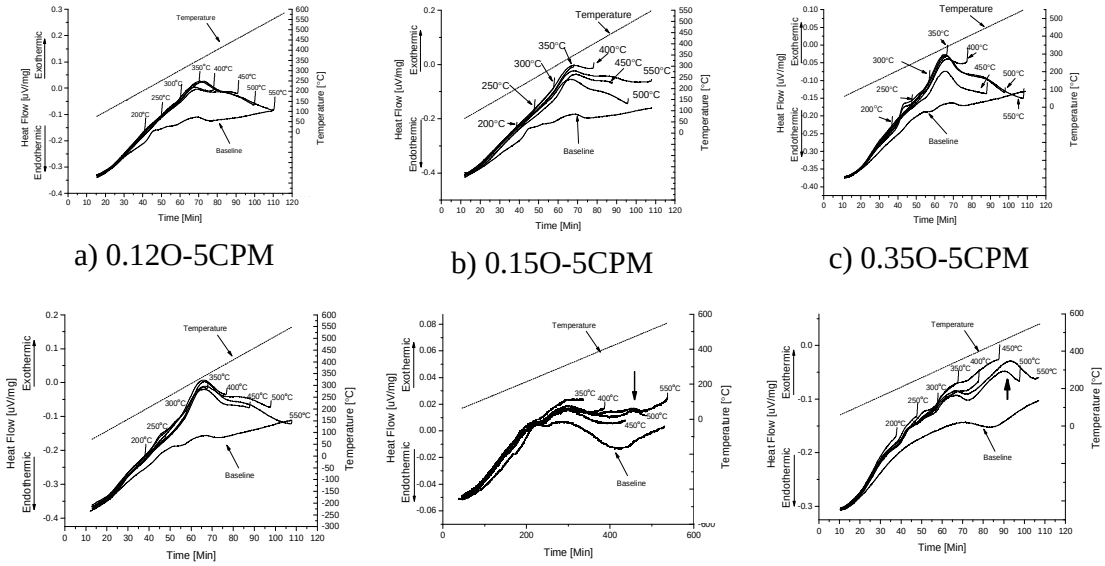

a) 0.12O-5CPM b) 0.15O-5CPM c) 0.35O-5CPM

d) 0.5O-5CPM e) 2O-1CPM f) 2O-5CPM

Figure 4-32: DSC compilation for Ti-15Mo-O using a heating rate of 1 and 5 CPM for temperatures in the range of 200 to 550°C.

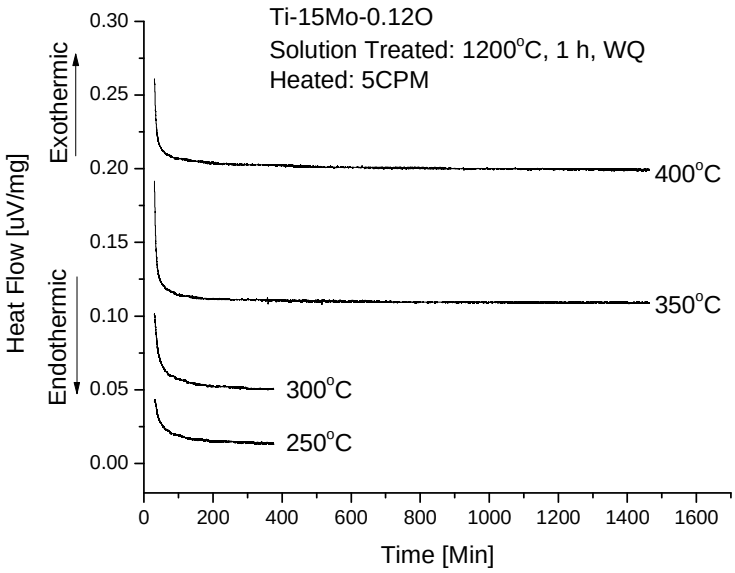

a

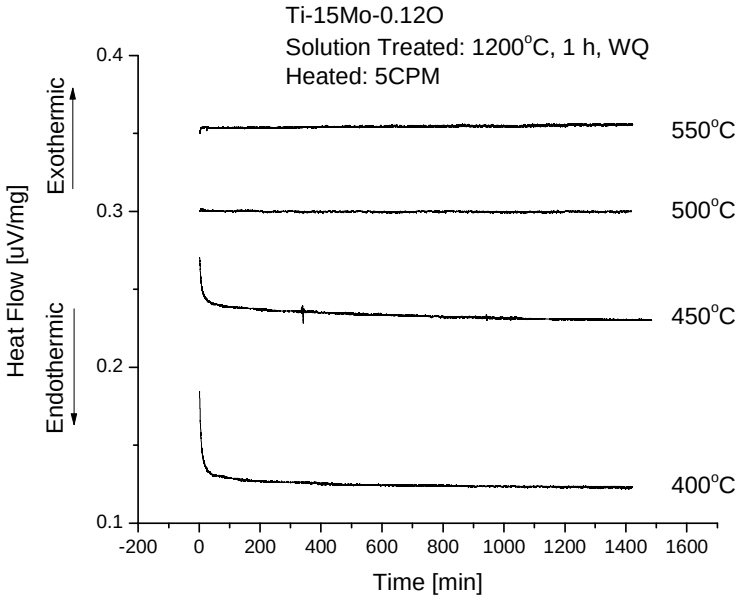

b

Figure 4-33: Overview of the isothermal response of Ti-15Mo-0.12O isothermally aged at 250°C -400°C (a) and at 400°C - 550°C (b) at 5CPM.

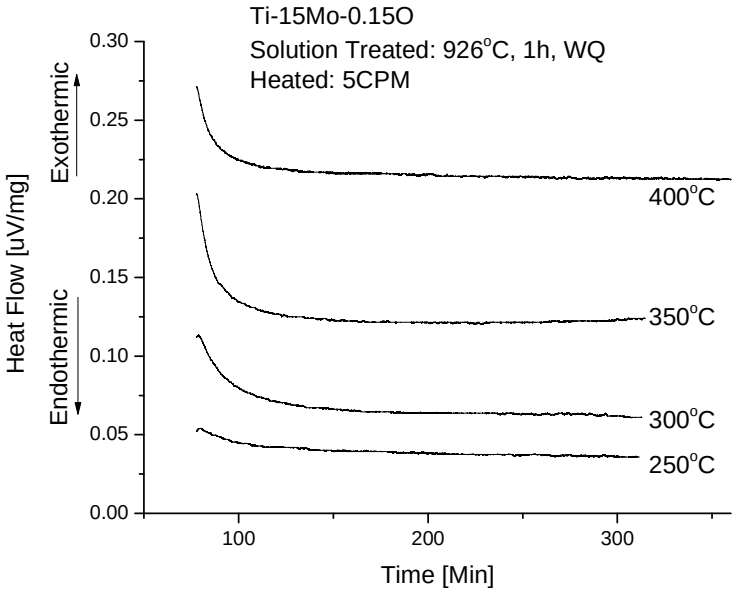

a

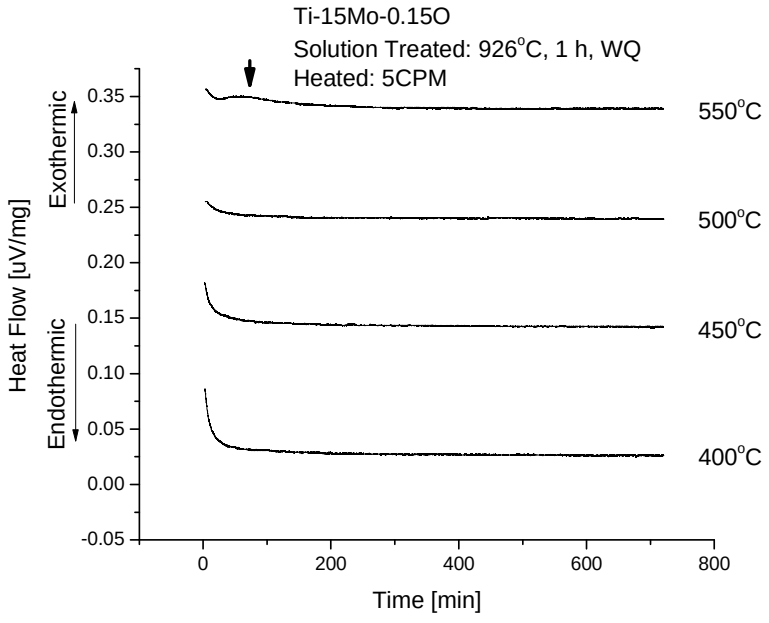

b

Figure 4-34: Overview of the isothermal response of Ti-15Mo-0.15O isothermally aged at 250°C - 400°C (a) and at 400°C - 550°C (b) at 5CPM.

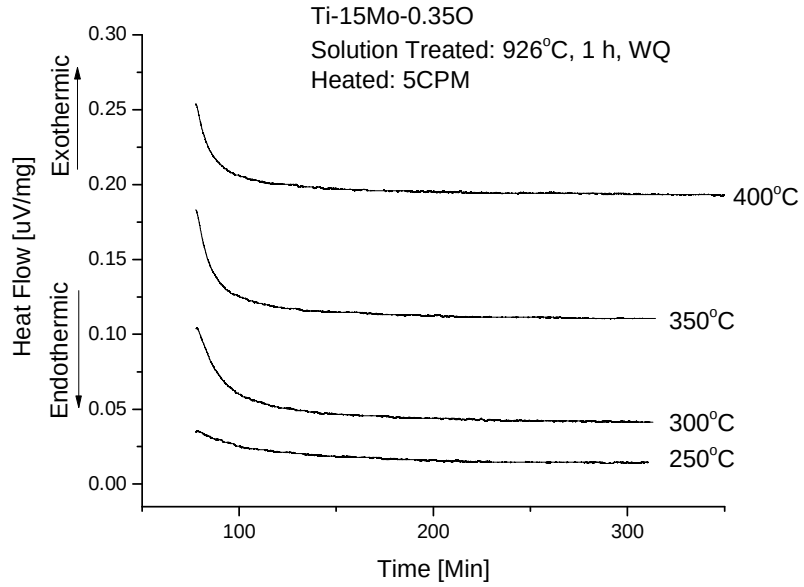

a

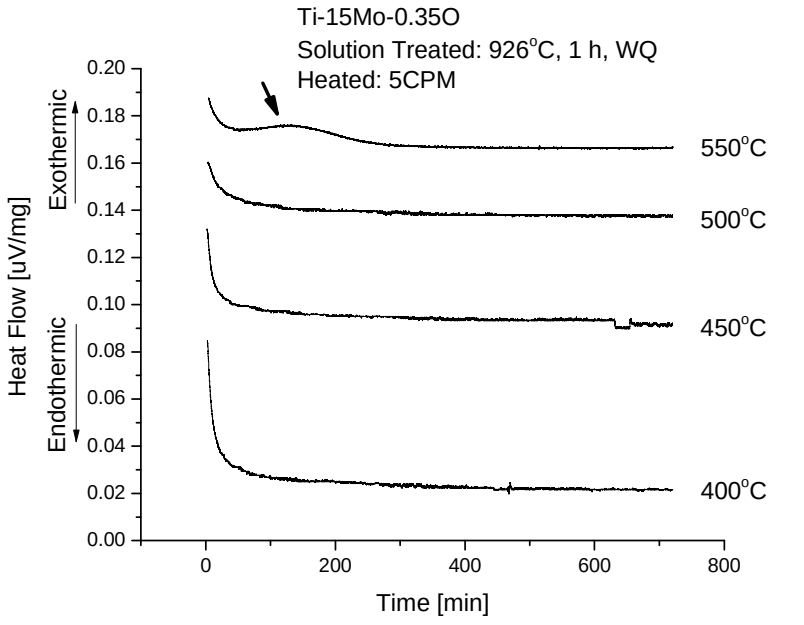

b

Figure 4-35: Overview of the isothermal response of Ti-15Mo-0.35O isothermally aged at 250°C - 400°C (a) and at 400°C - 550°C (b) at 5CPM.

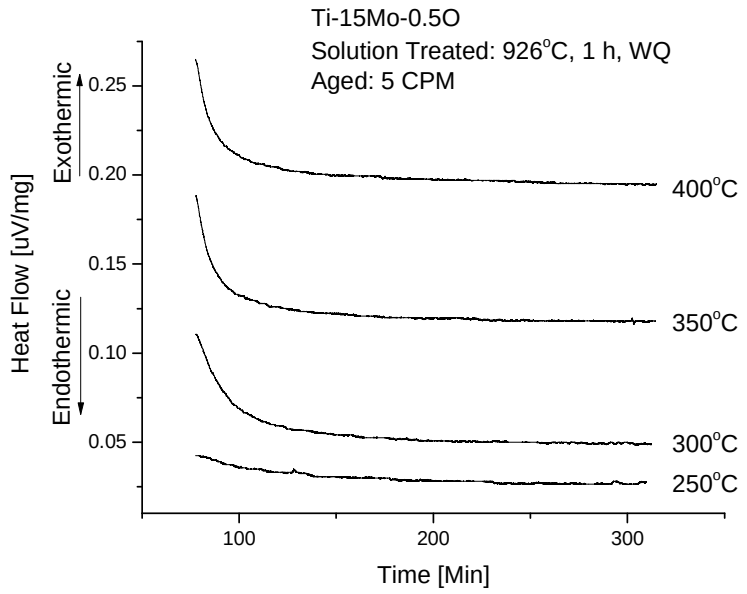

a

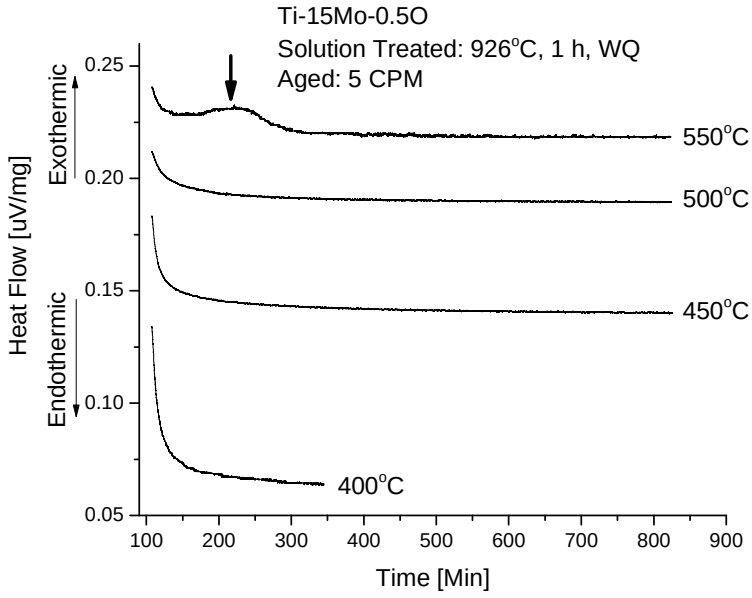

b

Figure 4-36: Overview of the isothermal response of Ti-15Mo-0.5O isothermally aged at 250°C - 400°C (a) and at 400°C - 550°C (b) at 5CPM.

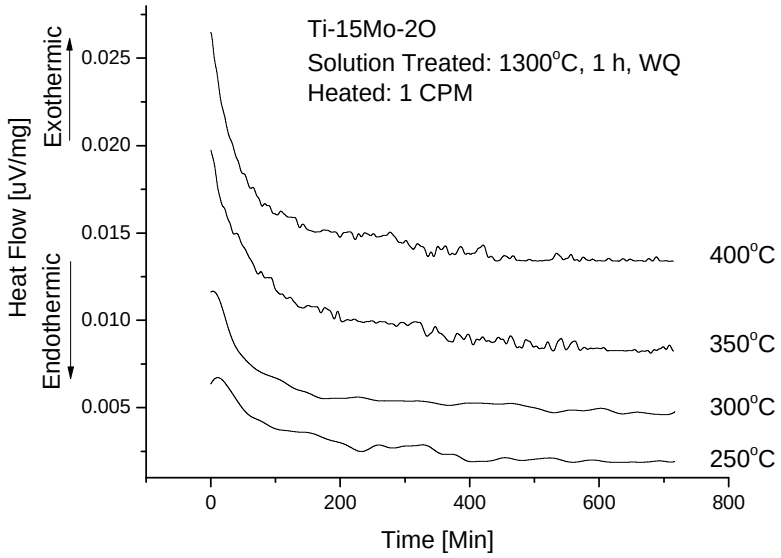

a

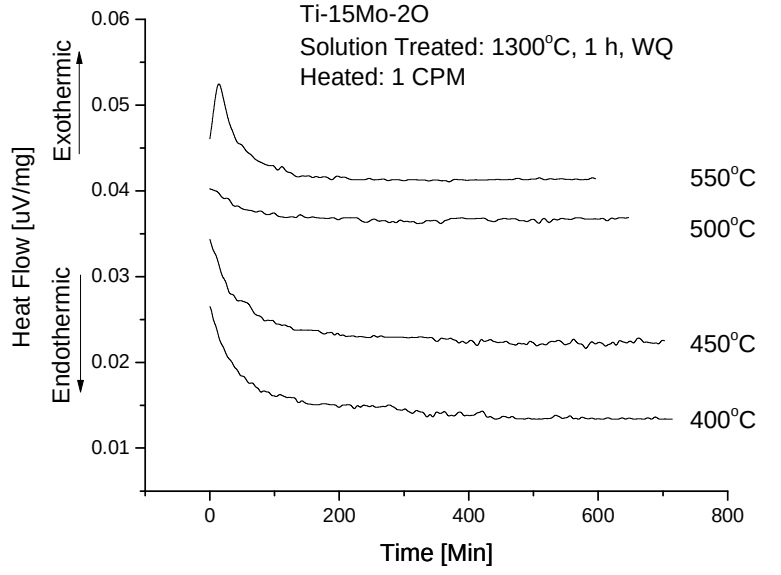

b

Figure 4-37: Overview of the isothermal response of Ti-15Mo-2O isothermally aged at 250°C - 400°C (a) and at 400°C - 550°C (b) at 1CPM.

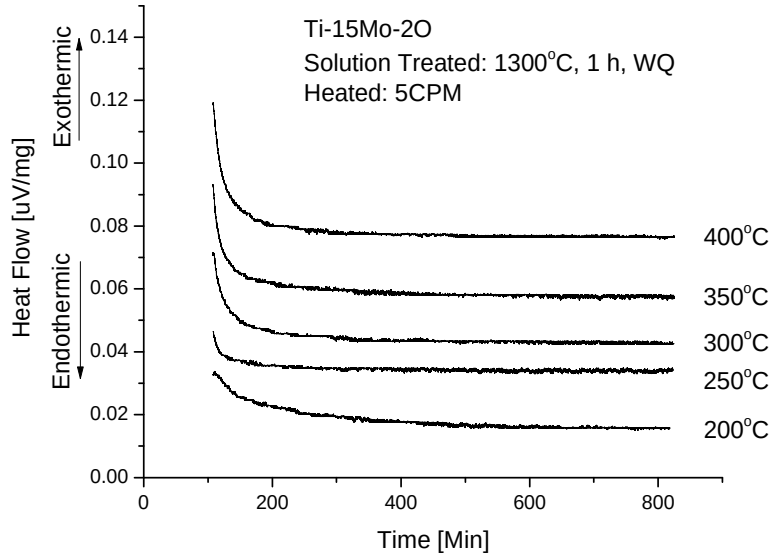

a

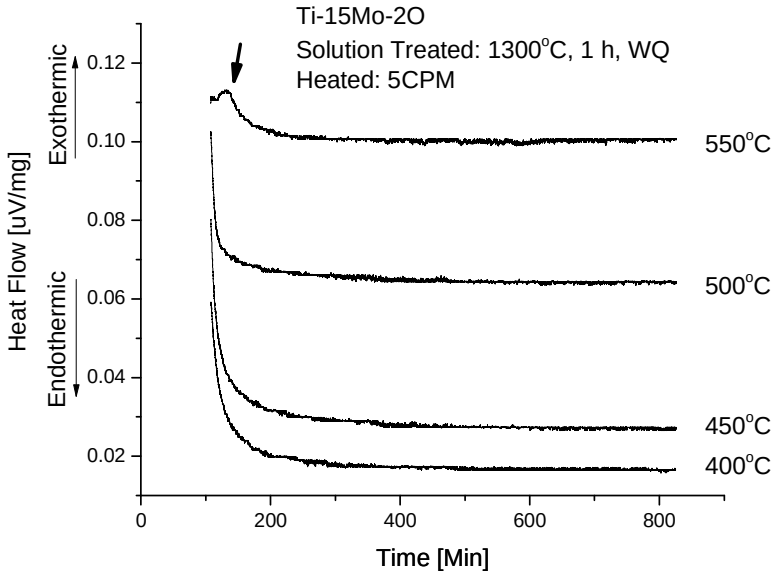

b

Figure 4-38: Overview of the isothermal response of Ti-15Mo-0.5O isothermally aged at 250°C - 400°C (a) and at 400°C - 550°C (b) at 5CPM.

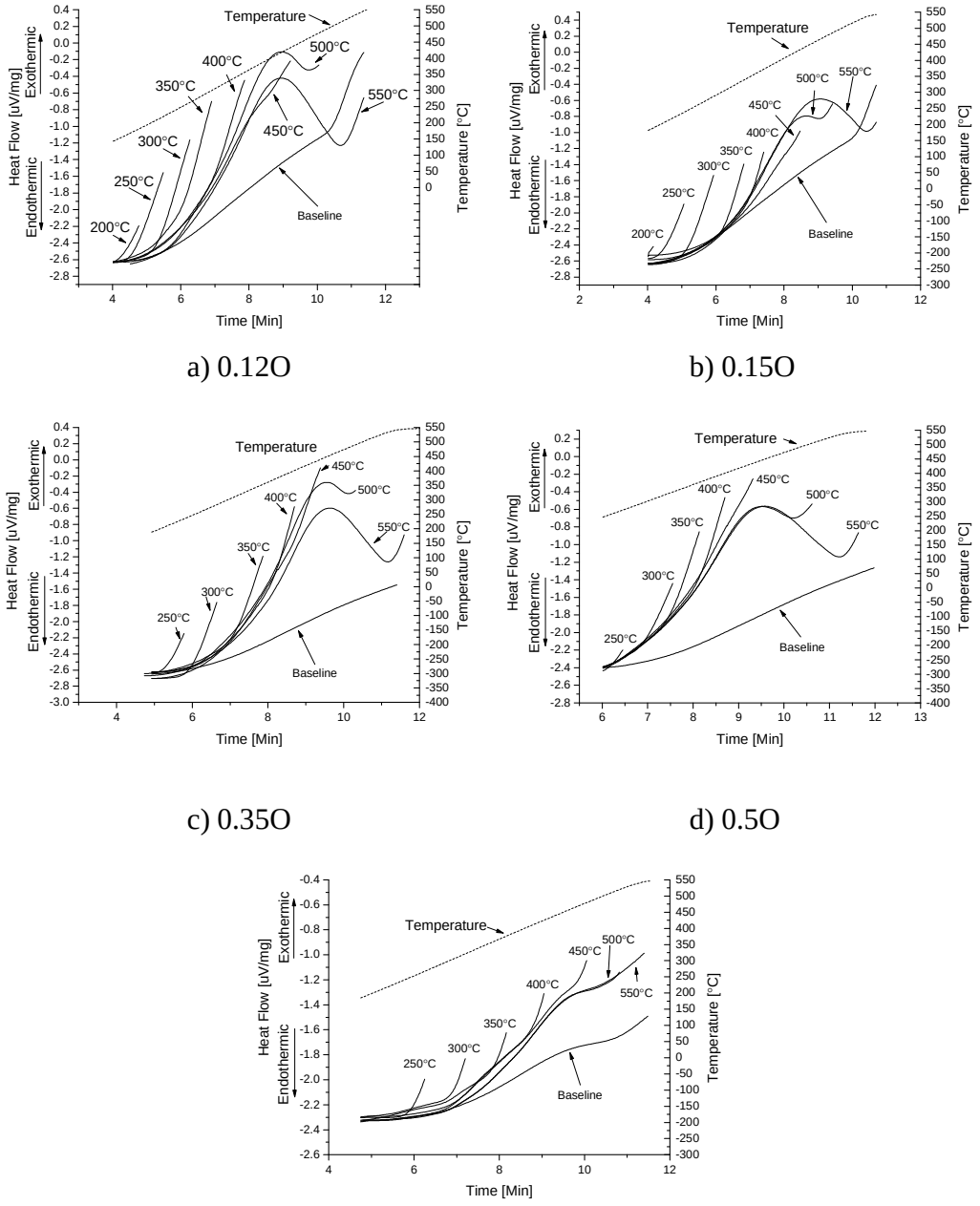

a) 0.12O

b) 0.15O

c) 0.35O

d) 0.5O

e) 2O

Figure 4-39: DSC compilation for Ti-15Mo-O using a heating rate of 50 CPM for temperatures in the range of 200 to 550°C.

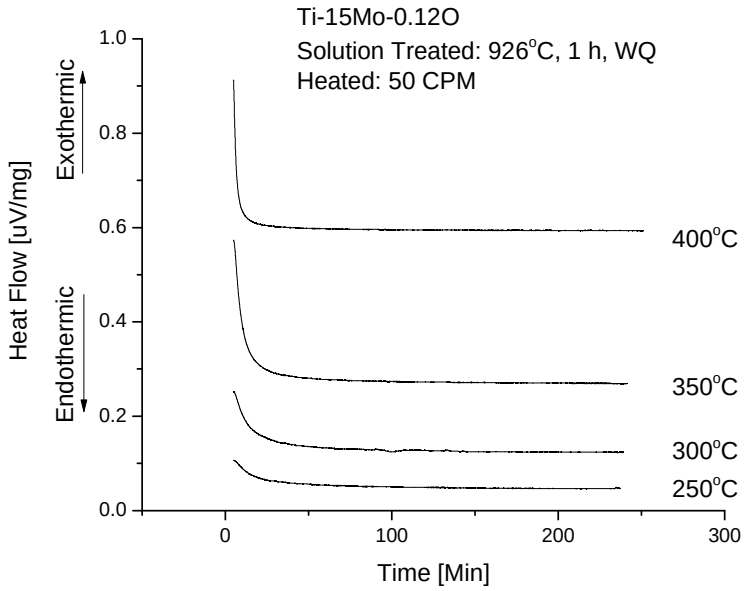

a

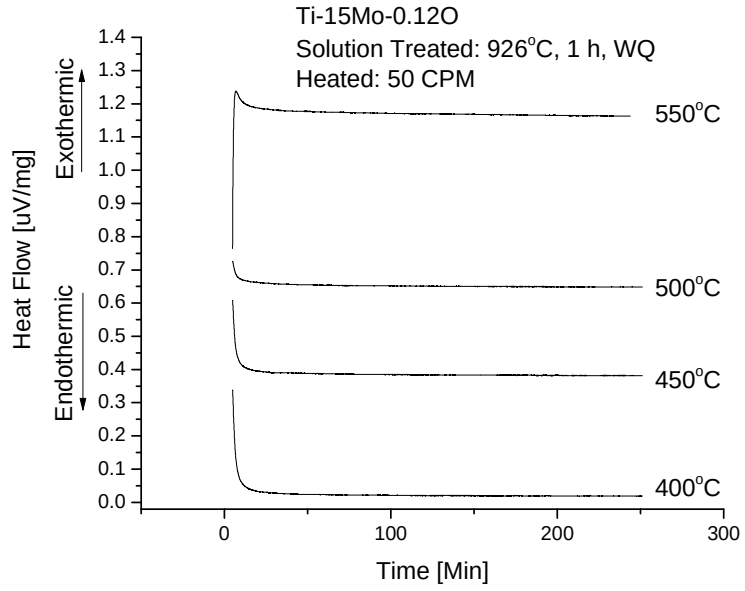

b

Figure 4-40: Overview of the isothermal response of Ti-15Mo-0.12O isothermally aged at 250°C - 400°C (a) and at 400°C - 550°C (b) at 50CPM.

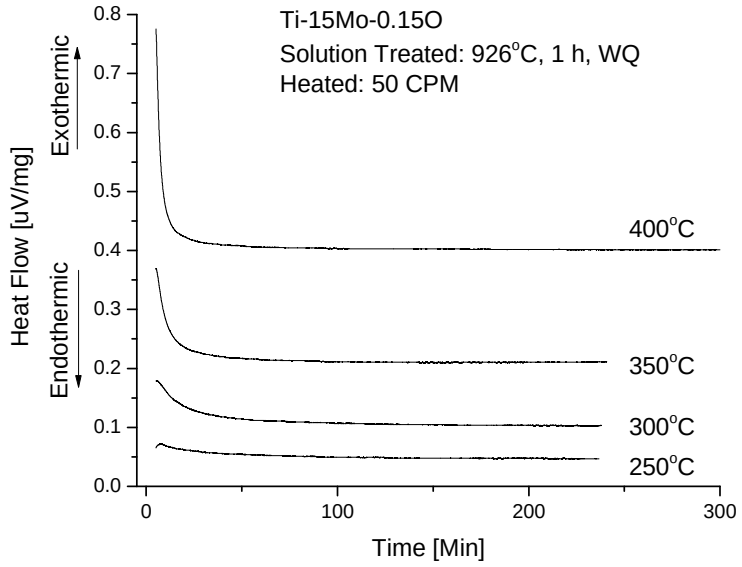

a

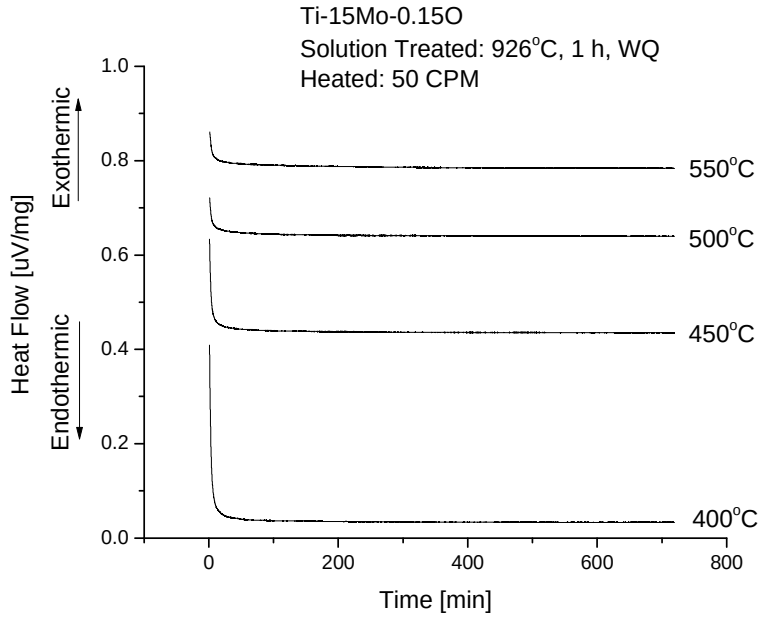

b

Figure 4-41: Overview of the isothermal response of Ti-15Mo-0.15O isothermally aged at 250°C - 400°C (a) and at 400°C - 550°C (b) at 50CPM.

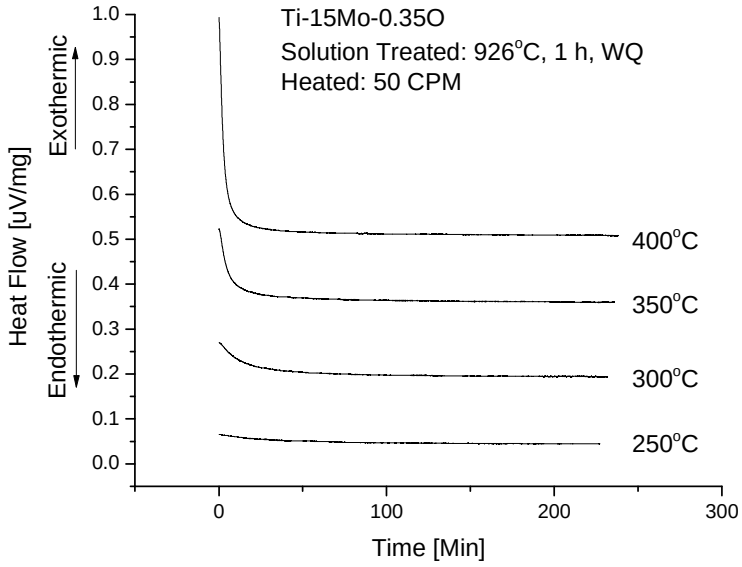

a

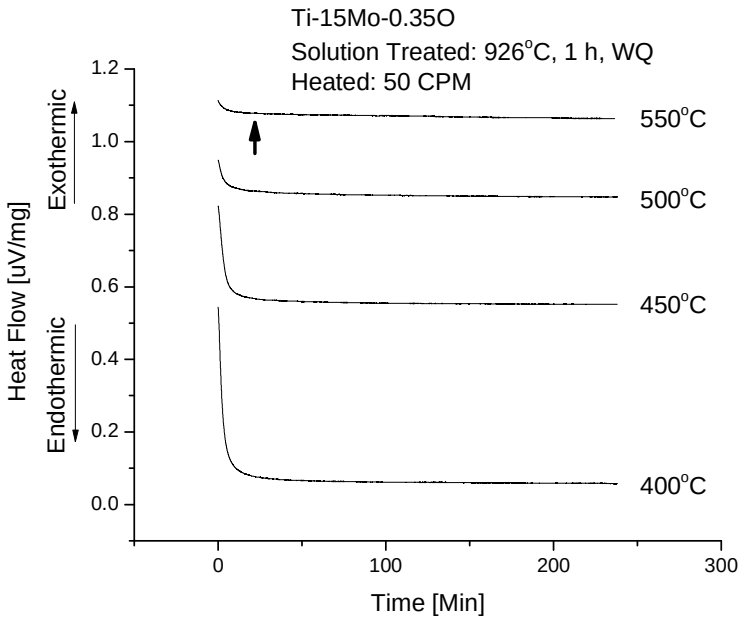

b

Figure 4-42: Overview of the isothermal response of Ti-15Mo-0.35O isothermally aged at 250°C - 400°C (a) and at 400°C - 550°C (b) at 50CPM.

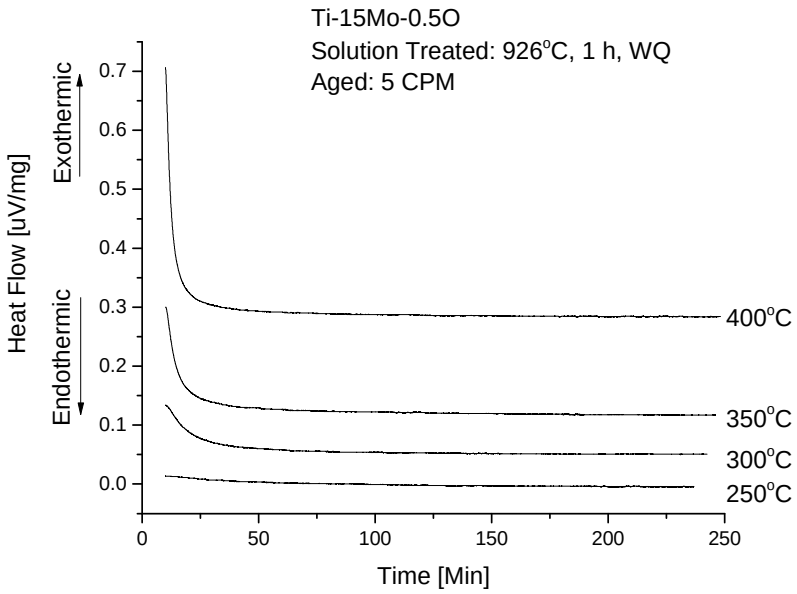

a

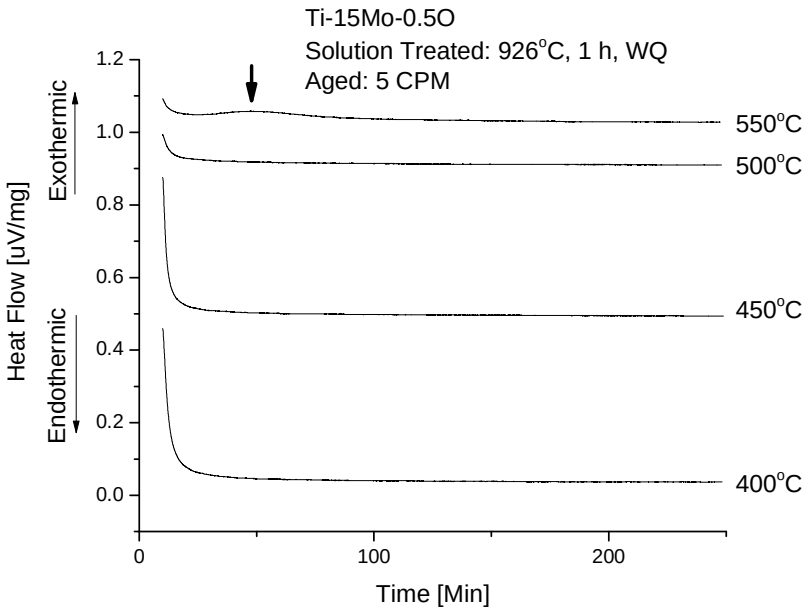

b

Figure 4-43: Overview of the isothermal response of Ti-15Mo-0.5O isothermally aged at 250°C - 400°C (a) and at 400°C - 550°C (b) at 50CPM.

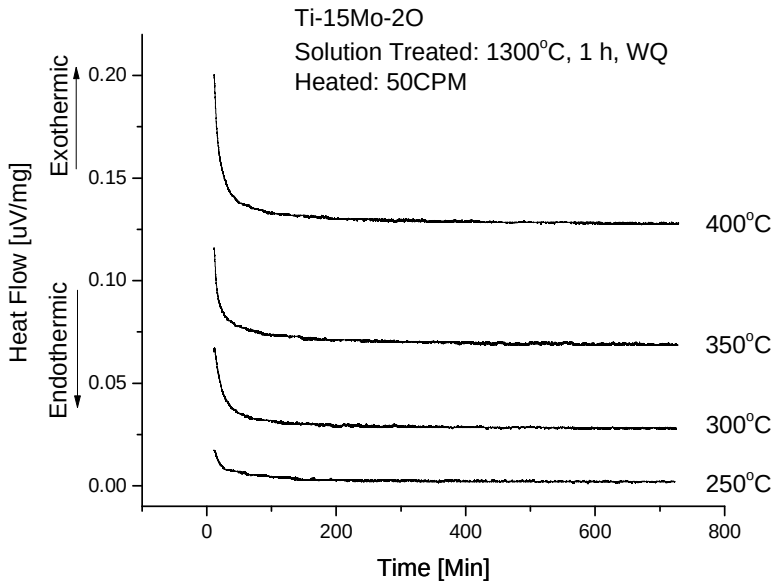

a

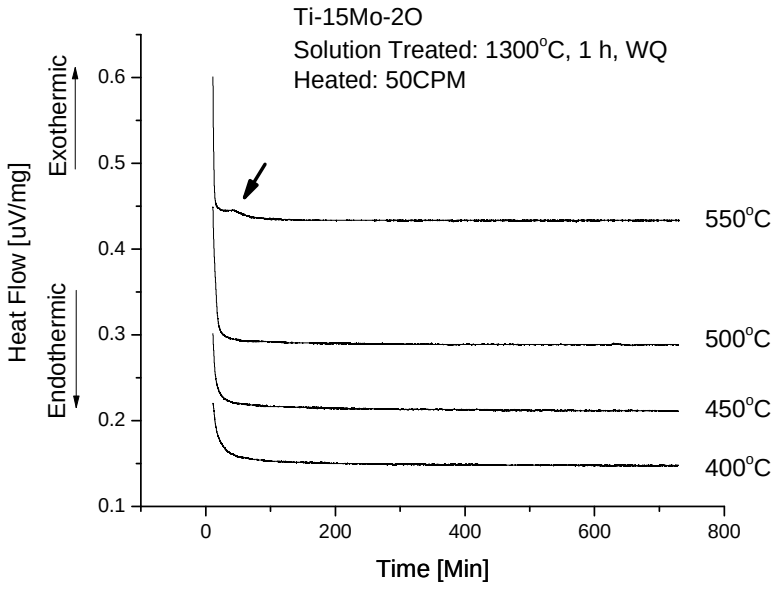

b

Figure 4-44: Overview of the isothermal response of Ti-15Mo-2O isothermally aged at 250°C - 400°C (a) and at 400°C - 550°C (b) at 50CPM.

4.3. Single Crystals

Figure 4-45 illustrates the two dimensional diffractions pattern for Ti-15Mo-0.15/ 0.5/ 1O single crystals recorded along the x-axis obtained in this investigation. All specimens showed single diffraction spots, Figure 4-45 a-c, the crystals being oriented such that the surface normals were within 2 or 3 degrees of [100]. Additionally, the positions of oxygen atoms were allocated by locating areas of residual electron density, using the DIAMOND software package [1-3]. First were the positions of the Ti and Mo atoms were assigned, assuming 8 atomic percent (at%) Mo atoms in the 0.5, 0.5, 0.5 location and Ti (balanced) atoms occupying the other bcc lattice positions (0, 0, 0). The results for the residual electron density after subtracting the assigned Ti and Mo intensities are shown in Table 4-9. The not associated residual electron densities observed are Q1 and Q2. The Q1 residual electron density is associated with the 0.5, 0.25, 0.0 lattice site. This indicates that the oxygen atoms prefer the tetrahedral interstitial site in bcc crystals location. The remaining residual electron density, Q2, was associated with the 0.18, 0.0, 0.18 lattice sites and was associated with thermal motion of the Ti and Mo atoms at room temperature. The Mercury software package [4] provides a visualization of the aforementioned single crystal results from Figure 4-46 after processing, Table 4-3, as can be seen in Figure 4-47 a and b, where the solid atoms were Ti or Mo atoms and the white, smaller atoms, the interstitial oxygen atoms in their tetrahedral lattice position.

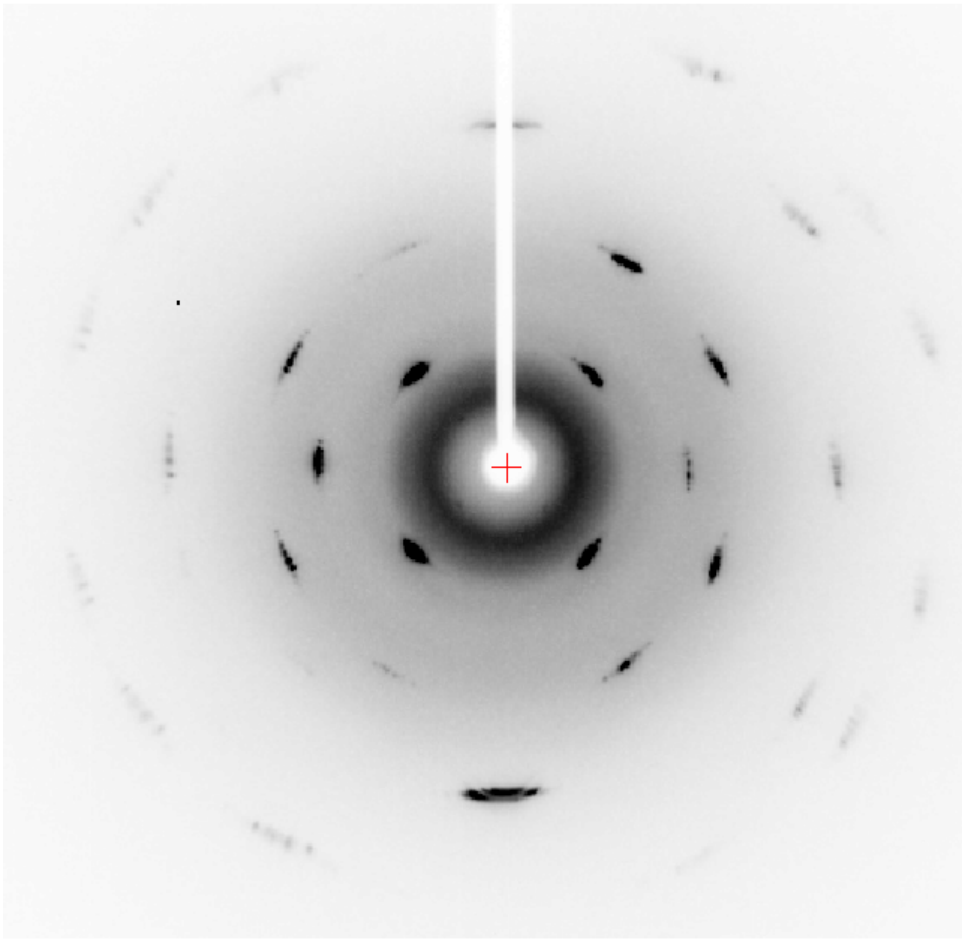

(a)

Figure 4-45: 2-dimensional diffraction pattern for the x-axis of Ti-15Mo-0.15O (a), Ti-15Mo-0.5O (b) and Ti-15Mo-1O (c).

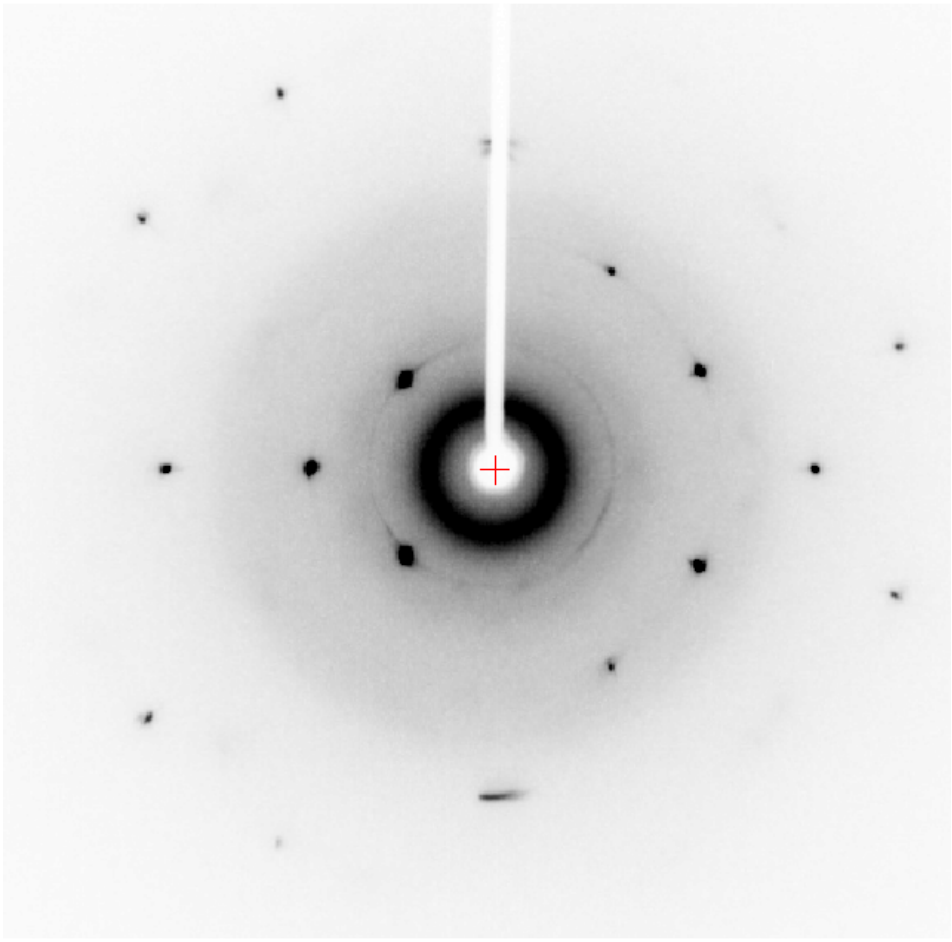

(b)

Figure 4-45: continued

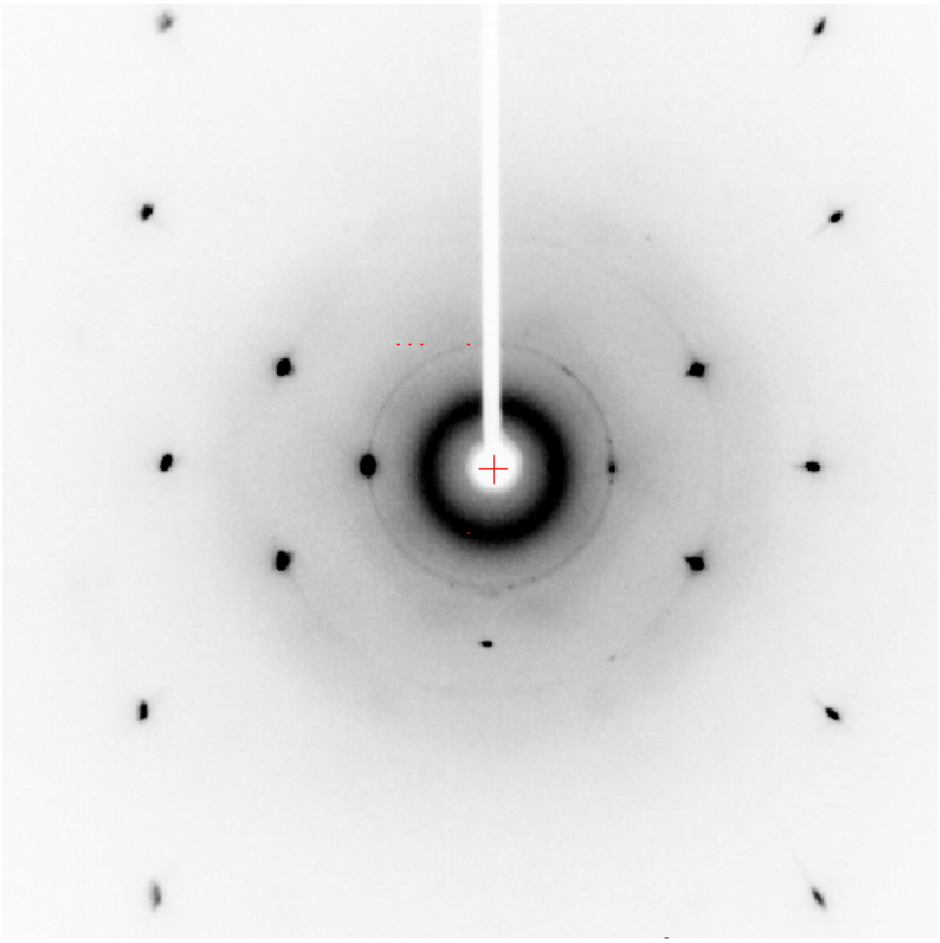

(c)

Figure 4-45: continued

Table 4-9: DIAMOND simulation results for Ti-15Mo-1O exhibiting the lattice location associated with the residual electron densities Q1 and Q2 based on the Fourier analysis.

Atoms	Atomic percent	Location		
		x	y	z
Ti	balanced	0.0000	0.0000	0.0000
Mo	8at%	0.5000	0.5000	0.5000
Residual Electron Density		Location		
		x	y	z
Q1		0.0000	0.2500	0.5000
Q2		0.1893	0.0000	0.1893

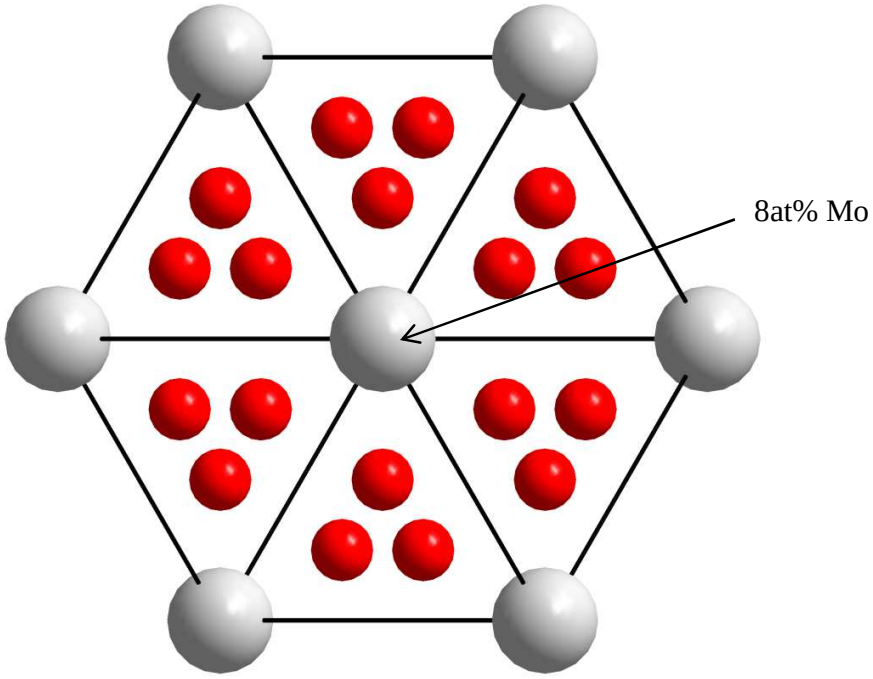

(a)

Figure 4-46: Simulation of oxygen location in the tetrahedral interstitial sites of the bcc lattice, view of the [111] direction (a) and [111] orientation (b)

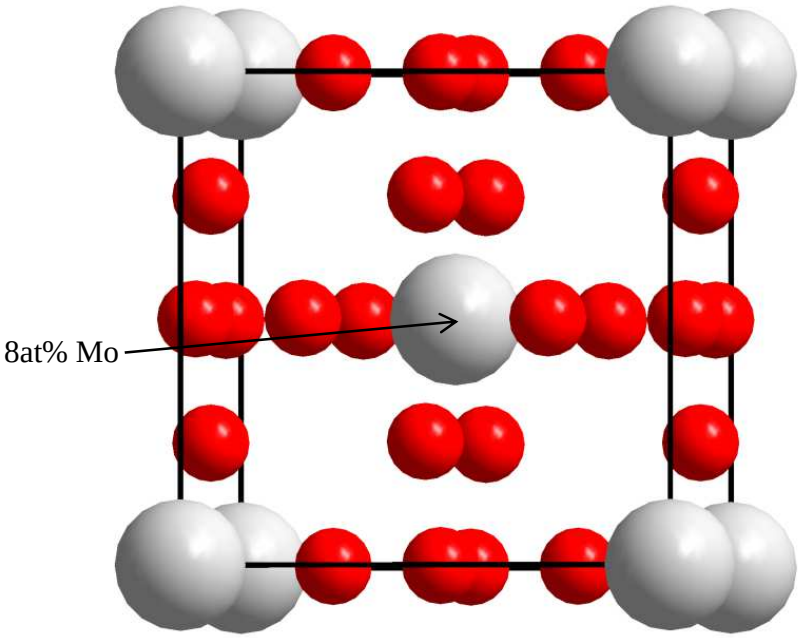

(b)

Figure 4-46: continued

4.4. References:

[1] Jacobson, R. (1998). *REQAB* Version 1.1. Molecular Structure Corporation, The Woodlands, Texas, USA. Molecular Structure Corporation & Rigaku (2006). *CrystalClear* MSC, The Woodlands, Texas, USA, and Rigaku Corporation, Tokyo, Japan.

[2] Sheldrick, G. M. (2008). *SHELXTL* Version 6.10 Acta Cryst. A64, 112-122. Mercury CSD 2.0 - New Features for the Visualization and Investigation of Crystal Structures

[3] Brandenburg, K. (1999). DIAMOND, Crystal Impact GbR, Bonn, Germany

[4] C. F. Macrae, I. J. Bruno, J. A. Chisholm, P. R. Edgington, P. McCabe, E. Pidcock, L. Rodriguez-Monge, R. Taylor, J. van de Streek and P. A. Wood, *J. Appl. Cryst.*, **41**, 466-470, 2008

CHAPTER FIVE

5. DISCUSSION

5.1. ω Phase

The ω phase transformation in bcc titanium alloys is considered to form either on quenching (athermal) or on aging (isothermal). The former is based on a displacive shuffle of atoms on the (111) planes along the <111> direction with a displacive wave amplitude of 1/3<112>, Figures 2-2 and 2-5, while the later forms during aging based on a nucleation and growth event [1]. The displacively formed particles are small, 10-15 Ångstrom, and are visible in selected area diffraction patterns as diffuse streaking [2], while the chemically altered, larger, isothermal ω particles exhibit sharp diffraction spots [1].

However, De Fontaine, while summarizing the ω phase transformation in his 1988 overview article, showed that there is no thermodynamic basis for separating these events [3]. He also pointed out that isothermal ω is based on the rejection of solute content, which would no longer allow a reversible transformation of these altered ω particles to the bcc parent phase. The focus of his model was on the displacive, ideal ω formation based on infinitely fast cooling from the single phase bcc field. During cooling, he proposed an ω start temperature, below which the ω phase would start to form. Due to the fast cooling, only ideal ω would form having coherency strains associated with the small coherent ω particles. Strain fields, either due to ω precipitates or point defects would also enhance local relative stability of the ω structure.

These conclusions were based on a previous investigation [2] where direct evidence for the reversibility of the initial displacively formed ω particles was presented using a cold stage equipped transmission electron microscope (TEM) conducting cooling and heating experiments in various Ti-Mo and Ti-Fe alloys. For example, in Ti-15Mo, it was determined that the ω start temperature, when the first ω particles start to form on quenching, was approximately 500˚C. After fast cooling to room temperature, diffuse streaking in the selected area diffraction pattern (SAD) was present. Further ω formation was observed upon cooling below room temperature. SAD patterns recorded at -4˚C, -19˚C, and -171˚C showed a continuous increase in intensity of the diffuse streaking in the SAD pattern[2]. Reheating the alloy resulted in a gradual decrease in the intensity of the diffuse streaking ω reflections. Subsequent cooling and reheating cycles also showed the reproducibility of the reversibility of this transformation. This reversible character of the displacive formed ω phase was moreover proposed by Ho et al. [4] to explain the anomalous, temperature dependency of the electrical resistivity in Ti-Mo alloys. Similar results were obtained by Quan et al. [5] using Mossbauer and resistivity measurements coupled with XRD investigation for a Ti-9.62Fe alloy at subzero temperatures.

Furthermore, De Fontaine [3] explained that the displacive β to ω transformation can proceed whenever the bulk free energy difference between these two states is

[2] This observation exhibited some parallels to the diffusionless martensitic transformation, martensite initially forming when the martensite start temperature is reached, increasing undercooling resulting in continuing platelet formation as the martensite finish temperature is approached.

negative and proposed that this decrease in free energy is both temperature and solute content dependent. The solute dependency was shown by Sukedai et al. [6] using in situ TEM studies on Ti-Mo alloys with a Mo content of 10, 15 and 20 wt%. In-situ cooling experiments utilizing dark field imaging techniques showed that an increasing number and size of ω particles will be observed with decreasing temperature as well as a decreasing amount and size with increasing solute content.

All the aforementioned results were based on very thin, millimeter or less thick samples, which would follow De Fontaine's infinitesimal fast cooling rates model and the formation of ideal ω. Boeckels et al. [7] have proposed that the ω phase formation can be impacted by the cooling rate from the single phase field in Ti-6.8Mo-4.5Fe-1.5Al using a modified Jominy end-quench test. Only the first 2 mm of the end quench test were cooled with the fastest cooling rate, 526˚C/s after water quenching. The fastest and an intermediate cooling rate, 34˚C/s, where no α precipitation was observed in TEM, were used to investigate the effect of cooling rate on the ω structure. Their findings are summarized in Figure 5-1. When the alloy is quenched quickly from the single phase field, so that no chemical alteration due to short range diffusion (SRD) is permitted, only displacive, reversible ω can form, as projected by De Fontain's model, and visible by the diffuse streaking in the SAD pattern in Figure 5-2(a). On the other hand, as the cooling rate is slowed so that the residence times at elevated temperatures are long enough to permit short range diffusion (SRD), the chemical composition of displacively formed ω particles will alter with increasing undercooling. This sequence

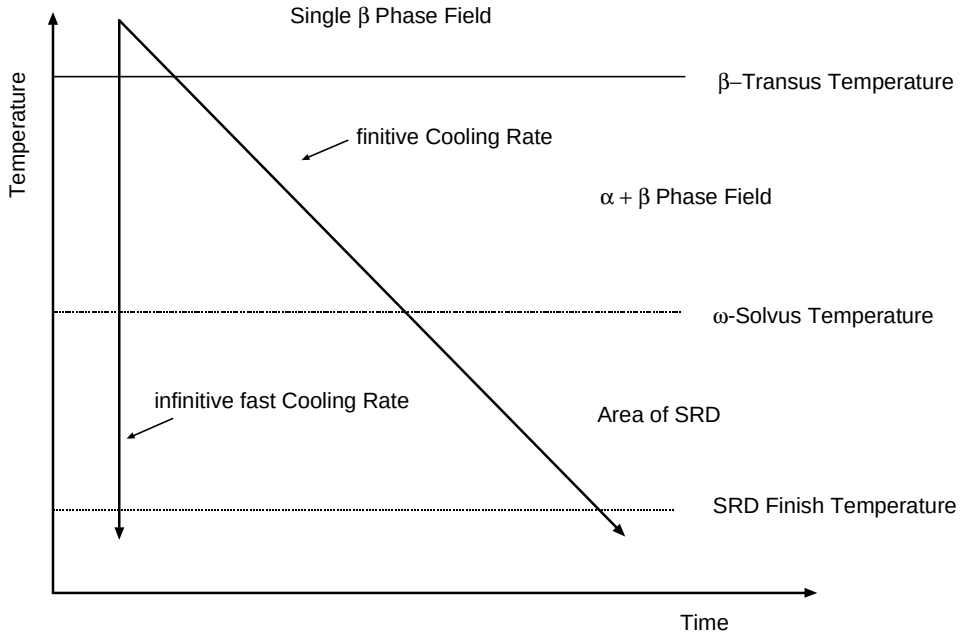

Figure 5-1: Schematic of the comparison between cooling rates from the single phase field, fast undercooling does not permit time for short range diffusion (SRD), but at slower cooling rates, SRD is permitted.

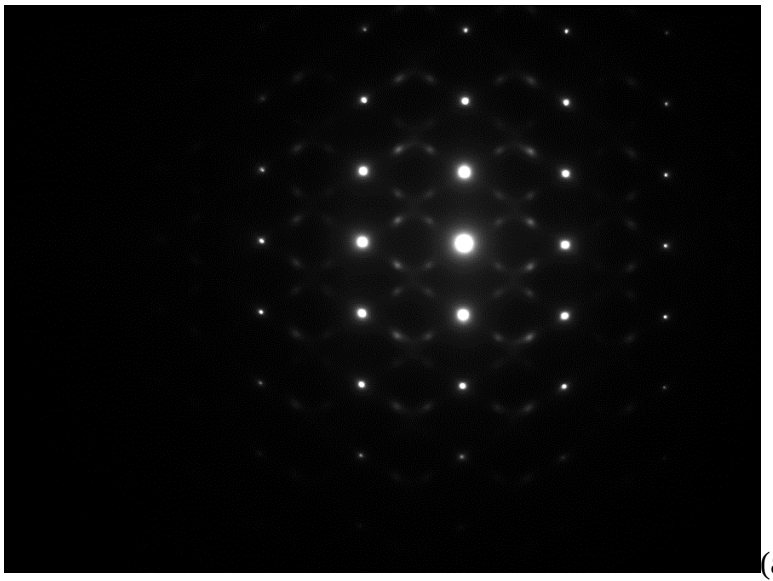
(a)

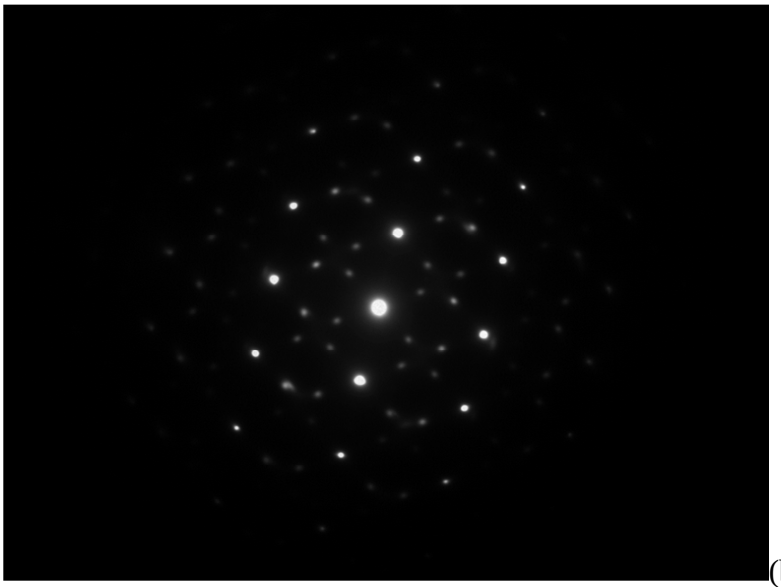
(b)

Figure 5-2: SAD pattern along the [110] zone axis of Ti-6.8Mo-4.5Fe-1.5Al, cooled at 526˚C/s (water quenched) (a) and 34˚C/s (b).

will progress until a temperature is reached below which SRD is no longer permitted, the SRD finish temperature. Evidence for the change to chemically altered ω is presented in the SAD pattern, Figure 5-2 b, which consists of distinct diffraction spots, after intermediate cooling. Below the SRD finish temperature, ω particles can again only form displacively without altering their composition, which was in agreement with the model by De Fontaine.

Interstitial additions are also expected to impact ω formation. For examples, Quan et al. [5] observed in their studies of Ti-9.62Fe, that less ω phase formed on sub-cooling from room temperature when the oxygen content was increased from 0.1wt% to 0.12wt%. Similar observations have been made by Paton and Williams [8] in Ti-V-O alloys, where the increase in oxygen from 0.02 to 0.18 wt.% in Ti-(17-19)wt.%V alloys suppressed the ω start temperature below room temperature. Moreover Kim et al. [9] suggested their observed decrease in Young's modulus was due to a decrease in ω volume fraction, when they increased the oxygen content in Ti-26wt%Nb to 1.2wt%.

The present investigation has shown clear evidence that the oxygen atoms preferably sit in the tetrahedral lattice sites in the bcc crystal using water quenched Ti-15Mo single crystals with oxygen contents of 0.15, 0.5 and 1wt%, Figure 4-45 - 4-47. This location is expected to directly interfere with the collapse along the $<111>_{\beta}$ direction thereby suppressing the displacive, reversible ω formation, and decreasing its volume fraction with increasing oxygen content.

(a)

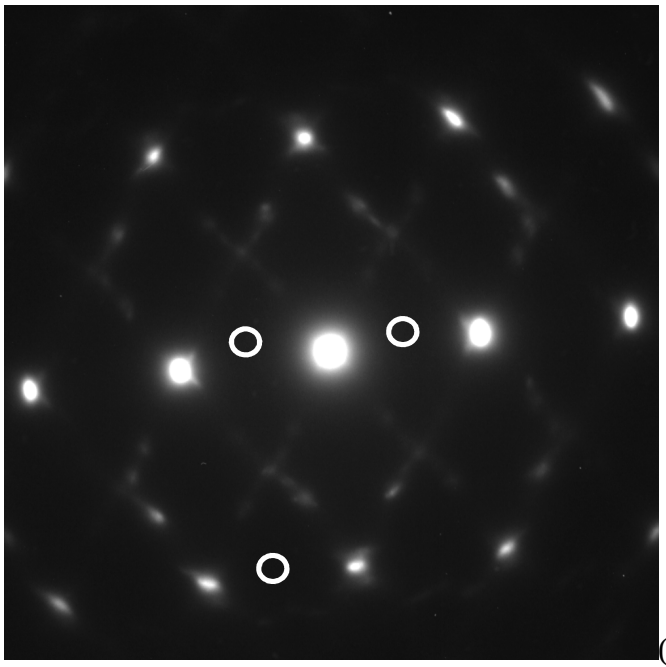

(b)

Figure 5-3: TEM image of Ti-15Mo-2O after aged for 4 hours at 450˚C (a) heated at 5CPM. The fine needles shape particles are α precipitations, marked with circles. α spots are marked in (b).

The present study has however shown that the addition of 2wt% oxygen to Ti-15Mo is ineffective in suppressing displacive, reversible ω formation, Figure 5-3 a. Comparison with studies of Ti-Nb-O and Ti-V-O system suggests that the potency of oxygen in suppressing the displacive ω formation is dependent upon the solute-interstitial binding energy. Internal friction results show that in Ti-Nb-O [10] and Ti-V-O [11], the bonding energy between titanium and oxygen atoms were stronger than that between the solute atoms and oxygen. The results of this investigation for the Ti-Mo-O system suggest that the bonding energy between Mo and O atoms exceeds that between Ti and O, assuming that Mo atoms reside within the titanium matrix in preferred sites within a supercell lattice, these sites be associated with local oxygen clustering. This would also lead to an oxygen fluctuation within the matrix. There will be areas in which the O clustered is clustered and is associated with the Mo and where reversible ω formation is suppressed. In other areas in which the O concentration is lower, either due to local depletion of Mo or a decreased O concentration, reversible ω formation will occur. Future high resolution TEM will be required to substantiate these suggestions.

Finally continuous β phase decomposition during heating was investigated by Prima et al. [12-18] using resistivity and dilatometry combined with high resolution TEM and neutron diffraction techniques. Their investigation of the temperature dependency on the temperature coefficient of resistivity (TCR) in Ti-6.8Mo-4.5Al-1.5Fe demonstrated the reversibility of reversible ω during heating. The displacive, reversible ω transformation to the parent bcc phase, occurred between 150 and 200˚C

[12, 14]. Further heating, using 2/3/5CPM resulted in coarsening of irreversible ω phase following a $t^{2/3}$ law for the early stages of growth [16]. During further heating the irreversible ω coarsens and ultimately dissolves. The rates for these reactions depend upon the initial ω size and compositional distribution as established by their previous cooling history. These phenomena should be controlled by the solute atom diffusion [16]. Indeed, these findings were confirmed by Boeckels and Rack in Ti-6.8Mo-4.5Fe-1.5Al using isochronal and isothermal DSC experiments combined with TEM techniques [19, 20]. At a heating rate of 5 CPM, the reversible ω transformation was detected by an initial change of slope between 122 and 225˚C in the heat flow curve, A1 in Figure 5-4. A further increase in slope was associated with the coarsening of irreversible ω up to approximately 300˚C, A2 in Figure 5-4, the initial rise in the heat flow which resulted in a maximum at 350˚C was associated with secondary α precipitation occurring. Finally, above 350˚C ω dissolution observed combined with continued α phase formation and growth was observed.

Corrected isochronal heating results for the β solution treated Ti-15Mo-(0.12-2)O, Figures 4-16 through 4-31, indicate that multiple reactions are observed. Figure 5-5 summarizes the influence of oxygen on the maximum reaction temperatures observed during the isochronal trials. The first observed reaction as defined by R1, solid symbols, is associated with the reverse transformation of ω to the bcc parent phase. The reaction temperature was approximately at 210˚C for the lower oxygen containing alloys, up to 0.35wt% oxygen. A further increase in oxygen content to 0.5wt% resulted in a decrease

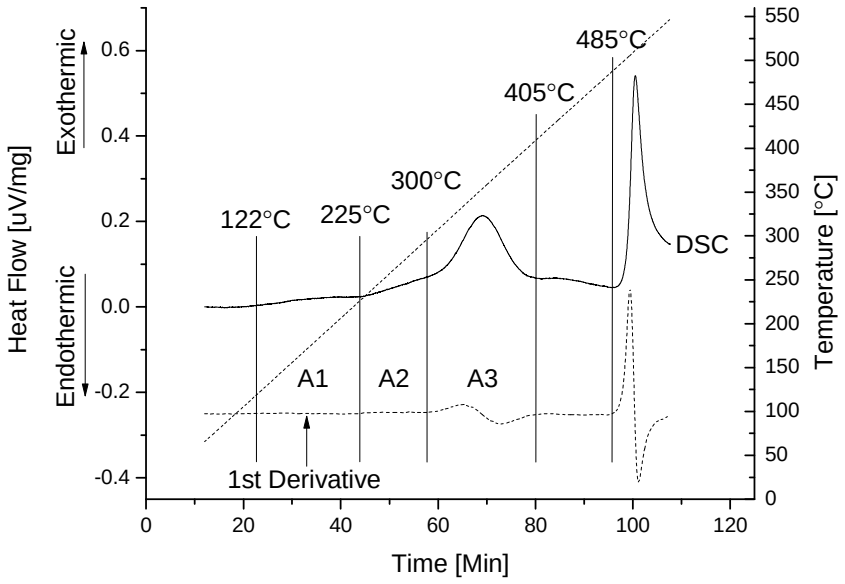

Figure 5-4: Baseline corrected isochronal heat flow of Ti-6.8Mo-4.5Fe-1.5Al heated at 5CPM.

of R1 to 150°C. Additionally, another peak at 210°C was observed, marked by the unfilled symbol. The presence of these two peaks reinforces the prior suggestion that local variations in O content will cause local reversible ω suppression thereby resulting in a decrease in the reverse ω to bcc transformation. Oxygen depleted areas are expected still exhibit the same ω to bcc transition temperature as lower oxygen conditions, i.e. 210°C, unfilled marker for Ti-15Mo-0.5O. Increasing the O concentration further would also be expected to increase the number of oxygen enriched areas and thereby to further decrease the ω to bcc transition temperature. This can be seen for Ti-15Mo-2O in Figure 5-5. The R1 reaction, the solid marker, decreased to 90°C. R2 may be associated with the coarsening of the irreversible ω phase during heating. This reaction is not influenced by the oxygen content for up to 0.5wt%. At the highest oxygen content decreased the reaction peak temperature to 230°C, solid up triangle symbol in Figure 5-5. Oxygen can also effect the size and volume fraction of the irreversible ω in two ways, first by suppressing the formation of reversible ω, thereby decreasing the volume fraction of irreversible ω formed from reversible ω and secondly by suppressing the growth of the ω phase which would hinder coarsening. Similar observations were made by Qazi et al. [21-23] in Ti-35Nb-7Zr-5Ta-(0.06-0.68)O using TEM imaging techniques. R3 and R4 being discussed in the α section.

Figure 5-6 summarizes the reaction temperature results for the α + β processed Ti-15Mo-(0.15-0.5)O. Comparison with the observations for β processed material

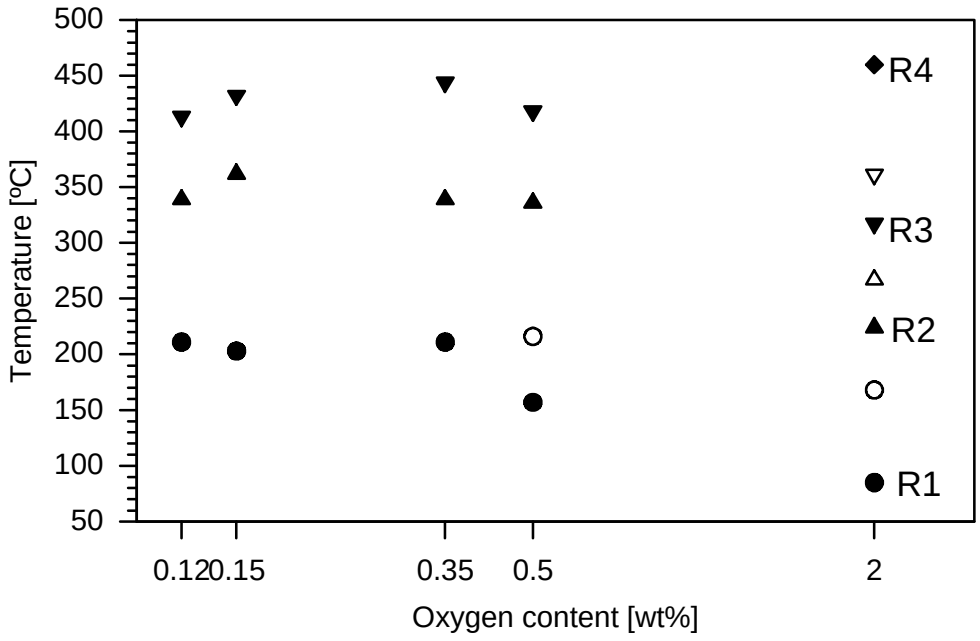

Figure 5-5: Isochronal peak reaction temperature during isochronal heating of β processed Ti-15Mo-(0.12-2)O at 5CPM.

indicates that those shown in this figure are generally lower. In addition only a simple reversible to β transformation temperature has been observed, independent of O content. Further this reaction temperature is only weakly influenced by macroscopic O content. These results can be understood recognizing that during the α-β processing, at 732-760°C, partitioning of O to the α phase occurs. Under equilibrium conditions, Pandat thermodynamic calculations confirm this partitioning, the O content in the α phase increasing to 0.91wt% at a macroscopic 0.15wt% O and to 2.4wt% at a macroscopic O content of 0.5wt%, the oxygen level in the β phase remaining between 0.13 and 0.19wt%. The similar response of R2, this reaction being associated with coarsening of irreversible ω, also supports this suggestion. Further x-ray measurements of the ω particle size also indicated only a weak dependence on oxygen content, Figures 4-6 through 4-8. The evolution of the irreversible ω particles size with low aging temperature can moreover be defined as shown in Figure 5-7 for in α + β processed Ti-15Mo-(0.15-0.5)O. For early times at 400°C and 450°C the ω particle size increased independent of the oxygen content, region a. This reaction was also observed during isothermal thermal analysis. JMAK analysis of the latter, summarized in Appendix B, indicates that the Avramni coefficient, n, equals 1, which can be associated with three dimensional growth of the ellipsoidal ω particles [25].

After a certain ω size is reached, region b in Figure 5-8, no future growth was observed, a size plateau being reached. Langmayr et al. [26, 27] have previously observed a similar phenomena in small angel scattering x-ray studies of aging in Ti-

18wt%Mo and Ti-32wt%Mo, Figure 5-8. Paris et al. [28] in their previous study of γ' precipitation in γ Ni based alloys suggested that this behavior could be understood by correlating the anisotropic elastic strains within the matrix, the misfit strains and the elastic inhomogeneity associated with matrix incorporations (solute content). Utilizing the Eshelby approach [29] they suggest the presence of elastic strains surrounding the precipitated particles will result in a decrease in particle growth and coarsening. Further ramification will recognize measurement of these strains utilizing HRTEM.

Langmayr et al. also suggested that the subsequent increase in ω size, regime c in Figure 5-8, observed at longer aging times occurs concurrent with the precipitation of α, the latter being to relieve the localized interfacial strains. Support for this provided by the HRSEM micrograph, Figure 5-9, where coarsened ω and fine α is observed in α + β processed Ti-15Mo-0.15O aged for 256 hours at 400°C. Further measurement of the ω and α volume fraction, Figure 5-7a, indicates that the proportion of ω decreases and that α increases at times beyond the plateau region (c) shown in Figure 5-7.Finally in region d dissolution of ω is predominant. This dissolution is however directional, that is dissolution in direction normal to (2-11) progresses at a more rapid rate than normal to (301). Two possibilities for this observation include anisotropy of diffusion or a non-uniformity (directionally) in previously existing residual strain field.

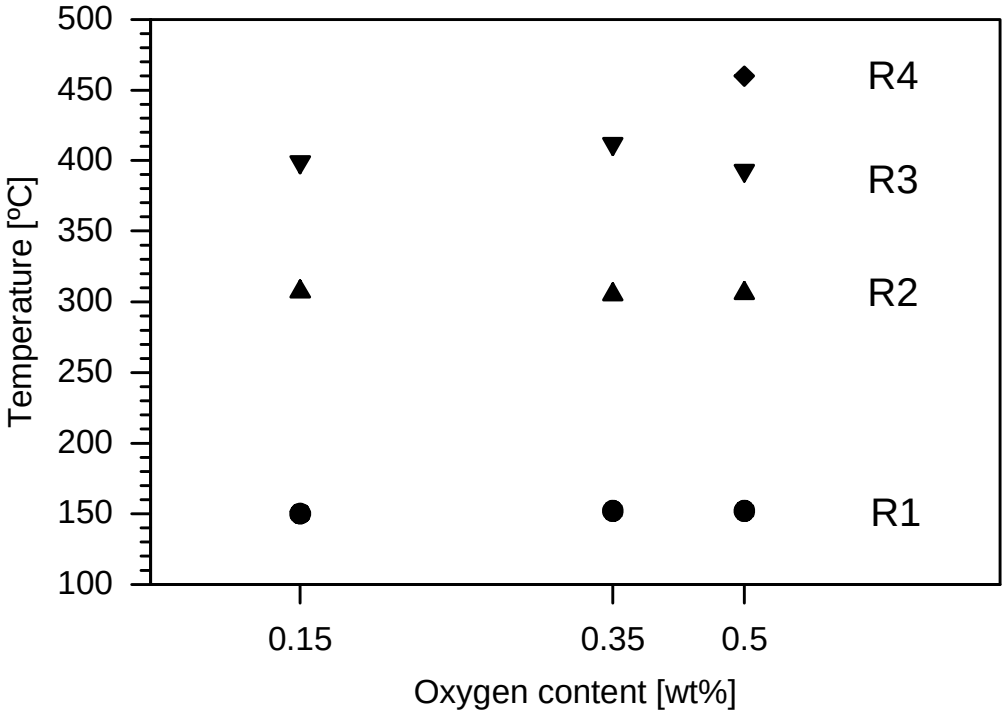

Figure 5-6: Isochronal peak reaction temperature during isochronal heating at 30CPM of α + β processed Ti-15Mo-(0.15-0.5)O.

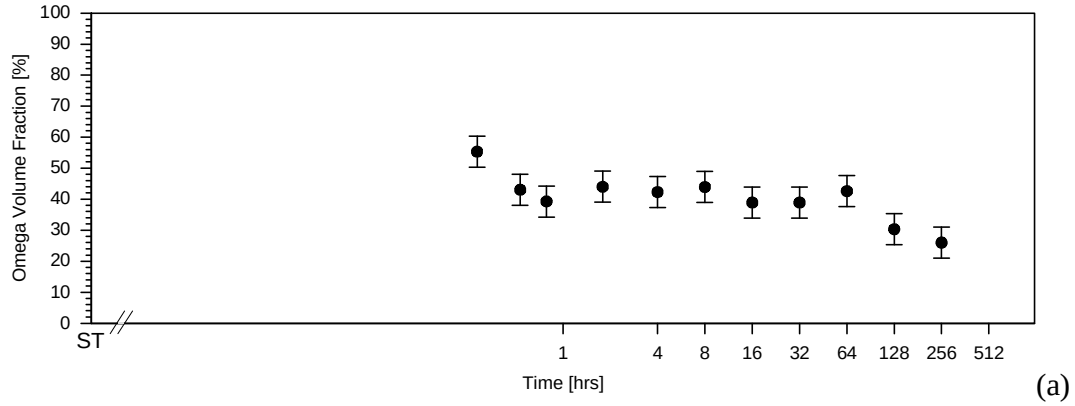

(a)

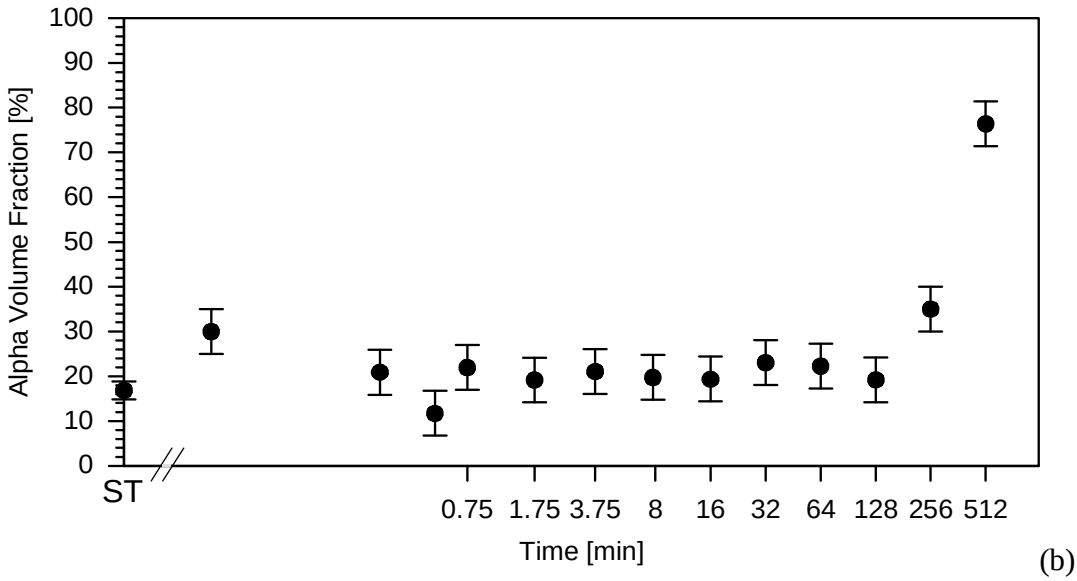

(b)

Figure 5-7: Evolution (a) of the ω, (b) α volume fraction for α + β processed Ti-15Mo-0.5O during aging at 400˚C determined by x-ray diffraction based on all available diffraction lines to reduce statistical errors, grain size or texture effects derived by a method introduced by Giamei and Freis [24].

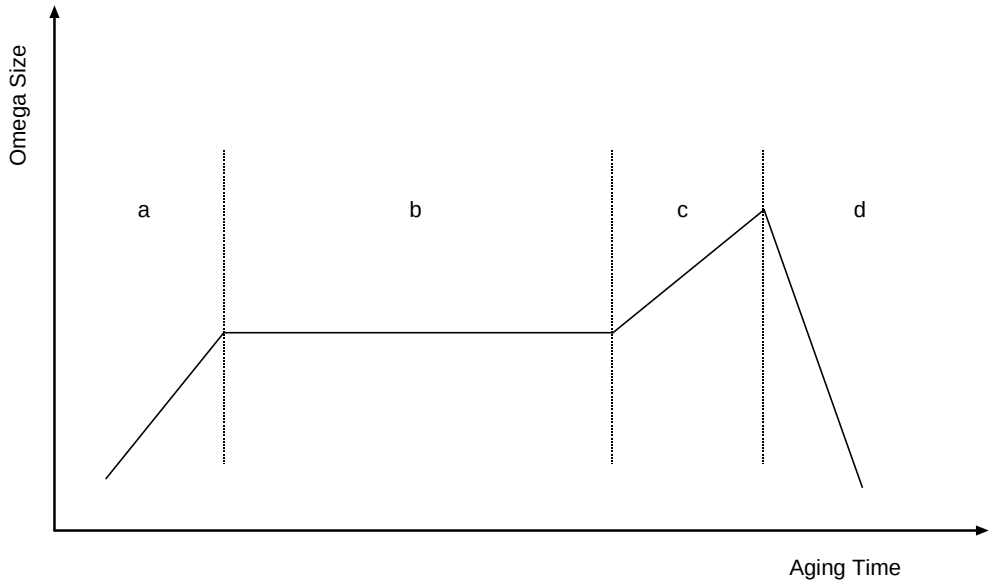

Figure 5-8: ω evolution during low temperature aging of α + β processed Ti-15Mo-(0.15-0.5)O: a. growth on the ω phase from the quenched condition, b stabilization of the ω phase, c further growth of the ω phase and d Dissolution of the ω phase.

5.2. α phase

As previously discussed, the low temperature reactions in α + β processed Ti-15Mo, Figure 5-6, arise from the ω transformations displayed in this alloy system. HRSEM further indicates that the isochronal reaction, R3 as well as the secondary isothermal reaction observed at 400°C , P2, can be associated with the formation of a continuous grain boundary α film, Figure 5-9, 5-10 and 5-11. Finally, R4 which was only observed at the highest oxygen level examined in α + β processed Ti-15Mo could be associated with the formation of intragranular α, Figure 5-3.

The elevated temperature thermal analysis results of β processed Ti-15Mo are similar to the α + β processed material. The increase in R3 observed can be ascribed to the need to overcome the grain boundary nucleation energy, only growth of grain boundary α from pre-existing triple point primary α being previously observed in the α + β processed Ti-15Mo. The duplex nature of grain boundary α formation in β processed Ti-15Mo-2O follows the prior study of Qazi and Rack [21-23] who showed that the degree of oxygen partitions to the β grain boundaries depends on the grain boundary misorientation.

Several changes in the grain boundary and primary morphology were also observed, Figure 5-10. At low temperature, e.g. 400°C and long aging time sideway growth of α from both the grain boundary and primary α were observed, Figure 5-14 a. Increasing aging times results in thickening of the sideways α plates accompanied by

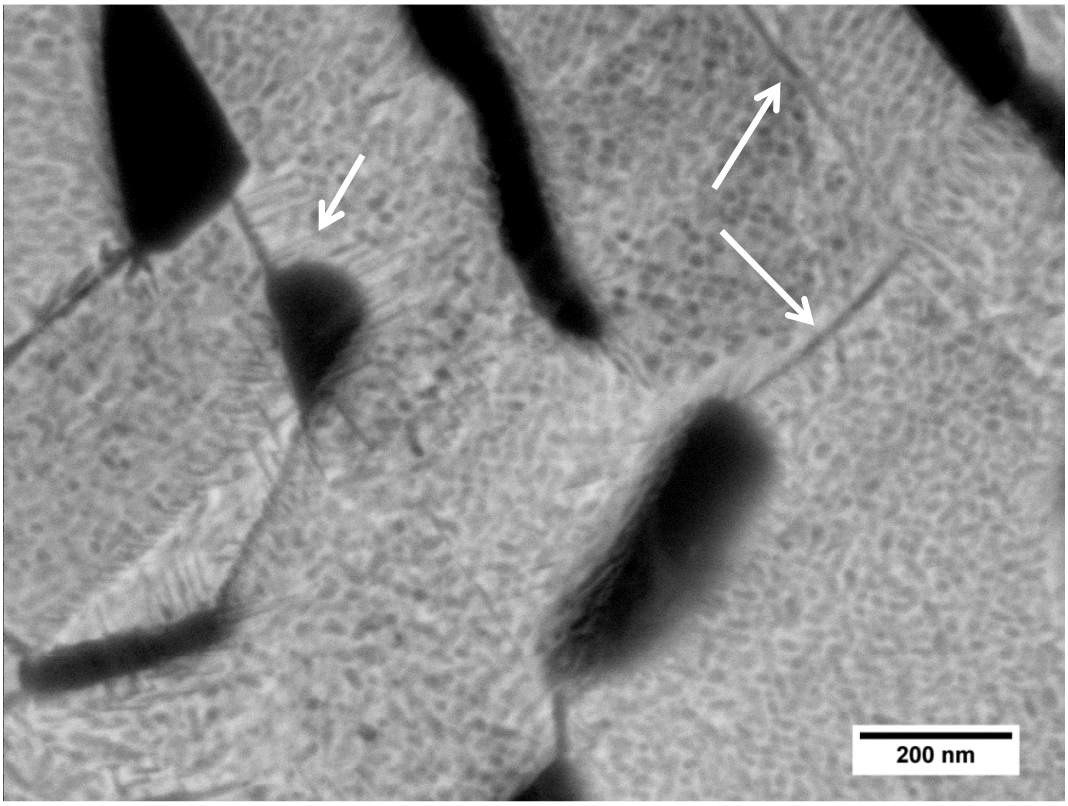

Figure 5-9: Ti-15Mo-0.15O aged at 400°C for 256 hours (SEM backscatter image); the arrows show a) grain boundary α film and b) sideway growth of α platelets from the grain boundary into matrix.

partitioning of Mo to the residual β phase, the latter ultimately being encapsulated in the precipitate α particles, Figure 5-14 b.

The hardness response parallels this evolution and is dependent upon the ω and α phase evolution. The initial hardness increase is due to the growth of ω. The hardness plateau is based on stabilized ω size and fine α precipitation. The overaging hardness response is due to continuous secondary α formation and growth combined with ω coarsening and dissolution. Hardness increases with increasing interstitial content as a result of solid solution strengthening and α particle refinement.

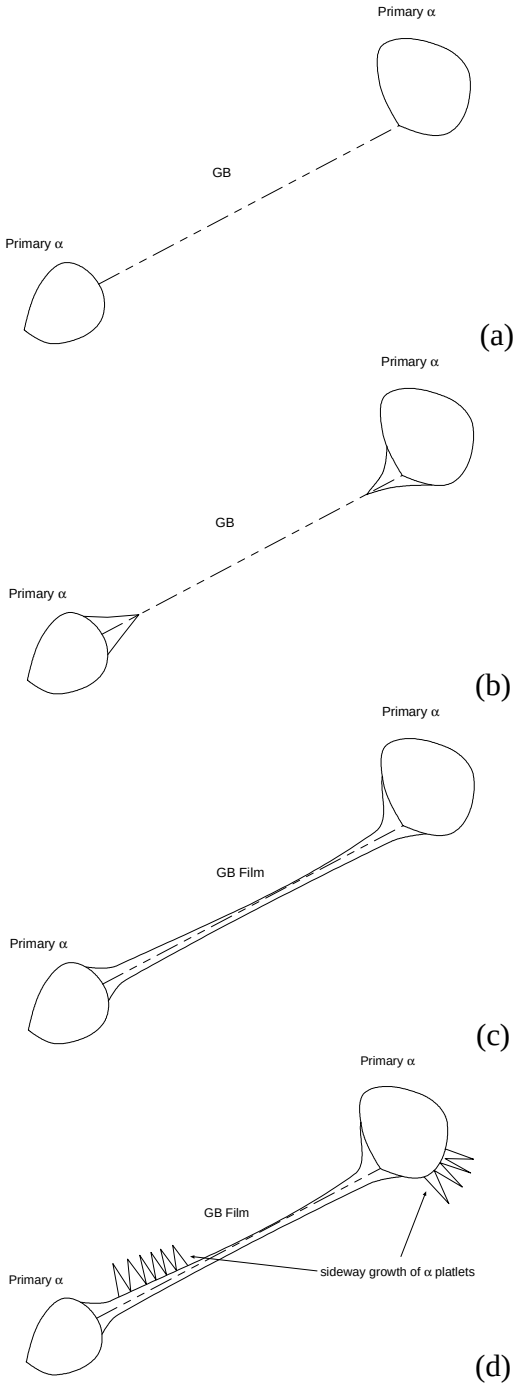

Figure 5-10: Grain boundary α evolution in α+β processed Ti-15Mo alloys during low temperature aging: (a) initial primary α particles at grain boundary triple points (b) initial growth along grain boundary, (c) grain boundary film formation, (d) sideway growth of α platelets.

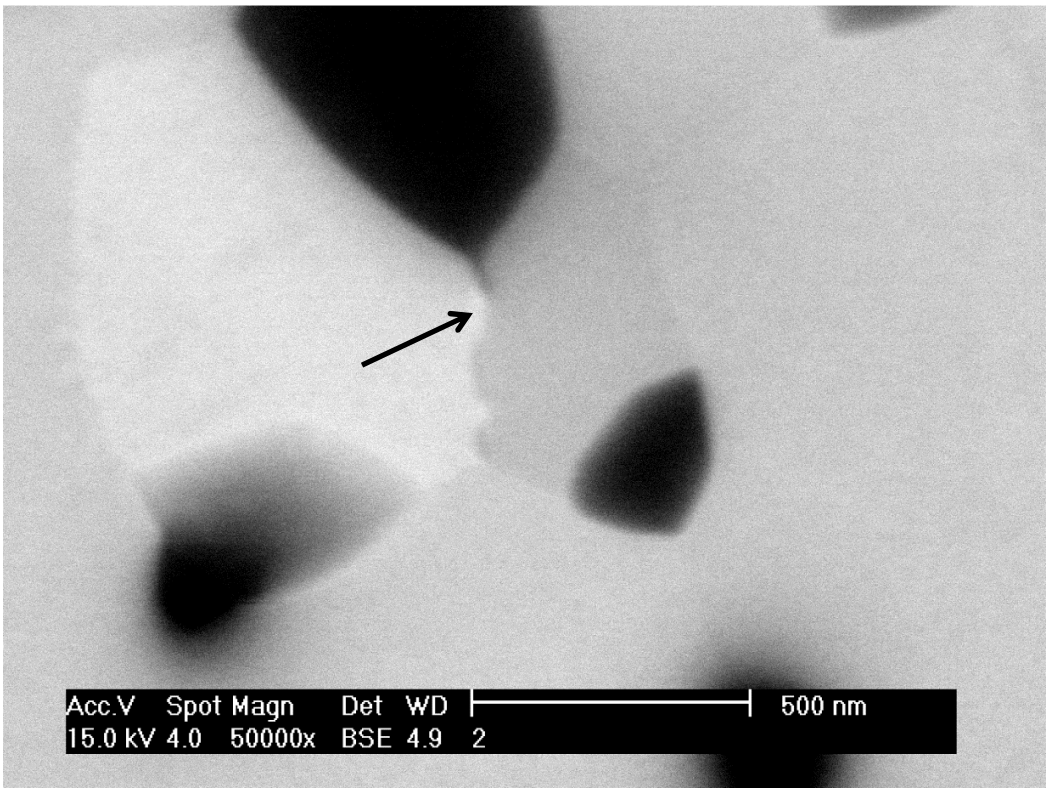

Figure 5-11: Grain boundary α (arrow) formation in α+β processed Ti-15Mo-0.15O α + β processed aged at 400˚C for 8 hours.

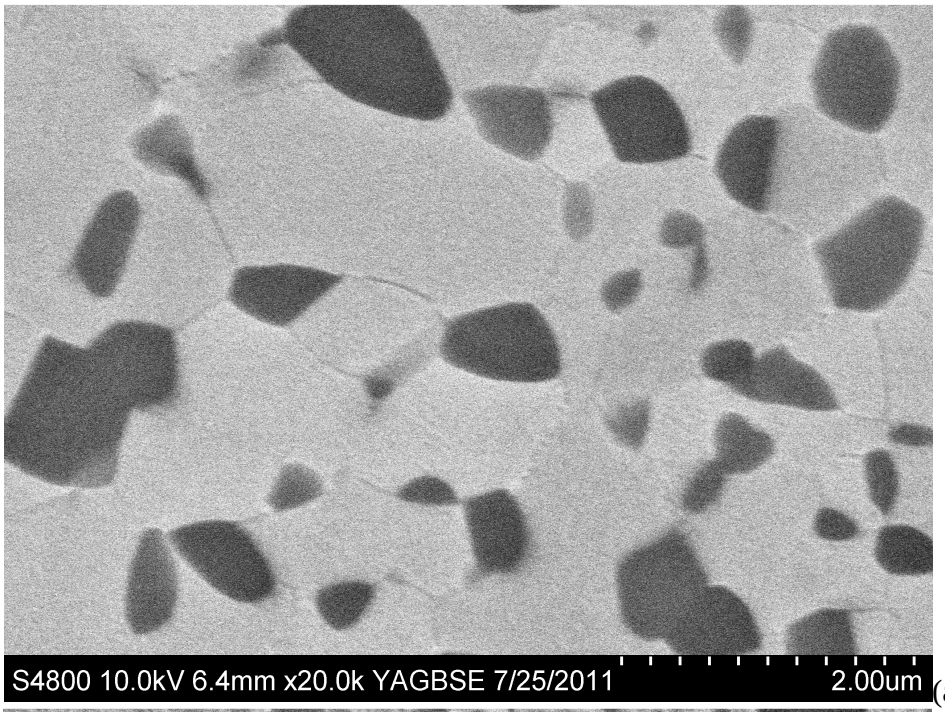

(a)

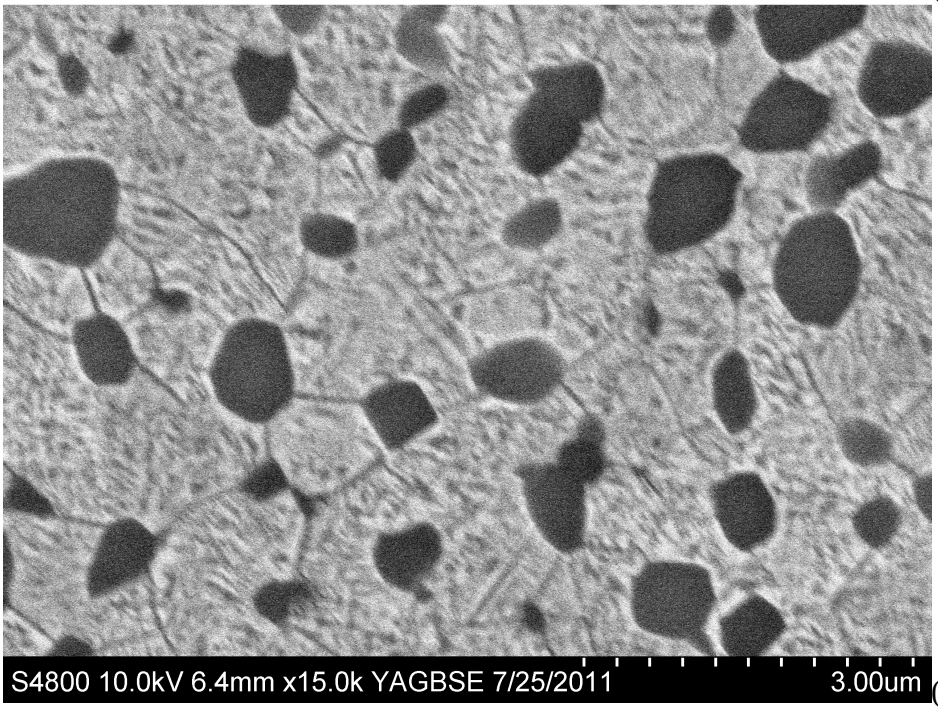

(b)

Figure 5-12: α+β processed Ti-15Mo-0.5O aged at 450°C for (a) 16 hours and (b) 256 hours (SEM backscatter image).

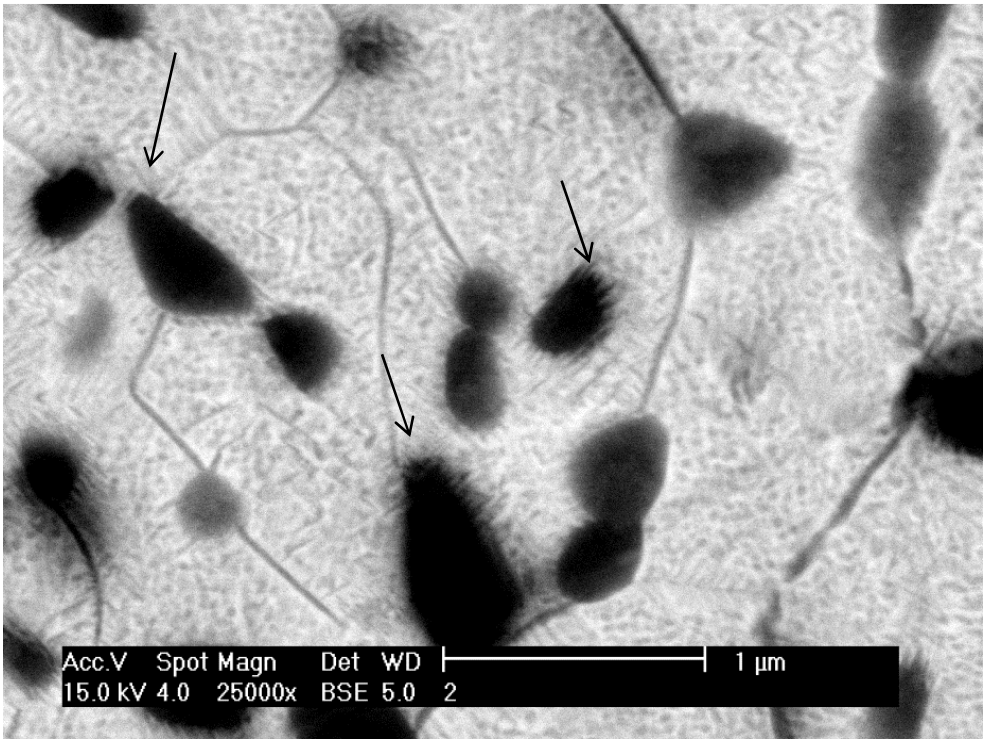

Figure 5-13: Ti-15Mo-0.5O aged at 400˚C for 256 hours, epitaxial growth of α platelets from the grain boundary α.

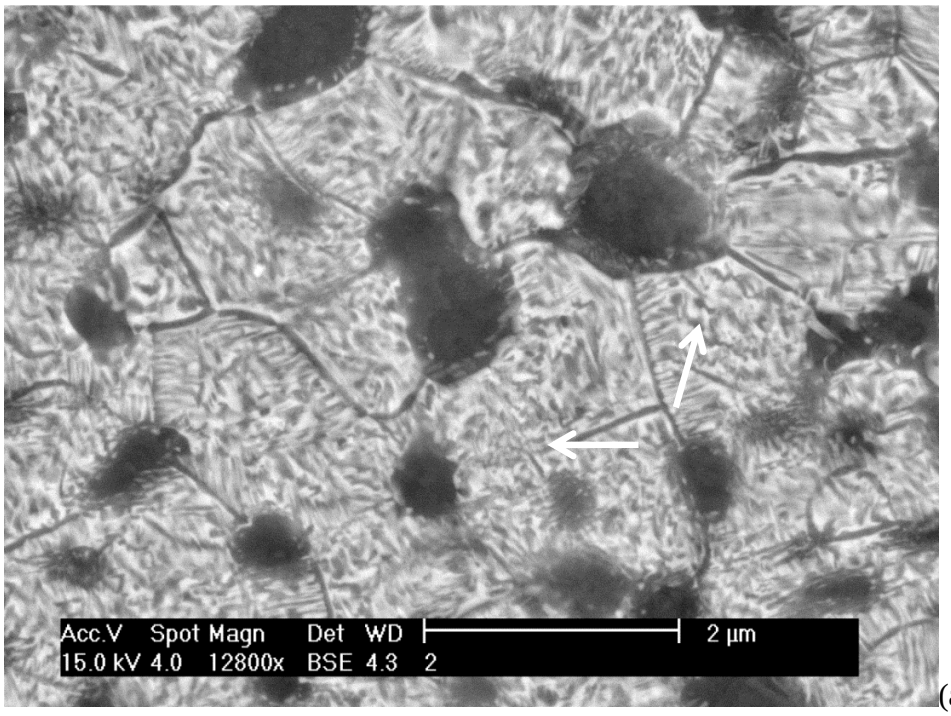

(a)

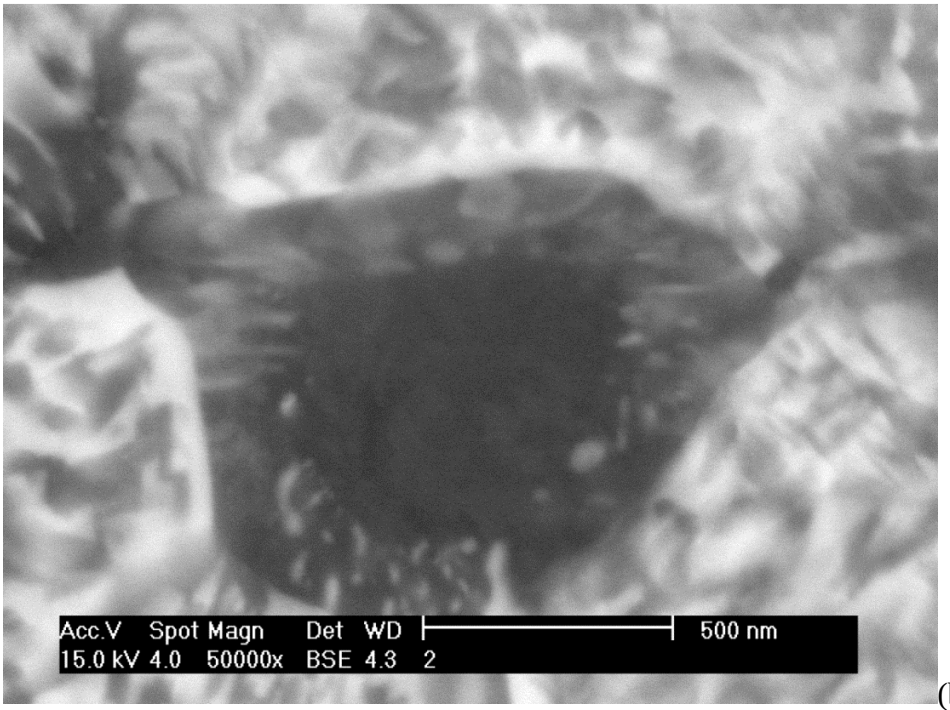

(b)

Figure 5-14: Ti-15Mo-0.15O aged at 400˚C for 512 hours, sideway α and encapsulation of β particles (arrows), (b) higher magnification.

5.3. References

[1] S. Bannerjee and P. Mukhopadhyay, “Phase Transformations – Examples from Titanium and Zirconium Alloys”, Pergamon, Oxford, (2007), pp. 490-518

[2] S.L. Sass, “The Structure and Decomposition of Zr and Ti B.C.C. Solid Solutions”, Journal of Less-Common Metals, No. 28, (1972), pp. 157-172

[3] D. De Fontaine, N.E. Paton and J.C. Williams, “The Ω Phase Transformation in Titanium Alloys as an Example of Displacement Controlled Reactions”, Acta Metallurgical, Vol. 19, (1971), pp. 1153-1162

[4] J.C. Ho and E.W. Collings, “Anomalous Electrical Resistivity in Titanium-Molybdenum Alloys”, Physical Review B, Vol 6, No. 10, (1972), pp. 3727-3737

[5] Z. Quan, R. Ma, J. Ping and R. Chang, “The precursor effect of the athermal β to ω transformation in Ti-9.62Fe alloy”, Acta Metallurgical, Vol. 36, No. 11, (1988), pp. 2989-2994

[6] E. Sukedai, H. Matsumoto and H. Hahimoto, “Electron microscope study on Mo content dependence of β to ω phase transformation due to cooling in Ti-Mo alloys”, Journal of Electron Microscopy, Vol. 51, (2002), pp. S143-S147

[7] H. Boeckels, R.E.A. Williams, H.L. Fraser and H.J. Rack, “Athermal –Isothermal Phase Transformations in Ti-6.8Mo-4.5Fe-1.5Al”, presented at the MS&T meeting 2012 in Pittsburgh

[8] N.E. Paton and J.C. Williams, ”THE INFLUENCE OF OXYGEN CONTENT ON THE ATHERMAL β-ω TRANSFORMATION”, Scipta Metallurgica, Vol. 7, (1973), p. 647

[9] W. Kim and H. Kim, “Effect of Oxygen on Elastic Modulus and Mechanical Property of Metastable TiNbO Based Alloys”, Key Engineering Materials, Volume 343-343, 2007: p. 549

[10] Terlize Cristina Niemeyer , Carlos Roberto Grandini a, *Odila Florˆencio*, “Stress-induced ordering due heavy interstitial atoms in Nb–0.3 wt.% Ti alloys”, Materials Science and Engineering A 396 (2005), p. 285

[11] O. Buck, D.O. Thompson, N.E. Paton and J.C. Williams, “The relation between internal friction spectra and the athermal β to ω transformation in Ti-V, Ti-V-O and Ti-

V-H alloys", Proceedings of the 5th International Conference on Internal Frcition and Ultrasonic Attenuation in Crystalline Solids, (1975), pp. 451-458

[12] F. Prima, P. Vermaut, D. Ansel, M. Boliveau, H. Francillette and J. Debuigne: "Phase Transformations in Ti-6.8Mo-4.5Fe-1.5Al", in Titanium'99: Proceedings of the 9th World Conference on Titanium, St. Petersburg, Russia, (1999), pp. 107-114

[13] F. Prima, J. Debuigne, M. Boliveau and D. Ansel, "Control of ω phase volume fraction precipitation in a β titanium alloy: Development of an experimental method", Journal of Material Science Letters, Vol. 19, (2000), pp. 2219-2221

[14] F. Prima, P. Vermaut, D. Ansel and J. Debuigne, "ω Precipitation in a B Metastable Titanium Alloy, Resistometric Study", Mater. Trans. , JIM, Vol. 41, No 8, (2000), pp. 1092-1097

[15] F. Prima, P. Vermaut, T. Gloriant, J. Debuigne and D. Ansel, "Experimetal evidence of elastic interaction between ω nanoparticles embedded in a metastable β titanium alloy", Journal of Material Science Letters, Vol. 21, (2002), pp. 1935-1937

[16] J. Debuigne and F. Prima, "Growth Kinetic Model for Isothermal Ω Phase Particles in Low-Cost B Titanium Ti-6.8Mo-4.5Fe-1.5Al", Mater. Trans., JIM, Vol. 46, No. 6, (2005), pp. 1433-1435

[17] Prima F, Vermaut P, Texier G, Ansel D, Gloriant T., "Evidence of α-nanophase heterogeneous nucleation from ω particlesbin a β-metastable Ti-based alloy by high-resolution electron microscopy" Scripta Materialia, Vol. 54, (2006), pp. 645-648

[18] T. Gloriant, G. Texier, F. Sun, I. Thibon, F. Prima and J.L. Soubeyroux, "Characterization of nanophase precipitation in a metastable β titanium-based alloy by electrical resistivity, dilatometry and neutron diffraction", Cripta Materialai, Vol. 58, (2008), pp. 271-274

[19] H. Boeckels and H.J. Rack, "Effect of Heating Rate on the short Time Aging Kinetics of Ti-6.8Mo-4.5Al-1.5Fe", presented at the TMS Spring Meeting 2012 in Orlando

[20] T. Cain, H. Bockels and H.J. Rack, "Aging Kinetics of Ti-6.8Mo-4.5Fe-1.5Al", presents at the NATAS Conference in Orlando, Fl., August 2012

[21] J.I. Qazi, V. Tsakiris, B. Marquardt and H. J. Rack, "The effect of duplex aging on the tensile behavior of Ti-35Nb-7Zr-5Ta-(0.06-0.7)O alloys", Ti-2003: Science and Technology, G. Luertjering and J. Albrecht, eds., Wiley-VCH Verlag Gmbh, Weinheim, Germany, pp.1651-1658.

[22] J. I. Qazi, B. Marquardt, L. Allard and H. J. Rack, “Phase transformations in Ti-35Nb-7Zr-5Ta(0.06-0.7)O alloys”, Material Sci. & Eng., Vol. C25 389(2005).

[23] J. I. Qazi, V. Tsakris, B. Marquardt and H. J. Rack, “Effect of aging treatments on the tensile properties of Ti-35Nb-7Zr-5Ta(0.06-0.7)O alloys”, Jn ASTM(JAI),Vol. 2, #8,19(2005).

[24] Giamei A.F., Freise E.J., Trans. AIME, 1967, Vol. 239, pp. 1676-85

[25] J. W. Christian, The Theory of Transformation in Metals and Alloys (2nd ed.), Elsevier, Oxford (2002) 529

[26] F. Langmayr, P. Fratzl and G. Vogl, “Crossover from ω-phase to α-phase precipitation in bcc Ti-Mo”, Physical Review B, Vol. 49, No. 17, (1994), pp. 11759-11766

[27] P. Fratzl, F. Langmayr, G. Vogl and W. Miekeley, “THE GROWTH OF ω-PHASE INCLUSIONS IN Ti-20 at% Mo AND THE COMPOSITION BETWEEN ELASTIC AND SURFACE ENERGIES”, Acta Metall., Vol. 39, No. 5, (1991), pp. 753-761

[28] O. Paris, F. Langmayr, G. Vogl, and P. Fratzl, “A Possible Criterion for Slowing Down of Precipitate Coarsening due to Elastic Misfit Interactions”, Z. Metallkd. Vol. 86, (1995), pp. 860-863.

[29] J.D. Eshelby, Prog. Solid Mech. 2 (1961) 89

CHAPTER SIX

6. CONCLUSIONS

This dissertation has shown:

1. Two types of ω phase can be observed. The reversible ω phase forms displacively on rapid cooling. The irreversible ω is chemically altered reversible ω.

2. Oxygen reduces the displacive transformation.

    a. Oxygen sits within the tetrahedral interstitial bcc lattice sites and directly interferes with the ω transformation. Increasing oxygen content decreases reversible ω volume fraction and size.

    b. Increased bonding energy between Mo-O atoms, vis a vis Ti-O results in oxygen enriched and depleted areas. ω can still form in the oxygen depleted areas

3. The irreversible ω forms during intermediate cooling rates. This chemical alteration is due to short range diffusion. Heating rates have the same effect.

4. Irreversible ω evolves during isothermal aging in four stages: a) growth, b) stabilization, c) coarsening and d) dissolution. The ω size is stabilized due to elastic strains associated with the particles. Coarsening begins when these strains are relieved by α nucleation. Dissolution is accompanied by further growth of the α phase. Increasing temperature and/ or oxygen content accelerates this evolution to shorter size stabilization times and accelerated ω coarsening and α nucleation.

5. At low aging temperatures and long aging times grain boundary and primary α morphologies under changes, these being associated with the growth of sideway α platelets. Further increase in aging times and oxygen causes thickening of the sideway α platelets accompanied by Mo partitioning to the residual β, the latter being encapsulated within the surrounding expanded primary α phase.

6. Oxygen affects the secondary α nucleation.

    a. Up to 0.5 weight percent oxygen promotes homogeneous α formation.

    b. At higher oxygen concentrations, for example 2wt% in Ti-15Mo, oxygen clusters act as preferred heterogeneous α nucleation sites causing earlier α nucleation.

7. The hardness response is based on the evolution of the ω and α phase
    i. Hardness increase due to ω size increase.
    ii. Hardness plateau based on ω size stabilization and initial fine α precipitation.
    iii. Overaging, ω coarsening and dissolution paired with further α growth.

APPENDICES

Appendix A

Pandat Calculations

The Pandat phase diagram calculation software from CompuTherm LLC with the Titanium Database Version 6 was used to determine the phase diagrams for Ti-15Mo-0.15/0.35/0.5/1/2O.

Table A 1: Pandat calculations for Ti-15Mo-0.15O

Phase Name	T[°C]	Volume Fraction (BCC_A2)	Volume Fraction (HCP_A3)	w%(MO@BCC_A2)	w%(O@BCC_A2)	w%(Ti@BCC_A2)	w%(MO@HCP_A3)	w%(O@HCP_A3)	w%(Ti@HCP_A3)
BCC_A2	800	1		15	0.15	84.85			
BCC_A2	785	1		15	0.15	84.85			
BCC_A2	770	1		15	0.15	84.85			
BCC_A2+HCP_A3	762.192	1	0	15	0.15	84.85	0.149049	0.994655	98.8563
BCC_A2+HCP_A3	755	0.972025	0.0279747	15.3883	0.13009	84.4816	0.169961	0.910398	98.9196
BCC_A2+HCP_A3	740	0.909109	0.0908914	16.341	0.0950351	83.564	0.218	0.755898	99.0261
BCC_A2+HCP_A3	725	0.842488	0.157512	17.4887	0.0683867	82.4429	0.267888	0.633114	99.099
BCC_A2+HCP_A3	710	0.775877	0.224123	18.8114	0.0488156	81.1398	0.314813	0.539858	99.1453
BCC_A2+HCP_A3	695	0.712321	0.287679	20.2775	0.0346324	79.6878	0.355796	0.470125	99.1741
BCC_A2+HCP_A3	680	0.653519	0.346481	21.858	0.0243705	78.1177	0.389709	0.417642	99.1926
BCC_A2+HCP_A3	665	0.600061	0.399939	23.5311	0.0169441	76.452	0.416476	0.377454	99.2061
BCC_A2+HCP_A3	650	0.551887	0.448113	25.2818	0.0115883	74.7066	0.436462	0.346051	99.2175
BCC_A2+HCP_A3	635	0.50863	0.49137	27.1	0.00776138	72.8923	0.450169	0.321037	99.2288
BCC_A2+HCP_A3	620	0.469813	0.530187	28.9784	0.00506854	71.0166	0.458115	0.300774	99.2411
BCC_A2+HCP_A3	605	0.434943	0.565057	30.9116	0.00321352	69.0852	0.46081	0.284126	99.2551
BCC_A2+HCP_A3	590	0.40356	0.59644	32.8953	0.00196954	67.1027	0.458746	0.270286	99.271
BCC_A2+HCP_A3	575	0.375256	0.624744	34.9252	0.00116182	65.0736	0.452404	0.258668	99.2889
BCC_A2+HCP_A3	560	0.349671	0.650329	36.9971	0.000656735	63.0023	0.442254	0.248836	99.3089
BCC_A2+HCP_A3	545	0.3265	0.6735	39.1058	0.000354137	60.8939	0.428764	0.240457	99.3308
BCC_A2+HCP_A3	530	0.305478	0.694522	41.2456	0.000181359	58.7542	0.412395	0.233271	99.3543
BCC_A2+HCP_A3	515	0.286382	0.713618	43.4097	8.78E-05	56.5902	0.393602	0.227075	99.3793
BCC_A2+HCP_A3	500	0.269017	0.730983	45.5904	4.00E-05	54.4096	0.372833	0.221705	99.4055

Table A2: Pandat calculations for Ti-15Mo-0.35O

Phase Name	T[°C]	Volume Fraction (BCC_A2)	Volume Fraction (HCP_A3)	w%(MO@BCC_A2)	w%(O@BCC_A2)	w%(Ti@BCC_A2)	w%(MO@HCP_A3)	w%(O@HCP_A3)	w%(Ti@HCP_A3)
BCC_A2	900	1		15	0.35	84.65			
BCC_A2	880	1		15	0.35	84.65			
BCC_A2	860	1		15	0.35	84.65			
BCC_A2	840	1		15	0.35	84.65			
BCC_A2	820	1		15	0.35	84.65			
BCC_A2+HCP_A3	809.318	1	0	15	0.35	84.65	0.0396777	1.94368	98.0166
BCC_A2+HCP_A3	800	0.974007	0.025993	15.3579	0.314395	84.3277	0.0451717	1.83789	98.1169
BCC_A2+HCP_A3	780	0.914386	0.085614	16.2518	0.243734	83.5045	0.0598198	1.6183	98.3219
BCC_A2+HCP_A3	760	0.850173	0.149827	17.3455	0.182526	82.472	0.078592	1.41544	98.506
BCC_A2+HCP_A3	740	0.783075	0.216925	18.6639	0.132022	81.2041	0.100956	1.23641	98.6626
BCC_A2+HCP_A3	720	0.715661	0.284339	20.2129	0.0923306	79.6948	0.125329	1.08525	98.7894
BCC_A2+HCP_A3	700	0.650613	0.349387	21.9783	0.0624722	77.9593	0.149513	0.961889	98.8886
BCC_A2+HCP_A3	680	0.589946	0.410054	23.9336	0.0408466	76.0256	0.171418	0.863154	98.9654
BCC_A2+HCP_A3	660	0.534712	0.465288	26.0501	0.0257241	73.9241	0.189527	0.784626	99.0258
BCC_A2+HCP_A3	640	0.485156	0.514844	28.3032	0.0155263	71.6813	0.202978	0.722033	99.075
BCC_A2+HCP_A3	620	0.441031	0.558969	30.6734	0.00892456	69.3177	0.211446	0.671821	99.1167
BCC_A2+HCP_A3	600	0.401853	0.598147	33.1464	0.00484901	66.8487	0.214991	0.631216	99.1538
BCC_A2+HCP_A3	580	0.367073	0.632927	35.7108	0.00246951	64.2867	0.213929	0.598113	99.188
BCC_A2+HCP_A3	560	0.336166	0.663834	38.3558	0.00116803	61.643	0.208746	0.570915	99.2203
BCC_A2+HCP_A3	540	0.308667	0.691333	41.0699	0.00050808	58.9296	0.200033	0.548408	99.2516
BCC_A2+HCP_A3	520	0.284178	0.715822	43.8388	0.000201224	56.161	0.188438	0.529656	99.2819
BCC_A2+HCP_A3	500	0.262365	0.737635	46.6456	7.18E-05	53.3544	0.174624	0.513935	99.3114

Table A3: Pandat calculations for Ti-15Mo-0.5O

Phase Name	T[°C]	Volume Fraction (BCC_A2)	Volume Fraction (HCP_A3)	w%(MO@BCC_A2)	w%(O@BCC_A2)	w%(TI@BCC_A2)	w%(MO@HCP_A3)	w%(O@HCP_A3)	w%(TI@HCP_A3)
BCC_A2	900	1		15	0.5	84.5			
BCC_A2	880	1		15	0.5	84.5			
BCC_A2	860	1		15	0.5	84.5			
BCC_A2+HCP_A3	842.934	1	0	15	0.5	84.5	0.0205527	2.50242	97.477
BCC_A2+HCP_A3	840	0.993011	0.00698859	15.0939	0.487646	84.4185	0.0212043	2.47165	97.5072
BCC_A2+HCP_A3	820	0.943229	0.0567715	15.8012	0.405696	83.7931	0.0264306	2.26251	97.7111
BCC_A2+HCP_A3	800	0.889822	0.110178	16.6437	0.328939	83.0274	0.0332415	2.0576	97.9092
BCC_A2+HCP_A3	780	0.833288	0.166712	17.6459	0.259131	82.0949	0.0418662	1.8617	98.0964
BCC_A2+HCP_A3	760	0.774638	0.225362	18.8285	0.197839	80.9737	0.052326	1.67973	98.2679
BCC_A2+HCP_A3	740	0.715352	0.284648	20.2034	0.14611	79.6505	0.0643098	1.51579	98.4199
BCC_A2+HCP_A3	720	0.657123	0.342877	21.771	0.104229	78.1248	0.0771461	1.37226	98.5506
BCC_A2+HCP_A3	700	0.601494	0.398506	23.5203	0.07171	76.408	0.0899189	1.24949	98.6606
BCC_A2+HCP_A3	680	0.549572	0.450428	25.4335	0.0474815	74.519	0.101668	1.14617	98.7522
BCC_A2+HCP_A3	660	0.501938	0.498062	27.491	0.0301635	72.4788	0.11157	1.06001	98.8284
BCC_A2+HCP_A3	640	0.458726	0.541274	29.6748	0.0183067	70.3069	0.11904	0.988462	98.8925
BCC_A2+HCP_A3	620	0.419774	0.580226	31.97	0.0105572	68.0194	0.123753	0.929055	98.9472
BCC_A2+HCP_A3	600	0.384762	0.615238	34.3653	0.00574646	65.629	0.125621	0.879634	98.9947
BCC_A2+HCP_A3	580	0.353314	0.646686	36.8509	0.00292945	63.1461	0.124744	0.838386	99.0369
BCC_A2+HCP_A3	560	0.325063	0.674937	39.4175	0.00138647	60.5811	0.121366	0.803827	99.0748
BCC_A2+HCP_A3	540	0.299676	0.700324	42.0542	0.000603508	57.9452	0.115829	0.774749	99.1094
BCC_A2+HCP_A3	520	0.276868	0.723132	44.7474	0.000239265	55.2524	0.10853	0.750179	99.1413
BCC_A2+HCP_A3	500	0.256391	0.743609	47.4804	8.56E-05	52.5195	0.0998985	0.729332	99.1708

Table A4: Pandat calculations for Ti-15Mo-1O

Phase Name	T[°C]	Volume Fraction (BCC_A2)	Volume Fraction (HCP_A3)	w%(MO@BCC_A2)	w%(O@BCC_A2)	w%(Ti@BCC_A2)	w%(MO@HCP_A3)	w%(O@HCP_A3)	w%(Ti@HCP_A3)
BCC_A2	1200	1		15	1	84			
BCC_A2	1176.67	1		15	1	84			
BCC_A2	1153.33	1		15	1	84			
BCC_A2	1130	1		15	1	84			
BCC_A2	1106.67	1		15	1	84			
BCC_A2	1083.33	1		15	1	84			
BCC_A2	1060	1		15	1	84			
BCC_A2	1036.67	1		15	1	84			
BCC_A2	1013.33	1		15	1	84			
BCC_A2	990	1		15	1	84			
BCC_A2	966.667	1		15	1	84			
BCC_A2+HCP_A3	953.91	1	0	15	1	84	0.0059547	3.94726	96.0468
BCC_A2+HCP_A3	943.333	0.981811	0.018189	15.2431	0.953557	83.8033	0.00618371	3.86413	96.1297
BCC_A2+HCP_A3	920	0.939864	0.0601359	15.8381	0.850371	83.3115	0.006798	3.67683	96.3164
BCC_A2+HCP_A3	896.667	0.895329	0.104671	16.5277	0.746778	82.7256	0.0075889	3.48512	96.5073
BCC_A2+HCP_A3	873.333	0.848218	0.151782	17.3313	0.643772	82.0249	0.00859197	3.29068	96.7007
BCC_A2+HCP_A3	850	0.798737	0.201263	18.2707	0.542731	81.1866	0.00984241	3.09574	96.8944
BCC_A2+HCP_A3	826.667	0.747366	0.252634	19.3676	0.445461	80.1869	0.0113669	2.90304	97.0856
BCC_A2+HCP_A3	803.333	0.694905	0.305095	20.6411	0.354188	79.0047	0.0131701	2.71575	97.2711
BCC_A2+HCP_A3	780	0.642449	0.357551	22.1028	0.271379	77.6258	0.0152187	2.53716	97.4476
BCC_A2+HCP_A3	756.667	0.591252	0.408748	23.7538	0.199368	76.0468	0.0174275	2.37032	97.6123
BCC_A2+HCP_A3	733.333	0.542491	0.457509	25.5832	0.139817	74.277	0.0196573	2.21758	97.7628
BCC_A2+HCP_A3	710	0.497037	0.502963	27.5718	0.0932586	72.3349	0.0217289	2.08031	97.898
BCC_A2+HCP_A3	686.667	0.455332	0.544668	29.6987	0.0589543	70.2423	0.0234538	1.95883	98.0177
BCC_A2+HCP_A3	663.333	0.417422	0.582578	31.9468	0.0351743	68.018	0.0246671	1.85258	98.1227
BCC_A2+HCP_A3	640	0.383088	0.616912	34.3054	0.0196944	65.6749	0.0252544	1.7604	98.2143
BCC_A2+HCP_A3	616.667	0.351993	0.648007	36.7696	0.0102683	63.2202	0.0251642	1.68082	98.294
BCC_A2+HCP_A3	593.333	0.323786	0.676214	39.3371	0.00493572	60.658	0.0244079	1.6123	98.3633
BCC_A2+HCP_A3	570	0.298159	0.701841	42.0049	0.0021612	57.9929	0.0230512	1.5534	98.4235
BCC_A2+HCP_A3	546.667	0.274874	0.725126	44.7659	0.00085052	55.2333	0.0212005	1.50279	98.476
BCC_A2+HCP_A3	523.333	0.25375	0.74625	47.606	0.00029658	52.3937	0.018988	1.45932	98.5217
BCC_A2+HCP_A3	500	0.234649	0.765351	50.5041	9.04E-05	49.4958	0.0165575	1.42198	98.5615

Table A5: Pandat calculations for Ti-15Mo-2O

Phase Name	T[°C]	Volum Fractio n (BCC_A 2)	Volum Fractio n (liquid)	Volume Fraction (HCP_A3)	w%(MO@BCC_A 2)	w%(O@BCC_A 2)	w%(Ti@BCC_A 2)	w%(MO@liquid)	w%(O@liquid)	w%(Ti@liquid)	w%(MO@HCP_A 3)		w%(Ti@HCP_A 3)
BCC_A2+liquid	1600	0.5399 58	0.4600 42		3.83905	0.63629 1	95.5267	27.3012	3.50327	69.3936			
BCC_A2+liquid	1563. 33	0.5844 21	0.4155 79		4.55335	0.76645 9	94.6782	28.7376	3.62264	67.64			
BCC_A2+liquid	1526. 67	0.6280 21	0.3719 79		5.44182	0.91256 3	93.6456	30.0389	3.71098	66.2502			
BCC_A2+liquid	1490	0.6742 6	0.3257 4		6.54379	1.07928	92.3881	31.2703	3.77807	64.9508			
BCC_A2+liquid	1453. 33	0.7262 89	0.2737 11		7.90304	1.2547	90.8463	32.6671	3.83382	63.4991			
BCC_A2+liquid	1416. 67	0.7877 9	0.2122 1		9.57689	1.45267	88.9704	33.6509	3.88235	62.4668			
BCC_A2+liquid	1380	0.8637 67	0.1362 33		11.6251	1.67126	86.7036	34.835	3.91008	61.2329			
BCC_A2+liquid	1343. 33	0.9616 86	0.0383 14		14.0985	1.91459	83.9869	36.0266	3.95026	59.9814			
BCC_A2+liquid	1331. 43	1	0		15	2	83	36.4153	4.0156	59.5691			
BCC_A2	1306. 67	1			15	2	83						
BCC_A2	1270	1			15	2	83						
BCC_A2	1233. 33	1			15	2	83						
BCC_A2+HCP_A3	1197. 26	1		0	15	2	83				0.00391265	5.95163	94.0465
BCC_A2+HCP_A3	1196. 67	0.9993 65		0.000635	15.0082	1.99783	82.9939				0.00399508	5.94957	94.0569
BCC_A2+HCP_A3	1160	0.9590 88		0.040912	15.5501	1.86092	82.588				0.00353906	5.79162	94.205
BCC_A2+HCP_A3	1123. 33	0.9167 64		0.083236	16.1672	1.71806	82.1167				0.00324585	5.62296	94.3743
BCC_A2+HCP_A3	1086. 67	0.8721 15		0.127885	16.8783	1.56859	81.5528				0.00301259	5.44259	94.5548
BCC_A2+HCP_A3	1050	0.8248 7		0.17513	17.708	1.41303	80.878				0.00283898	5.2507	94.7465
BCC_A2+HCP_A3	1013. 33	0.7747 97		0.225203	18.6886	1.25025	80.0612				0.00271794	5.04839	94.9489
BCC_A2+HCP_A3	976.6 67	0.7217 7		0.27823	19.842	1.0805 7	79.0574				0.0026 4524	4.83605	95.1613
BCC_A2+HCP_A3	940	0.6658 81		0.334119	21.2811	0.906777	77.8161				0.00261673	4.61506	95.3823
BCC_A2+HCP_A3	903.3 33	0.6076 61		0.392357	23.0077	0.725169	76.2672				0.00262675	4.38761	95.6098
BCC_A2+HCP_A3	866.6 67	0.5482 81		0.451717	25.1005	0.547123	74.3524				0.00264687	4.15726	95.8401
BCC_A2+HCP_A3	830	0.4900 27		0.509973	27.5842	0.380729	72.0351				0.00270993	3.92977	96.0675
BCC_A2+HCP_A3	793.3 33	0.4358 96		0.564104	30.4053	0.236921	69.3548				0.00273425	3.71347	96.2838
BCC_A2+HCP_A3	756.6 67	0.3886 32		0.611568	33.4307	0.135731	66.4336				0.00264136	3.51488	96.4804
BCC_A2+HCP_A3	720	0.3482 67		0.651733	36.538	0.0680632	63.3981				0.00245071	3.34302	96.6525
BCC_A2+HCP_A3	683.3 33	0.3143 07		0.685693	39.6668	0.031161	60.302				0.00223445	3.19708	96.8007
BCC_A2+HCP_A3	646.6 67	0.2849 61		0.715039	42.8392	0.0123537	57.1284				0.00168776	3.07006	96.9281
BCC_A2+HCP_A3	610	0.2589 68		0.741052	46.1622	0.00616173	53.8337				0.00152136	2.9406	97.0379
BCC_A2+HCP_A3	573.3 33	0.2356 95		0.764505	49.6145	0.00514436	50.3843				0.00114092	2.84613	97.1327
BCC_A2+HCP_A3	536.6 67	0.2142 6		0.78574	53.2203	0.00324565	46.7794				0.00083 4645	2.78478	97.2144
BCC_A2+HCP_A3	500	0.1951 6		0.80484	56.9435	3.91E-05	43.0564				0.00054 5586	2.71521	97.2842

Appendix B

Avramni Exponent and Volume plots

Experimental isothermal data were analyzed within the framework of the JMAK model [1, 2]. The JMAK model assumes that phase changes occur via nucleation and growth reactions and that nucleation sites are randomly distributed. According to the most generalized JMAK equation for the isothermal nucleation and growth process, the volume fraction *X(t)* transformed at time *t* is given by:

$$X(t)=1-\exp\{-[k(t-\tau)]^n\}, \qquad (1)$$

Where n is the "Avramni exponent", which depends on the mechanism of the transformation process, *k* a temperature-dependent reaction rate constant, and τ is the incubation time. In isothermal trials, the transformed fraction $X(t)$ is related to the integrated signal through

$$X(t)=\frac{\int_{\tau}^{t}\left(\frac{dQ}{dt}\right)dt}{\int_{\tau}^{t_f}\left(\frac{dQ}{dt}\right)dt}=\frac{\Delta H(t)}{\Delta H}=\frac{A(t)}{A_{tot}}, \qquad (2)$$

Where dQ/dt is the heat flow detected by DSC, $\Delta H(t)$ the amount of heat released up to any time *t*, and ΔH is the total heat released during the α-grain boundary precipitation process, given by integrating the peak between τ and t_f, the process end time. For clarification, during integration the equation can also be written where $A(t)$ is the partial area of exothermic peak. This is obtained by integrating the isothermal DSC curves from τ up to any time *t* and A_{tot} is the total area of the exothermic peak due to α-grain boundary precipitation. Substituting Eq. (1) into Eq. (2), we obtain the direct

relationship between the DSC signal dQ/dt, and the rate of the precipitation process, dX/dt:

$$\frac{dQ}{dt} = \Delta H \frac{dX}{dt} = \Delta H n k^n (t-\tau)^{n-1} \exp\{-[k(t-\tau)]^n\}, \quad (3)$$

Solving Eq. (3) for $X(t)$ produces the most generalized JMAK equation as shown by Eq. (1) Based on Eq. (1), we can obtain the following equation:

$$\ln[-\ln(1-x)] = \ln k + n\ln(t-\tau). \quad (4)$$

The local Avramni exponent $n(x)$ can be calculated by differentiating Eq. (4):

$$n(x) = \frac{\partial \ln[-\ln(1-x)]}{\partial \ln(t-\tau)} \quad (5)$$

The experimental data were fitted using equation (4) and (5), respectively, in order to obtain the kinetic parameters k and n. The data fitting was performed using a commercial software program, OriginPro 8.5 (OriginLab Corporation, USA). The Avramni exponents found were associated with microstructural evolution based on a summary published by Christian, Table B4 [3].

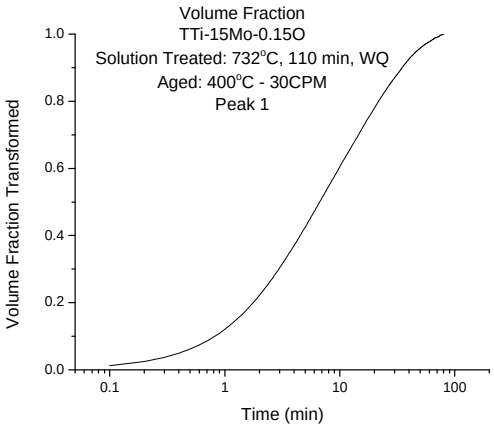

(a)

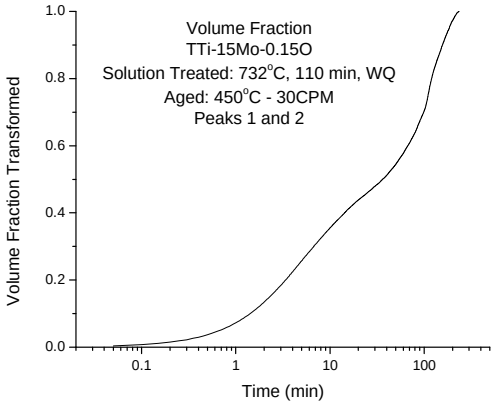

(b)

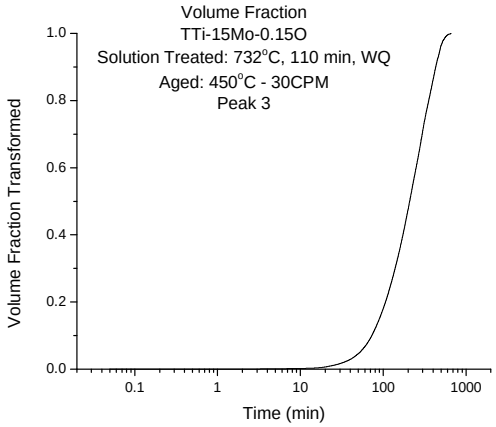

(c)

Figure B1: Sigmoidal plots for each individual peak occurring during isothermal aging of Ti-15Mo-0.15O

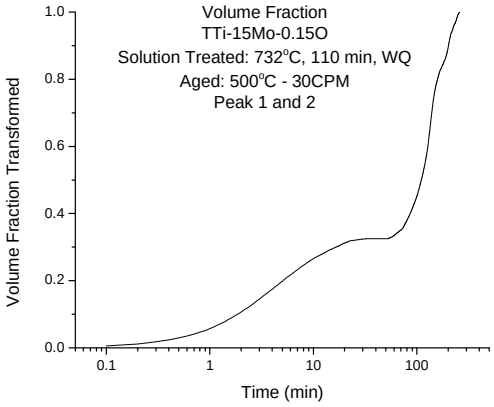

(d)

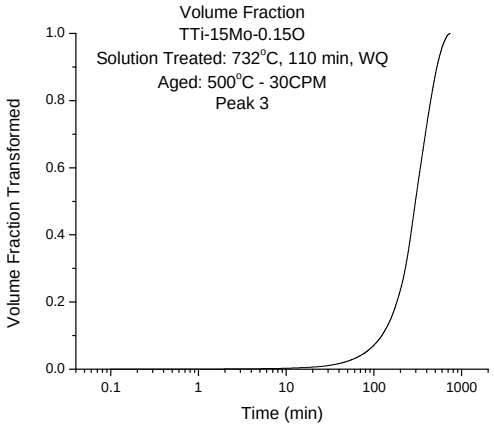

(e)

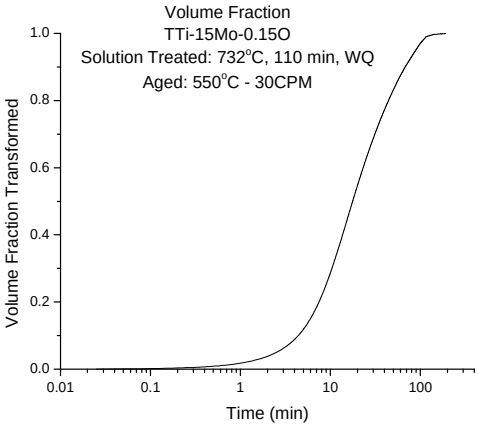

(f)

Figure B1: continued

Table B1: Avramni coefficients of Ti-15Mo-0.15O aged between 400 and 550°C.

Temperature	Avramni Coefficients	
400°C		
P1	0.977	0.76
450°C		
P1 + P2	0.978	0.37
P3	1.11	
500°C		
P1 + P2	0.91	1.857
P 3	1.09	1.98
550°C		
P1	1.1	

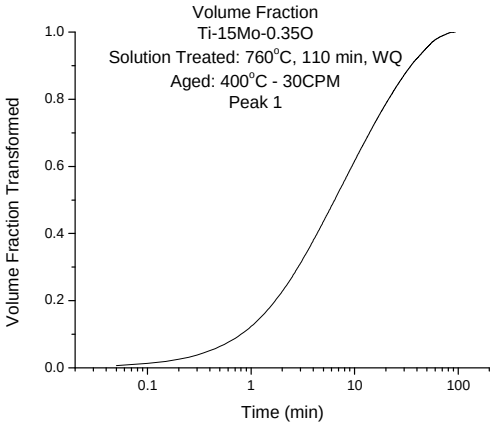

(a)

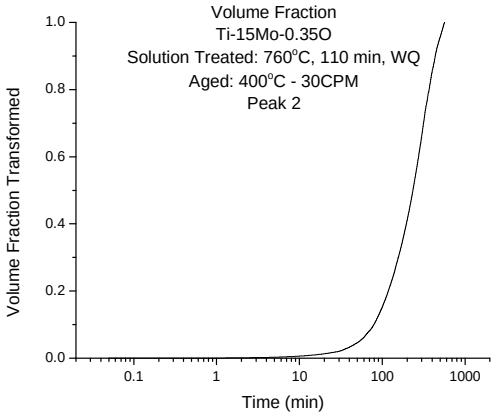

(b)

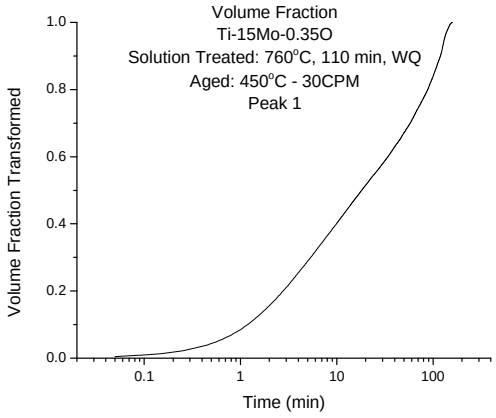

(c)

Figure B2: Sigmoidal plots for each individual peak occurring during isothermal aging of Ti-15Mo-0.35O

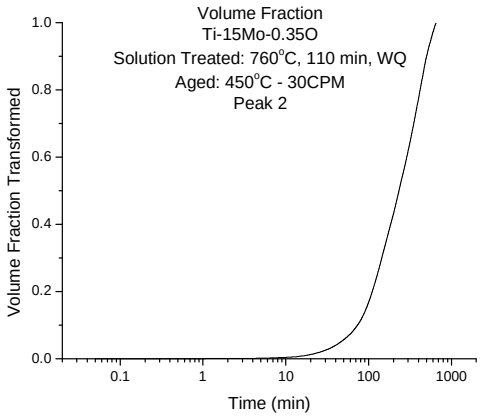

(d)

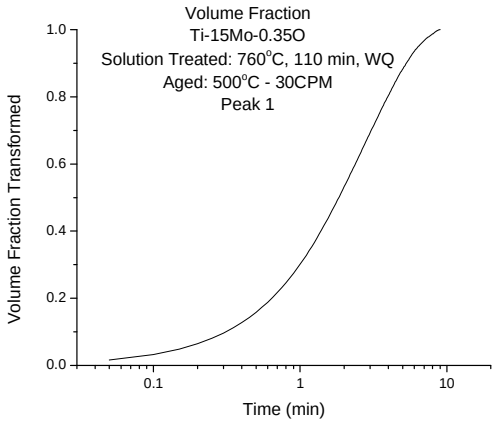

(e)

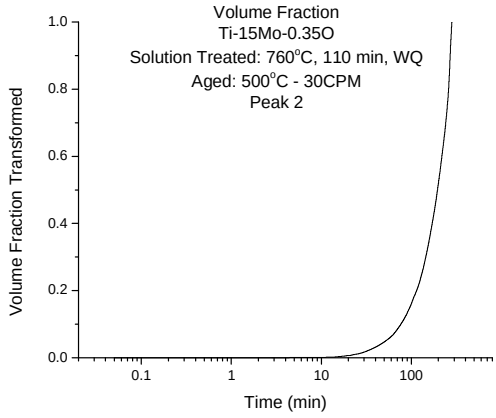

(f)

Figure B2: continued

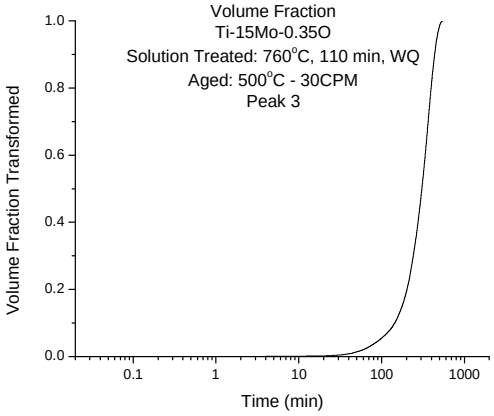

(g)

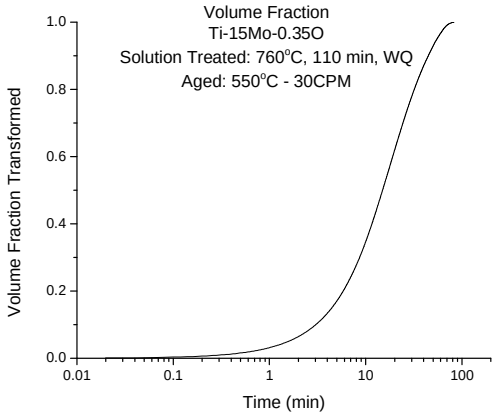

(h)

Figure B2: continued

Table B2: Avramni coefficients of Ti-15Mo-0.35O aged between 400 and 550°C.

Temperature	Avramni Coefficients		
400°C			
P1	0.96	0.71	
P2	1.19	1.79	
450°C			
P1	0.97	0.48	
P2	0.67	2.78	1.64
500°C			
P1	1.07		
P2	1.36	2.07	
P3	0.99	2.44	
550°C			
P1	1.1		

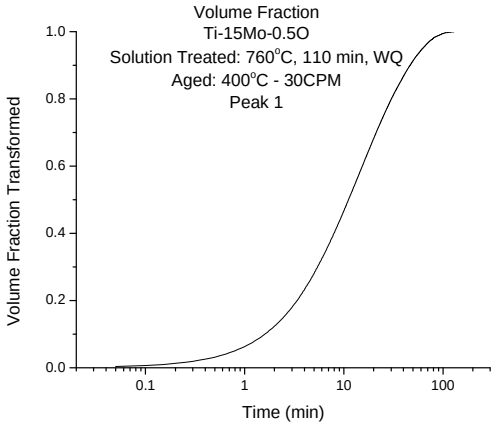

(a)

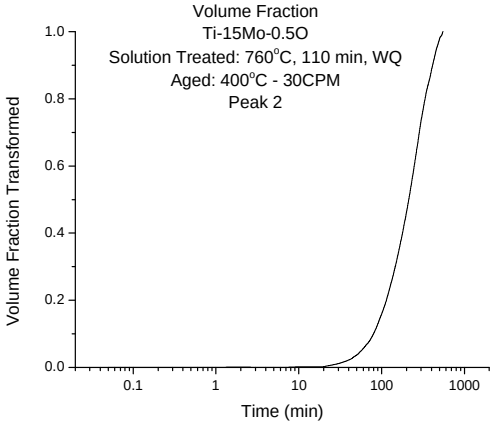

(b)

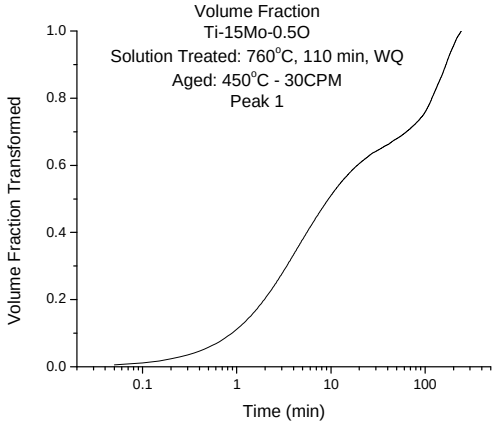

(c)

Figure B3: Sigmoidal plots of the isothermally observed DIC peaks for Ti-15Mo-0.5O

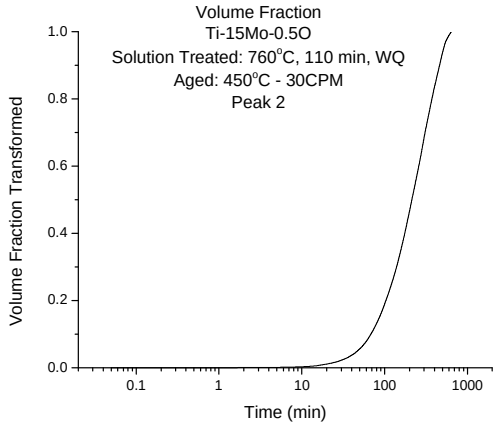

(d)

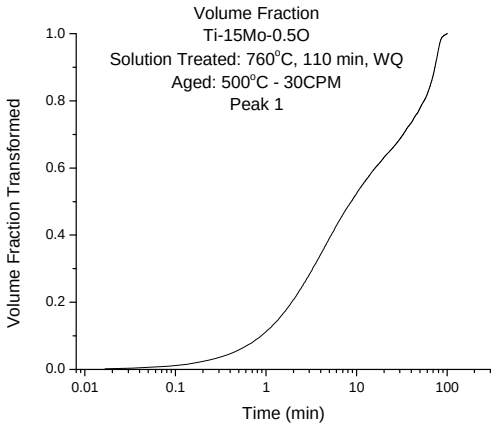

€

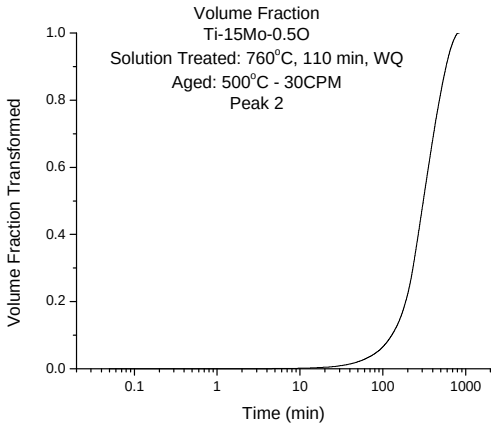

(f)

Figure B3: continued

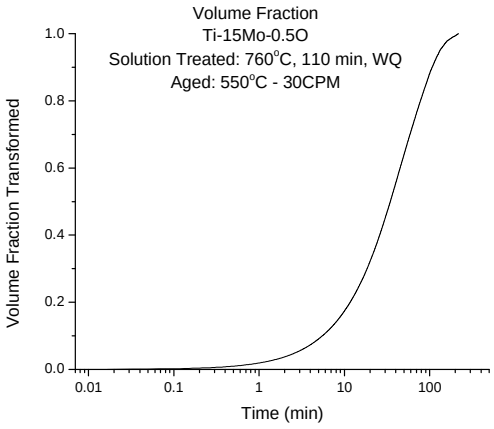

(g)

Figure B3: continued

Table B3: Avramni coefficients of Ti-15Mo-0.5O aged between 400 and 550°C.

Temperature	Avramni Coefficients	
400°C		
P1	0.92	
P2	1.1	1.96
450°C		
P1	0.96	0.24
P2	0.71	1.71
500°C		
P1	0.99	0.45
P2	1.89	
550°C		
P1	1.0	

Table B4: Values of n in the Kinetic Law: $X(t)=1-\exp\{-[k(t-\tau)]^n\}$ [3]

Conditions	n
Increasing nucleation rate	>4
Constant nucleation rate	4
Decreasing nucleation rate	3–4
Zero nucleation rate (saturation of point sites)	3
Grain edge nucleation after saturation	2
Grain boundary nucleation after saturation	1

(b) Diffusion controlled growth

Conditions	n
All shapes growing from small dimensions, increasing nucleation rate	$>2\frac{1}{2}$
All shapes growing from small dimensions, constant nucleation rate	$2\frac{1}{2}$
All shapes growing from small dimensions, decreasing nucleation rate	$1\frac{1}{2}$–$2\frac{1}{2}$
All shapes growing from small dimensions, zero nucleation rate	$1\frac{1}{2}$
Growth of particles of appreciable initial volume	1–$1\frac{1}{2}$
Needles and plates of finite long dimensions, small in comparison with their separation	1
Thickening of long cylinders (needles) (e.g. after complete end impingement)	1
Thickening of very large plates (e.g. after complete edge impingement)	$\frac{1}{2}$
Precipitation on dislocations (very early stages)	$\sim\frac{2}{3}$

References

[1] M. Avramni, J. Chem. Phys. 7 (1939) 1103

[2] M. Avramni, J. Chem. Phys. 8 (1940) 212

[3] J. W. Christian, The Theory of Transformation in Metals and Alloys (2nd ed.), Elsevier, Oxford (2002) 529